January 2013

Determining Best Method For Estimating Observed Level Of Maximum Convective Detrainment Based On Radar Reflectivity

Nicholas Daniel Carletta

DETERMINING BEST METHOD FOR ESTIMATING OBSERVED LEVEL OF MAXIMUM CONVECTIVE DETRAINMENT BASED ON RADAR REFLECTIVITY

by

Nicholas Daniel Carletta
Bachelor of Science, Iowa State University, 2011

A Thesis
Submitted to the Graduate Faculty

of the

University of North Dakota

in partial fulfillment of the requirements

for the degree of

Master of Science

Grand Forks, North Dakota
December
2013

This thesis, submitted by Nicholas Carletta in partial fulfillment of the requirements for the Degree of Master of Science from the University of North Dakota, has been read by the Faculty Advisory Committee under whom the work has been done and is hereby approved.

Gretchen Mullendore, Chairperson

Mark Askelson

Baike Xi

This thesis is being submitted by the appointed advisory committee as having met all of the requirements of the School of Graduate Studies at the University of North Dakota and is hereby approved.

Wayne Swisher
Dean of the School of Graduate Studies

December 5, 2013
Date

PERMISSION

Title Determining Best Method for Estimating Observed Level of Maximum Convective Detrainment based on Radar Reflectivity

Department Atmospheric Sciences

Degree Master of Science

In presenting this thesis in partial fulfillment of the requirements for a graduate degree from the University of North Dakota, I agree that the library of this University shall make it freely available for inspection. I further agree that permission for extensive copying for scholarly purposes may be granted by the professor who supervised my thesis work or, in her absence, by the Chairperson of the department or the dean of the School of Graduate Studies. It is understood that any copying or publication or other use of this thesis or part thereof for financial gain shall not be allowed without my written permission. It is also understood that due recognition shall be given to me and to the University of North Dakota in any scholarly use which may be made of any material in my thesis.

Nicholas Carletta
November 19, 2013

TABLE OF CONTENTS

LIST OF FIGURES

Figure Page

LIST OF TABLES

Table Page

ACKNOWLEDGEMENTS

I would like to thank my committee for their advice and support throughout this project. I would also like to acknowledge the support of NSF Grant ATM-0918010, as it supported my research work. I would like to acknowledge Dr. Timothy Lang for providing the dual-Doppler data for the nine test cases. Finally, I would like to thank Zhe Feng, Xiquan Dong, and Baike Xi for supplying the code for the CSA algorithm and providing support in using it.

ABSTRACT

Convective mass transport is the transport of mass from near the surface up to the upper troposphere and lower stratosphere (UTLS) by a deep convective updraft. This transport can alter the chemical makeup and water vapor balance of the UTLS, which can affect cloud formation and the radiative properties of the atmosphere. It is therefore important to understand the exact altitudes at which mass is detrained from convection. The purpose of this study is to improve upon previously published methodologies for estimating the level of maximum detrainment (LMD) within convection using data from individual radars. Three methods were used to identify the LMD and validated against dual-Doppler derived vertical mass divergence fields. The best method for locating the LMD was determined to be the method that uses a horizontal reflectivity texture-based technique to determine convective cores and a multi-layer echo identification to determine anvil locations.

The methodology was found to work in many but not all cases. The methodology works best when applied to convective systems with mature updrafts, and is most accurate with convective lines and isolated cells. A time lag is present in the reflectivity based LMD compared to the vertical mass divergence based LMD because the reflectivity method is dependent on anvil growth.

This methodology was then applied to archived NEXRAD 3D mosaic radar data. The regions of analysis were chosen to coincide with the observation regions for the Deep

Convective Clouds and Chemistry Experiment (DC3): the Colorado Foothills, Southern Plains (OK/TX), and Southeast US (AL). These three regions provide a wide variety of convection. The dates analyzed were from May and June of 2012 so the results can be compared to future DC3 studies

CHAPTER 1

INTRODUCTION

Convective mass transport is the transport of mass from near the surface up to the upper troposphere and lower stratosphere (UTLS) due to a deep convective updraft. This transport can affect cloud formation and can change the radiative properties of the atmosphere by altering the composition of the UTLS (Lopez et al. 2006). This change in radiative properties can occur because some chemicals, such as ozone, have slower chemical destruction and higher production efficiency in the UTLS than at or near the surface (Leliveld and Crutzen 1994). It is therefore important to understand the exact altitudes at which mass is detrained from convection. Determining the levels of detrainment and measuring convective mass transport has been done in previous studies based on satellite based measurements (e.g., Fishman et al. 1990), aircraft measurements (e.g., Pickering et al. 1996), and numerical modeling (e.g., Mullendore et al. 2005). Due to the low spatial or temporal resolution (varies based on satellite) of satellite based measurements and infrequency of aircraft measurements modeling has been the focus of study. Modeling studies have been a major component of convective mass transport studies but more observations are needed to constrain these models. A relatively recent method employed to obtain more observations is using proxies to represent the area of detrainment from deep convective updrafts.

One study that determines detrainment with a proxy is Mullendore et al. (2009), which used the reflectivity of anvils as a proxy. In Mullendore et al. (2009) comparisons were made between the radar as a proxy method and dual-Doppler derived vertical mass divergence. In this comparison, a level of maximum detrainment (LMD) was determined for both methods and compared. While the method used in Mullendore et al. (2009) to estimate where detrainment occurred work well, it was applied to a very "clean" or well-organized convective line in the tropics, i.e. a convective line in which both the deep updraft cores and forward anvil were easy to identify. Will similar methodology perform well for other storm types and more complex morphologies in different parts of the world? This is the main question that this study will answer. This work builds upon the use of radar reflectivity in Mullendore et al. (2009) and expands it into a methodology that can be applied in the midlatitudes for a variety of storm types. Suggestions for application were developed for the method so that it can be applied to datasets beyond the test cases used for development of the method. Cases considered here are from the Deep Convective Clouds and Chemistry Experiment's (DC3) three analysis regions during May and June of 2012.

CHAPTER 2

BACKGROUND

Convective mass transport involves rapid vertical transport in the troposphere due to deep convective updrafts. Convective mass transport is an important atmospheric process to understand since it can have a significant impact on various gases in the atmosphere such as ozone, carbon monoxide, methane, and nitrogen oxides (Lelieveld and Crutzen 1994). While vertical transport of these gases occurs in the absence of any form of deep convection, the vertical transport is much more rapid in deep convection. Transport through cumulonimbus clouds takes between 0.5-1.0 hr while mesoscale subsidence over a larger area can take between 10-50 hr (Lelieveld and Crutzen 1994). Due to these impacts, convective mass transport has been studied by many researchers, but many questions regarding convective mass transport remain. One question that will be addressed in this study is how can simulated convective mass transport be the best constrained at cloud-scales with observations?

To provide context for this research project, an overview of some important and recent research in the area of convective mass transport will be presented. Second, an overview of radar reflectivity and velocity that has been used in convective mass transport validation will be discussed. Velocity based observations are useful when a Dual-Doppler analysis has been performed because it provides vertical motion, which is needed to identify deep convective updrafts. Lastly, convective and anvil classification schemes will be

discussed, as these schemes are needed to identify different parts of convective storms, particularly since dual-Doppler networks are rare outside of research projects.

2.1 Previous Studies of Convective Mass Transport

Multiple observational studies, such as the Deep Convective Clouds and Chemistry (DC3) Experiment (Barth et al. 2012), North Dakota Thunderstorm Project (Boe et al. 1992), Cloud Dynamics and Chemistry Field Experiment (CLEOPATRA; Hauf et al. 1995), Transport and Atmospheric Chemistry near the Equator – Atlantic (TRACE-A; Andreae et al. 1996), and the Mediterranean Oxidant Study (MINOS; Fischer et al. 2003), have examined the transport of trace gases in deep convection. These studies have taken place in a variety of locations around the world and have used a variety of observation methods to collect measurements. One of the most useful measurements in field campaigns is gained from aircraft in-situ measurement. The instruments carried by Aircraft can collect gas phase samples and determine the composition of the atmosphere in both a pre-storm and post-storm environment. Any differences of atmospheric composition between pre-storm and post-storm can be obtained by these measurements and will represent the mass transported by convection. Studies in the tropics have often focused on the impact on the general circulation because of the large areal coverage and frequency of convection in the Intertropical Convergence Zone (ITCZ). Studies in the mid-latitudes also have looked at global transport, but since convection is not as widespread as in the ITCZ, the focus often has been on more localized effects.

In addition, net vertical transport from the troposphere to the stratosphere is positive (i.e. upward) at low latitudes, and negative at high latitudes (e.g. Holton et al. 1995). However, even in regions of net negative vertical transport, the rapid vertical transport of

boundary layer air to the upper troposphere and lower stratosphere (UTLS) in convection has potentially significant impacts on the water vapor and chemical mixing ratios in the UTLS, and, therefore on the radiative balance. One of the earlier experiments in which transport in the mid-latitudes was observed is the Preliminary Regional Experiment for Stormscale Operational and Meteorology Program-Central Phase (PRESTORM; Dickerson et al., 1987) project. From observations taken during PRESTORM, Dickerson et al. (1987) were able to conclude that rapid vertical transport of trace gases from the boundary layer to the UTLS via convective transport played an important role in the budgets of trace gases in the UTLS.

The various gases that are transported via convection can also be observed by satellite. A common example is the measurement of ozone. Fishman et al. (1990) found tropospheric ozone maximums in the South Atlantic via the Stratospheric Aerosol and Gas Experiment I (SAGE I) and SAGE II satellites. Chatfield and Delany (1990) and Pickering et al. (1992) hypothesized that ozone that was convectively lofted in Brazil could be responsible for this maximum. Unlike aircraft data, which are usually recorded as part of a field campaign wherein the measurements can be collected near a storm, the information provided by satellite cannot be directly related to the convective transport. As other components of the general circulation may be responsible for vertical transport, determining the sources of satellite-observed transport can be challenging. Additionally, the coarse temporal and spatial resolution of satellites often obscures out the signal of individual convective cores. Since all observation platforms have their disadvantages modeling is frequently used since the temporal and spatial resolutions can be set.

A major motivator for convective mass transport research has been to improve chemical and climate models. Climate models must correctly simulate convective mass

transport, as transport across the equator is primarily accomplished through deep tropical convection (Rind and Lerner 1996). For atmospheric chemistry models to correctly simulate the UTLS and their interactions, the level of maximum detrainment (LMD) must be correctly identified, because transport of gases from near the surface to the UTLS can change the radiative properties of the UTLS (Lopez et al. 2006). In the upper troposphere, the trace gases that are transported from the surface can have longer chemical residence times than they would have had near the surface (Dickerson et al. 1987; Erukhimova and Bowman 2006). Cotton et al. (1995) used observational and cloud resolving models to obtain an estimate of how much mass transported from the boundary layer from different types of storms. Cotton et al. (1995) also found that extratropical cyclones transported the most mass followed by mesoscale convective systems (excluding mesoscale convective complexes (MCC)), ordinary thunderstorms, tropical cyclones, and MCCs. Cotton et al. (1995) estimated an annual flux of 4.95 X 1019 kg of boundary layer air, which is equivalent to a transport of the entire boundary layer 90 times in a year. Another modeling study that demonstrates the differences in mass transport of different storm types is done by Mullendore et al. (2005). In Mullendore et al. (2005), both supercell and multicell were simulated in a three-dimensional cloud-resolving model. The amount of boundary layer tracer transported by the supercell was almost double the amount of tracer transported by the multicell. Significant convective transport and differences owing to storm type need to be included in climate models to accurately simulate the atmosphere's chemical composition.

Global transport models currently do not explicitly resolve updrafts, so differences in vertical transport due to storm morphology and/or storm evolution are not included. Most mass-flux transport parameterizations use the thermodynamic profile and estimates of

entrainment to determine the depth of transport. The level of neutral buoyancy (LNB) has been used to approximate the upper bound of detrainment altitude, but the exact distance between the LNB and the LMD is not known. Mullendore et al. (2009; hereafter M09), Takahashi and Luo (2012), and Mullendore et al. (2013) all show that the LMD is much lower than the LNB for most cases. Takahashi and Luo (2012) demonstrated this with a near-global survey of storms based on CloudSat, a satellite-based radar, data and found that the LNB derived using a sounding was an upper bound for convection, but was not where the maximum mass detrainment occurred. They found that on average the LMD was 3 km lower than the LNB based on parcel theory. Mullendore et al. (2013) used data from cases from the Severe Thunderstorm Electrification and Precipitation Study (STEPS), which enabled analysis of a variety of storm types and of characteristics at different evolutionary stages. They used the same method as M09 to develop vertical velocity divergence profiles, which provides divergence-based LMD estimates for comparison to the LNB. It was found that the LMD was generally below the LNB by an average of 2.2 km. The difference between LMD and LNB altitudes did vary significantly based on storm type, with LMD altitudes being just below or equal to LNB altitudes for the supercell cases. Mullendore et al. (2013) also demonstrated that the LMD varied, sometimes significantly, over the life of a storm, with convective lines having the greatest variability with respect to time.

2.2 Radar Reflectivity as a Proxy for Convective Transport

The different methods of studying convective mass transport and its associated detrainment have advantages and disadvantages. Temporal, spatial, and spectral resolution can vary significantly depending on the satellite platform. Some satellites only measure the total chemical mass in a column while others can detect values at different vertical levels.

No one satellite has great temporal, spatial, and spectral resolution. Therefore, satellites cannot retrieve storm scale transport. Aircraft measurements have excellent spatial and temporal resolution, but represent only the regions sampled, and not a view of the entire storm structure. Additionally, aircraft measurements are often not available because of the high costs of operation. With models, temporal and spatial resolutions can be decided by the modeler, but observations are needed to constrain these models. A method of observation is needed that can cover a large area and provide detrainment values at higher spatial resolution than possible with satellite data. One way this can be done is by using anvil reflectivity as a proxy for the area of maximum detrainment (Mullendore et al. 2009). This method was also used with satellite-based radar data (CloudSat) by Takahashi and Luo (2012). Expanding upon this prior work so that it can be applied to a variety of storm types around the world would help to constrain the chemical and climate models.

2.2.1 Recent Studies

In a recent study, M09 demonstrated a strong correlation between the radar reflectivity in the anvil near convection and the LMD. M09 did a case study of the 26 January 1999 squall line during the Tropical Rainfall Measuring Mission Large Scale Biosphere Atmosphere field campaign (TRMM-LBA). In their study, the assumption was that the majority of hydrometeors in the anvil near the updraft were due to detrainment from vertical mass convergence. The extent and magnitude of the convergence was compared to the extent and magnitude of the concentration of the hydrometeors in the anvil. TRMM-LBA provided dual-Doppler data from which vertical velocity divergence profiles could be produced. M09 used dual-Doppler vertical velocities to calculate vertical mass divergence [$d(\rho w)/dz$] at each grid point and then integrated over each vertical level to produce vertical

mass divergence plots. From these, the largest negative vertical mass divergence was used to identify the location of the LMD since vertical mass convergence implies horizontal mass detrainment. It should be noted that while this methodology gives a good estimate of the detrainment heights, the percentage of boundary layer air in the detrained air mass reminds undetermined, which is simply because initial parcel conditions and the entrainment of free tropospheric environmental air is not quantified. This LMD derived from dual-Doppler velocities was assumed to be the "true" detrainment level for use in testing the methodology that uses radar reflectivity alone. The M09 method used an approximation of the Steiner et al. (1995) method to identify convective regions (see section 2.3, below, for a more in depth explanation of the Steiner et al. (1995) method). Anvils were defined as regions where reflectivity echo tops were above 6 km and no echo was present below 2.5 km. The anvil regions that were used were within 20 km of the convective regions, as shown by the black box in Fig. 1.

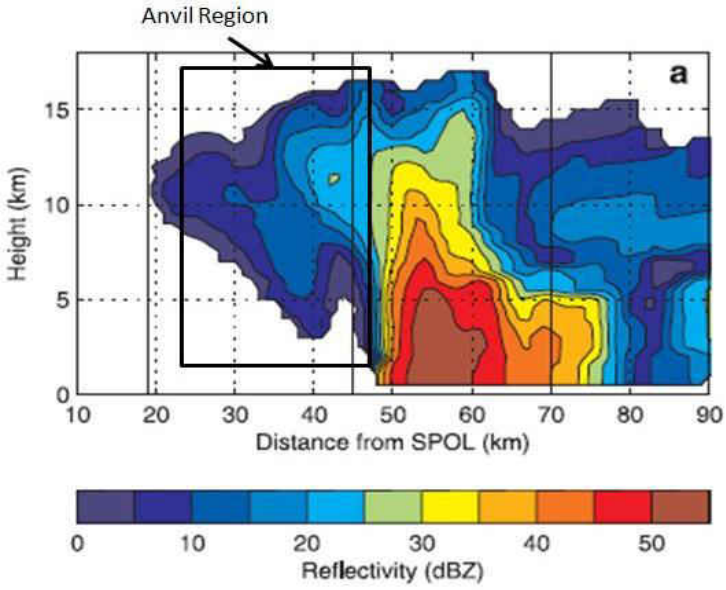

Figure 1: Taken from Mullendore et al. (2009) Figure 4a. A vertical cross section of reflectivity taken perpendicular to the line from 1950 UTC for the 26 January 1999 convective line. A box has been added to the original figure to illustrate the anvil region thus the reflectivity values that were used to calculate the ice mass.

The anvil regions were assumed to be primarily ice, so hydrometeor mass was estimated using

$$I = 0.008 * Z_I^{0.61} \quad (1)$$

where I is the ice water content and Z_I is the radar reflectivity (mm^{-6} m^3) from ice precipitation (Leary and Houze 1979). The resulting ice mass profile (Fig. 2, red line) was found to correlate well with the detrainment profile determined from the vertical velocity field (figure 2, blue line). The radar-estimated LMD (maximum value, red line) lines up well with the divergence-estimated LMD (minimum value, blue line).

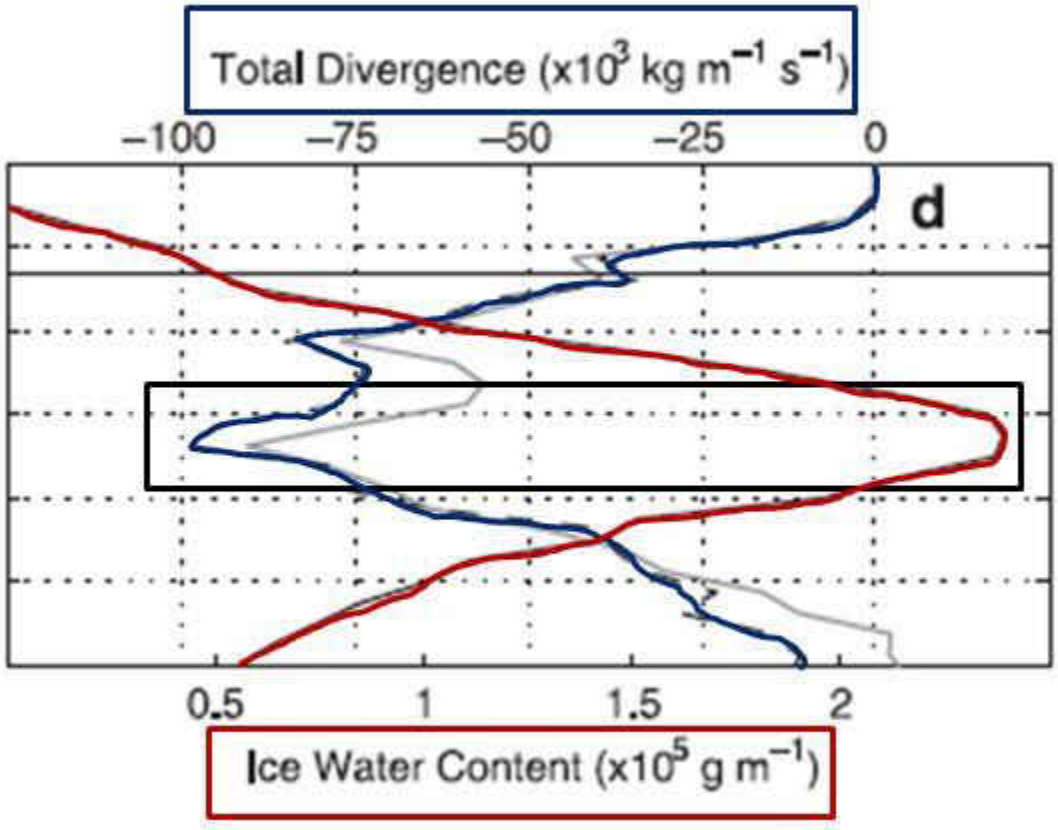

Figure 2: Taken from Mullendore et al. (2009) Figure 4d. The total vertical mass divergence of positive velocities (blue line), total vertical mass divergence of all velocities (grey line) and total ice water mass (red line) from 1950 UTC for the 26 January 1999 convective line. The box emphasizes that the minimum of total vertical mass divergence is at the same level as the maximum of total ice water mass.

2.2.2 Radar Retrievals

Although radar cannot directly measure hydrometeor mass, reflectivity can be used to approximate hydrometeor mass and convective mass transport. In order to understand the challenges associated with using radar observations to study vertical mass transport, an overview of radar observational techniques is presented here. Weather radars operate by transmitting microwaves into the atmosphere, which interact with hydrometeors that scatter the microwave energy. Not all the energy that hits the particle is scattered, as some is absorbed by the particle. The amount scattered and absorbed depends upon the size, shape, composition, orientation, and refractive index of the particle. Some of the energy will be backscattered to the radar's receiver, which will be amplified and converted into signals to be analyzed.

One of the primary challenges of determining hydrometeor mass from reflectivity is that there is no way to definitely know if the return signal was from a liquid hydrometeor, an ice hydrometeor, or some combination of the two. In some studies, such as M09, assumptions regarding the type of hydrometeors present in the area of study can be used to minimize this problem. For M09, the focus was on the convective anvil, which is predominantly ice, so an assumption can be made that all of the hydrometeors were ice. If an assumption like this can be made, then relationships do exist to convert reflectivity into ice or liquid water mass. For example, Leary and Houze (1979) did a comparative case study through which they were able to derive equations for estimating the ice water and liquid water content based on the reflectivity of the ice and liquid water in a storm. A source of uncertainty when using the Leary and Houze (1979) equation is that it is taking a 6th moment input ($mm^6\ m^{-3}$) and outputting a 3rd moment result (g m-3).

Radar retrievals are also used to analyze storm-scale wind fields. Dual-Doppler analysis provides three-dimensional wind fields that can be used to understand the detailed structure of convective cores. Doppler radars are used to measure hydrometeor motion and, by assuming that wind is the reason that the hydrometeors are moving, wind fields. A single Doppler radar can be used to detect if a hydrometeor is either moving towards the radar or away from the radar. Through the use of two Doppler radars and some trigonometry, two-dimensional wind fields can be estimated. Additionally, through the use of the continuity equation, vertical motion can also be calculated to give a full three dimensional wind field. This can be accomplished using the method outlined in Ray et al. (1980). The method used to integrate the continuity equation can greatly change the result, as errors change based upon the order of integration. A downward integration will reduce error near the top of a storm but will produce larger errors near the surface. An upward integration will have less error near the surface but much more error at higher altitudes. Finally, a blend of the two methods can be used to reduce error over the depth of the storm, but will produce more error near the surface than an upward integration scheme and more error at higher altitudes than a downward integration scheme.

2.3 Classification Schemes

Knowing the location of deep convective updrafts is vital when finding convectively generated anvil, such as in M09. When vertical motion cannot be obtained, other methods of identifying convective cores must be used. One way convective cores can be identified is based on radar reflectivity, e.g. the method demonstrated in Steiner et al. (1995). For the Steiner et al. (1995) methodology, before anything else is done any grid point in the field with radar reflectivity over the threshold value of 40 dBZ is classified convective since

reflectivity of this intensity is rarely stratiform. In the next step, Steiner et al. (1995) used a background exceeding technique on a low-level two dimensional horizontal reflectivity field to determine convective locations. Figure 3 is a plot of the function that determines the threshold value of reflectivity difference for each mean background reflectivity. Reflectivity at each radar grid point is compared to its background intensity, and if it exceeds the background intensity threshold value (Fig. 3, thick black line), it is assigned as convective.

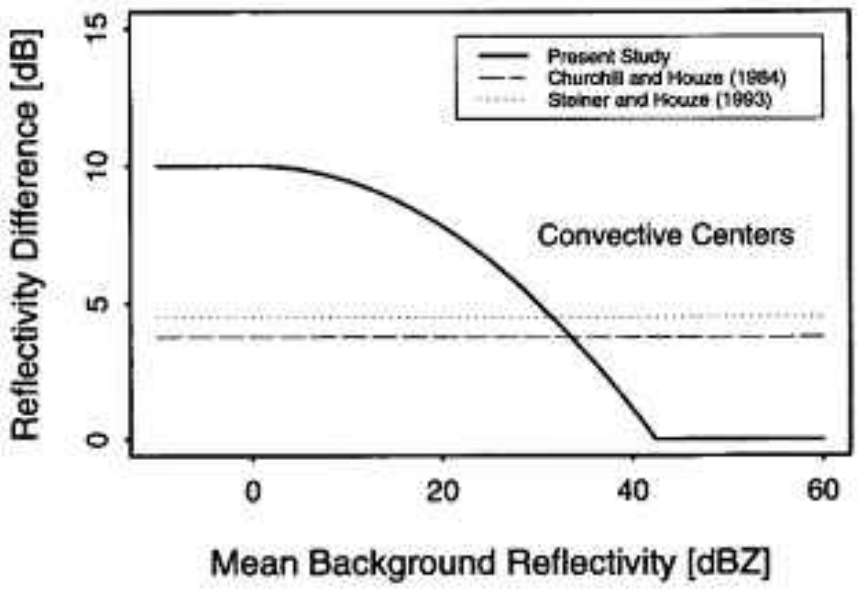

Figure 3: Taken from Steiner et al. (1995) figure 7. This figure compared the convective threshold function for three different studies. The thick black line is Steiner et al. (1995) while the dashed and dotted lines are previous studies with constant thresholds.

The background intensity is determined "as the linear average of the nonzero radar echoes ($mm^6\ m^{-3}$) within a radius of 11 km around the grid point" (Steiner et al. 1995), i.e. the threshold is a function of the background reflectivity value determined by the average intensity of the background. Once the convective center is assigned, surrounding grid points are also assigned as convective if within a defined "convective radius"; this convective radius depends on the mean background reflectivity and determination of convective area size

(small, medium, or large; Figure 4). The remaining area with reflectivity is simply assigned as stratiform rain.

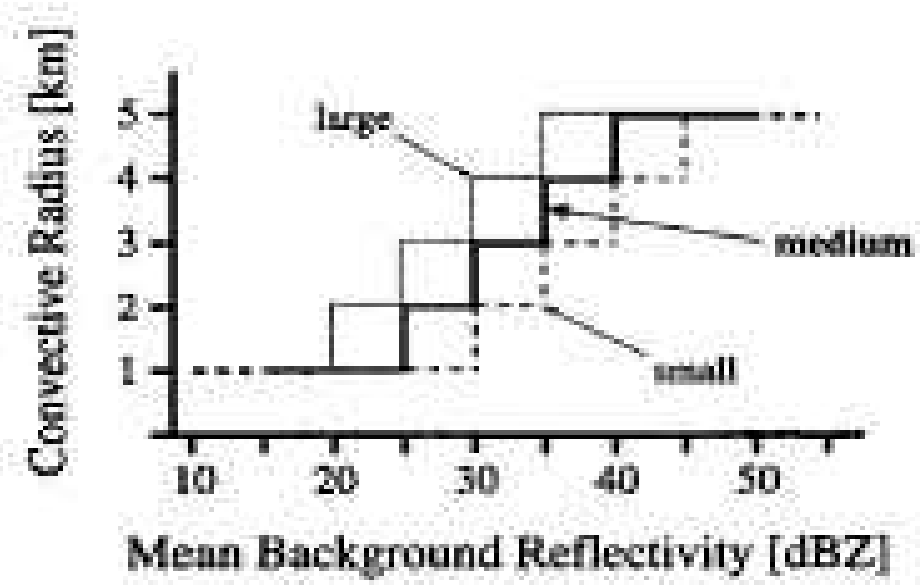

Figure 4: Taken from Steiner et al. (1995) figure 6b. A step function that determines the convective radius around convective points based on the size of the convective area (small, medium, or large) and the mean background reflectivity.

In Feng et al. (2011), a convective stratiform anvil (CSA) scheme was developed which builds upon the Steiner et al. (1995) scheme by breaking storms down into four parts: convective core, stratiform region, transitional anvil, and thick anvil. Thin anvil is also classified but that classification is dependent on GOES satellite data and therefore will not be used in this study. The first step in the CSA radar scheme is to separate low, middle, and high layer clouds to help in identifying low-level stratus and cirrus clouds. Then, up to five echo layers are determined for each vertical column. An echo layer is defined as "having contiguous reflectivity value above -10 dBZ with no more than one gap (0.5 km vertically)." The classification levels used in Feng et al. (2011), as well as the study presented herein, were surface to 3 km, 3 km to 6 km, and 6 km to the top value of the dataset. The levels were

selected based on upon the height used for stratus and cirrus clouds in Dong et al. (2006). Due to ground clutter, all anvil classifications can have echoes in the low level (Feng et al. 2011). If the base of a single echo layer is in the lowest classification level, and in the same vertical column, the top of an echo layer is in the highest classification level then it is defined as a transitional anvil (Feng et al. 2011). All transitional anvil classifications must have not continuous anvil unless there the echo base is above the low level (Feng et al. 2011). If the base of every echo layer is above the lowest classification level and, in the same vertical column, the top of an echo layer is in the highest classification level, and then it is defined as a thick anvil (Feng et al. 2011). Lastly, the convective cores and stratiform regions from the Steiner et al (1995) scheme must have contiguous echo up from below the low level to above the middle level to maintain their classifications (Feng et al. 2011).

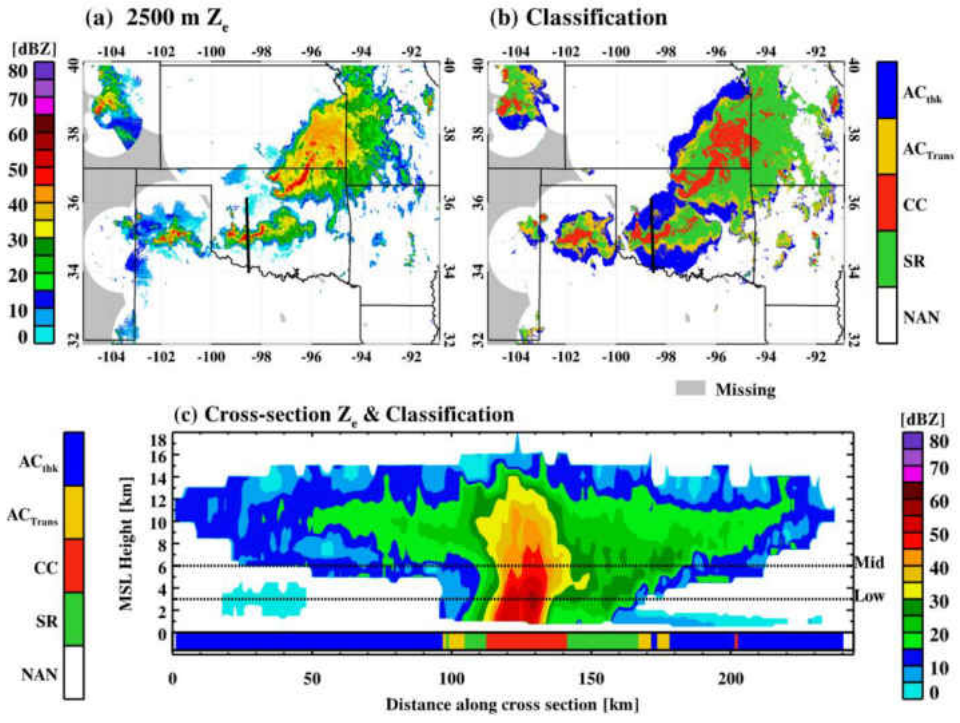

Figure 5: Taken from figure 3 of Feng et al. (2011). This is an example of the CSA radar classification method for a convective system. (a) NEXRAD horizontal reflectivity at 2500 MSL with the gray areas representing the boundaries of the radars used in the mosaic. (b) The classifications based on reflectivity data from all levels. (c) Vertical reflectivity cross section at the black line in a and b with the classification categories color coded below the cross section. The two dashed lines in c are the low and mid level heights.

Figure 5 shows an example of the classification scheme compared to both horizontal and vertical reflectivity cross sections. For this study the important classifications will be the convective cores (red), thick anvil (blue), and transitional anvil (yellow). The black line in figure 3b shows where the cross section in figure 3c was taken. The area of the highest reflectivity in figure 3c is classified as the convective core (see horizontal bar at bottom of plot for classifications). The convective core is surrounded by stratiform classifications (green) due to echo layers returns in all three layers. Next to the stratiform regions are transitional anvil areas (yellow) that have echo layers in the mid and upper sections. Past the transitional regions is the thick anvil (blue), which only has echo layers in the upper level.

CHAPTER 3

DATA AND METHODOLOGY

3.1 Dual-Doppler Data

Dual-Doppler radar data for nine cases of varying storm type from the Severe Thunderstorm Electrification and Precipitation Study (STEPS) campaign and Colorado State University (CSU) CHILL-Pawnee radar network were used. The cases are from June of 2000 (STEPS) and July of 1998 (CHILL) in Eastern Colorado and Western Kansas. The dual-Doppler analysis provided vertical velocity fields, used for vertical mass divergence calculations. Radar reflectivity from these cases was used for ice mass calculations. Both of these calculation methods are described in subsequent sections.

There were two data sources used, a triple-Doppler network set up for the STEPS campaign and a dual-Doppler network run by Colorado State. For STEPS, a triple-Doppler network, consisting of the CSU CHILL radar near Burlington, Colorado, an NCAR S-band radar near Idalia, Colorado, and the WSR-88D radar at Goodland, Kansas, was used. The CSU CHILL-Pawnee network consisted of the CSU CHILL radar and the S-band radar at the Pawnee site. The grid spacing of the data for all cases are 1 km vertically and 0.5 or 1 km horizontally. The altitudes in all STEPS cases have been converted to above ground level (AGL) from mean sea level by subtracting 1.1 km, the height of the Goodland, KS radar; the altitudes in all CHILL cases were already in AGL. The cases used in the study were a single

cell on June 3, a convective line on June 11, a convective line on June 19, a convective line on June 22, a multicell on June 23, a supercell on June 29, a supercell on July 2, a convective line on July 15, and a multicell on July 21. All cases from June are from 2000 and data were collected as part of the STEPS campaign while the July cases are from 1998 with data collected using the CSU CHILL and Pawnee radars. An overview of the evolution of each storm is provided in chapter 4.

The goal of the STEPS field campaign was to "achieve a better understanding of the interactions between kinematics, precipitation production, and electrification in severe thunderstorms on the High Plains" (Weisman and Miller 2000). STEPS took place in western Kansas and eastern Colorado from May 17 to June 20 in 2000. The campaign took place in Kansas and Colorado since that area has a high climatological occurrence of severe storms, especially supercells, in May and June (Bluestein and Parks 1983). To accomplish the campaign goals, a wide variety of observation systems were used. Systems used included lightning mapping arrays (LMA), aircraft, balloons, mobile sounding systems, radar, and mobile mesonets.

All of the interpolation, raw data quality control, and dual-Doppler processing occurred before the start of this study. Using NCAR's Sorted Position Radar INTerpolator (SPRINT: Mohr and Vaughn 1979; Miller et al. 1986) software, the data from the radars were estimated and put onto a Cartesian grid with 1 km horizontal spacing and 0.5 or 1 km vertical spacing (Lang and Rutledge 2002). The next step taken was interpolation and velocity unfolding with CEDRIC (Tessendorf et al. 2005). CEDRIC was also used for dual-Doppler processing, in which a downward integration of the continuity equation was used to obtain vertical velocity values. This was done with data that had an average temporal

spacing of 5 minutes (Tessendorf et al. 2005). Although a triple-Doppler network was setup for the STEPS cases, only dual-Doppler processing was performed. This approach was used for the 6 STEPS cases and three CHILL-Pawnee cases (Mullendore et al. 2013).

3.2 NEXRAD Mosaic Data

The mosaic radar reflectivity dataset was from an archive of the National Severe Storm Laboratory's National Mosaic and Multi-Sensor QPE (NMQ) project. This dataset was selected to test the method with radar reflectivity from outside of the multi-Doppler networks. Raw radar data from radars across the United States from 20°N to 55°N latitude and from 130°W to 60°W longitude are merged using spatial and temporal weighting schemes (Zhang et al. 2011). The vertical grid spacing varies with height; specifically, 0.5 to 3 km has vertical spacing of 250 m, 3 km to 9 km has vertical resolution of 500 m, and 9 km to 18 km has vertical resolution of 1 km. The horizontal grid spacing of the NMQ datasets are 1 km and the temporal grid spacing is 2.5 to 5 minutes. All heights in NMQ are MSL. All available NMQ variables are listed in Table 1. The variable of primary interest for this study is the 3D mosaicked reflectivity field (MREF3D). The country is divided into eight tiles (Fig. 6), with subsets of tiles 6 (southern plains, OK, CO) and 7 (southeast, AL) being used for this project. The regions analyzed were the same domains used for the 2012 DC3 campaign: Colorado foothills, southern plains of Oklahoma and Texas, and northern Alabama. A priority case day, as defined at the 2013 DC3 PI Meeting (personal communication, Mullendore 2013), was chosen for each analysis region.

Table 1. List of NMQ products.			
ID	Unit	Update cycle	Description
UNQC_CREF	dBZ	5 min	Non-quality-controlled composite reflectivity
MREF3D	dBZ	2.5 min	3D mosaicked reflectivity field
CREF	dBZ	2.5 min	Composite reflectivity
CREFH	km MSL	2.5 min	Height of composite reflectivity
HSR	dBZ	2.5 min	Hybrid scan reflectivity
HSRH	km above ground	2.5 min	Height of hybrid scan reflectivity
ETP18	km MSL	2.5 min	Echo top of 18 dBZ
SHI	none	2.5 min	Severe hail index
POSH	%	2.5 min	Possibility of severe hail
MEHS	mm	2.5 min	Max expected hail size
VIL	kg m^{-2}	2.5 min	Vertically integrated liquid
VILD	g m^{-3}	2.5 min	VIL density
PCP_FLAG	none	2.5 min	Precipitation type
PCP_RATE	mm h^{-1}	2.5 min	Precipitation rate
Q2RAD_HSR_1(3)H	mm	2.5 min	1-h (3 h) radar-derived precipitation accumulations
Q2RAD_HSR_6(12,24, 48, 72)H	mm	1 h, at the top of the hour	6-h (12, 24, 48, 72 h) radar-derived precipitation accumulations
Q2GC_HSR_1(3,6,12, 24, 48, 72)H	mm	1 h, at the top of the hour	1-h (3, 6, 12, 24, 48, 72 h) local gauge-corrected radar precipitation accumulations
Q2GAUGE_1(3,6,12, 24, 48, 72)H	mm	1 h, at the top of the hour	1-h (3, 6, 12, 24, 48, 72 h) gauge precipitation accumulations
Q2MM_1(3,6,12, 24,48, 72)H	mm	1 h, at the top of the hour	1-h (3, 6, 12, 24, 48, 72 h) gauge-, terrain-, and climatology-based precipitation accumulations

Table 1: Taken from Zhang et al. (2011). This table details all of the NMQ products available for use. The ID used in the netCDF data files, units, temporal resolution, and a description of the data is provided.

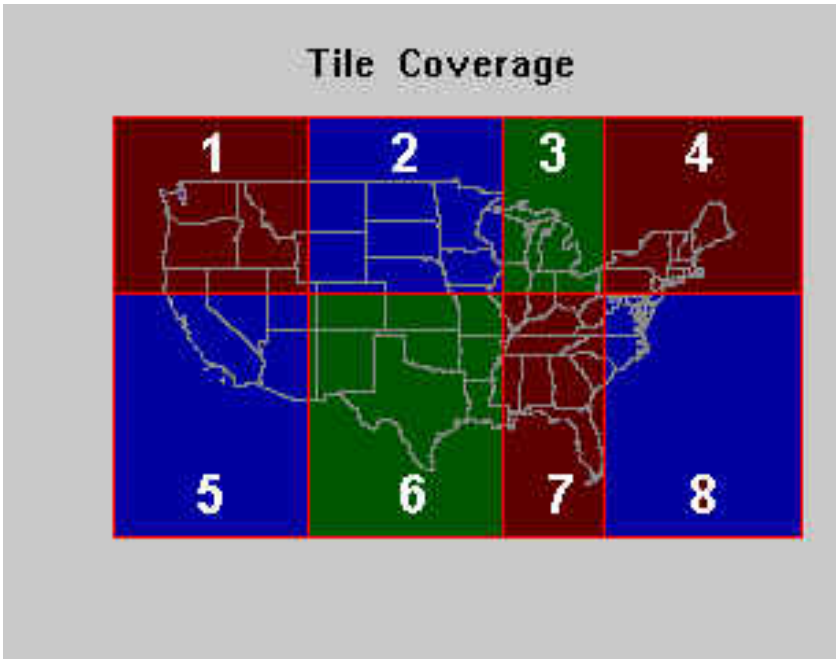

Figure 6 : Taken from: http://soar.ou.edu/legacy.html. The national NMQ mosiac is divided into eight tiles to cover the United States. This figure shows the boundaries and area of these tiles.

3.3 Vertical Mass Divergence

The goal of the project is to determine where and when mass detrainment is occurring in a variety of midlatitude storms. Direct measurements of detrainment are rare and typically only occur during field projects through the use of aircraft. The area of detrainment can be determined, as was done for part of this study, with the use of the three dimensional wind field obtained from dual-Doppler analysis. Dual-Doppler networks are uncommon outside of field projects, but data obtained from them are used in this study as a way to estimate the "true" convective detrainment such that various other methods (that do not require dual-Doppler networks) can be tested for accuracy.

Vertical velocities from a dual-Doppler analysis are used to estimate where mass is detrained and the level of maximum detrainment (Mullendore et al. 2009, 2013). Areas of detrainment were found by determining the vertical mass divergence at every altitude. Net vertical mass convergence (negative vertical mass divergence) equals net horizontal mass divergence and, therefore, convective detrainment. The level with the greatest vertical mass convergence has the greatest horizontal detrainment, which is labeled as the LMD. The range of altitudes with negative vertical mass divergence defines the detrainment envelope, which is the area where detrainment is occurring in the convective system.

Vertical mass divergence profiles were calculated for every vertical column at each grid point in the data. Then, vertical mass divergence was horizontally integrated over the entire domain at each vertical level. Vertical mass divergence is calculated using

$$\partial(\rho w)/\partial z, \tag{2}$$

where ρ is density and w is vertical velocity. This derivative is evaluated over each 500 m (or 1000 m) vertical layer in the dataset. The vertical velocity values are from the dual-Doppler analyses while density is calculated using

$$\rho(z) = \rho_0 exp(z/H) \tag{3}$$

where ρ_0 = 1.22 kg m-3, H=7 km, and z is height. Only positive velocities were used in the calculation of vertical mass divergence, since this study is only concerned with deep convective updrafts that transport mass up into the UTLS, as done in Mullendore et al. (2009). For example, in Fig. 7a, the vertical mass divergence profile from the June 3 single cell storm at 2356 UTC, the detrainment envelope (i.e. altitudes with net vertical mass convergence) is from 5 km to 11 km, and the LMD at this time is at 8.7 km.

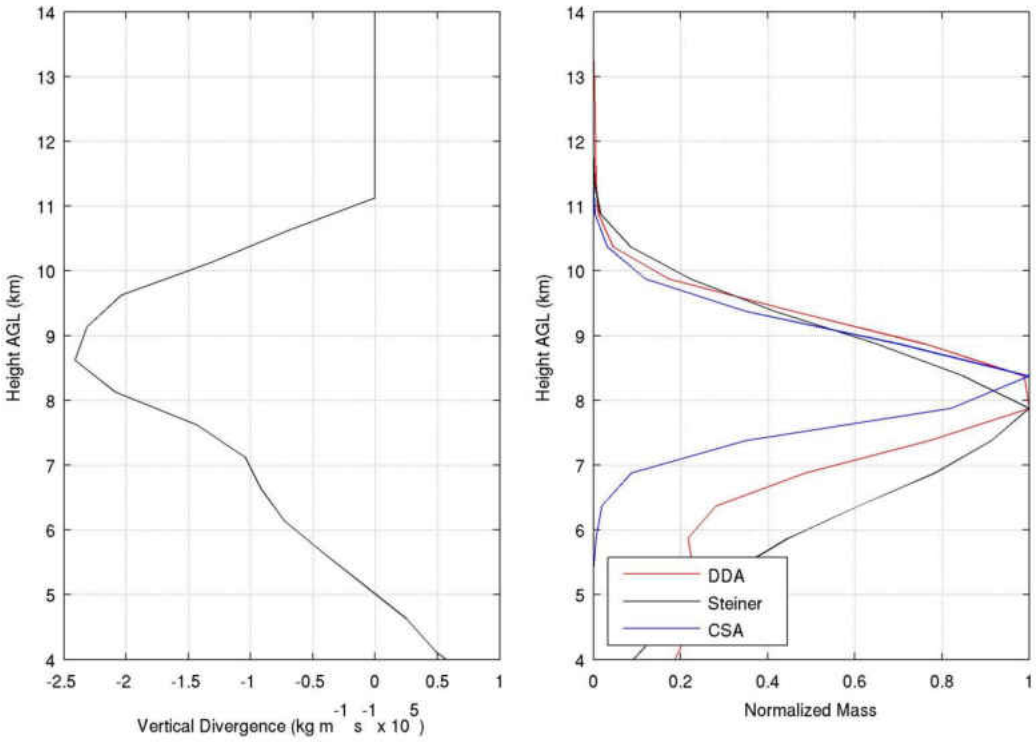

Figure 7: Mass detrainment profiles for the 2000 June 3 single cell storm at 2356 UTC, estimated using horizontally-integrated vertical mass divergence (a) and horizontally-integrated anvil mass (b). The right panel shows three different methods of anvil estimation: DDA (red line), Steiner (black line) and CSA (blue line)

3.4 Identification of Storm Regions

M09 demonstrated that radar reflectivity of convectively generated anvils could be used to estimate areas of detrainment in convection. In order to estimate the detrainment, however, the locations of the convectively generated anvils in each storm must first be determined. In this study, a convectively generated anvil location is defined as a vertical column classified as an anvil location within 10 km of a convective core, meaning that two storm regions that need to be clearly separated, these are, convective cores and anvil regions. Three different combinations of methods were used to classify these regions for this study: 1) using dual-Doppler vertical velocities to find convective cores and a simple anvil definition (named the "DDA" method), 2) using the convective/stratiform separation technique from

Steiner et al. (1995) and the simple anvil definition (named the "Steiner" method), and 3) using convective core and anvil classifications from Feng et al. (2011) (named the "CSA" method).

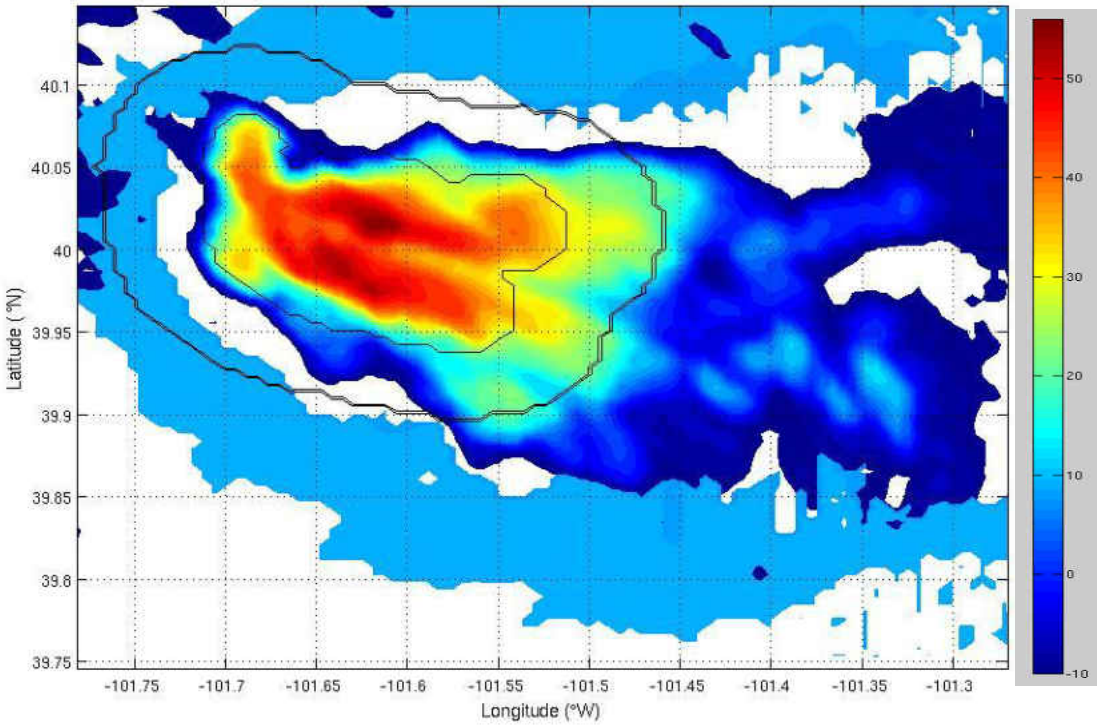

Figure 8: 2 km AGL Reflectivity from the June 3 single cell at 2356 UTC plotted with the convective (inner black line) and analysis regions (outer black line) outlined. The various sections are detailed by arrows. Light blue regions are anvil regions. Analysis anvil locations are the light blue locations within the analysis region.

To demonstrate the idea of convective anvil (hereafter the "analysis anvil"), Figure 8 shows an example of the CSA method. The convective region is outlined and then 10 km away from the edge of the convective region another outline is plotted. The colored contours represent radar reflectivity at 2 km AGL. The analysis area is in between these outlines. The light blue shading is where the CSA method found anvil, but only the anvil locations within the two outlines are analyzed, which anvils were recently generated by the convective updrafts. The other anvil locations that are farther away could be more significantly affected

than anvil locations near the convection by ice fall speed and environmental winds that can both change the altitude of the hydrometeors. Also, anvil farther than 10 km from the convective cores has a greater potential of being from non-convective sources.

3.4.1 Dual-Doppler Method

For the dual-Doppler based method, convective area is defined using the vertical velocities. Just as in the divergence calculations, only positive vertical velocities are used, since deep convective updrafts define convective cores. The average positive vertical velocity for each column was calculated, and if the average velocity was above a threshold value, the column was classified as convective. The threshold value for all storm types was 6 m/s because May and Rajopadhyaya (1998) found that intense updrafts that extend above the freezing level have updraft speeds in excess of 6 m/s. To insure that the convective area was deep and not shallow we determined that at least 60% of each potential convective column had to have values above 2 m/s to determine deep convective updrafts.

Once the convective regions had been identified, a 10 km circle was drawn around each convective region. The resulting area was the analysis region wherein anvils would be identified. For all columns in the analysis region, the simple anvil test was performed to identify anvil regions. For the simple anvil test, anvil regions were defined as regions where reflectivity echo tops were above 6 km with no reflectivity at 2.5 km (Mullendore et al. 2009; Frederick and Schumacher 2008). Figure 9a shows the reflectivity at 2356 UTC for the June

3 single cell, and figure 9b shows the classifications for the DDA method at that time.

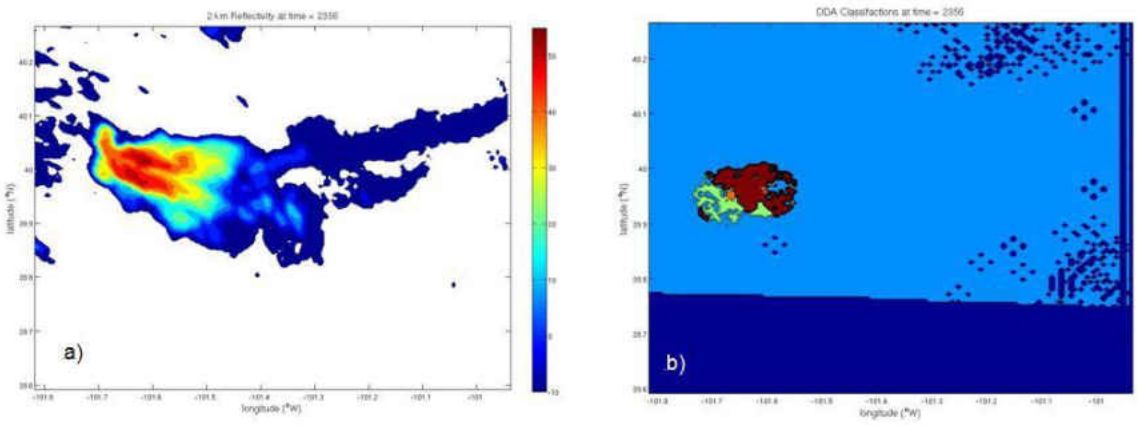

Figure 9: Radar reflectivity CAPPI at 2km for the June 3 single cell at 2356 UTC. (b) Classifications for the DDA method: orange regions are convective, red is analysis non-anvil locations, and green is analysis anvil locations.

3.4.2 Steiner Method

For the Steiner method, convective cores are identified based on the output of the Steiner et al. (1995) convective/stratiform separation technique, which uses reflectivity retrievals to classify the convective cores. See Section 2.3 for additional background on the Steiner separation technique. Once the convective cores are identified, a 10 km circle was drawn around each convective region and the simple anvil test was used to define columns that contained anvil, same as was done for the DDA method. Figure 10a shows the reflectivity at 2356 UTC for the June 3 single cell, and figure 10b shows the classifications for the Steiner method at that time. The analysis region does not cover every grid point around the convective core at this time because of locations removed in pre-processing for missing data.

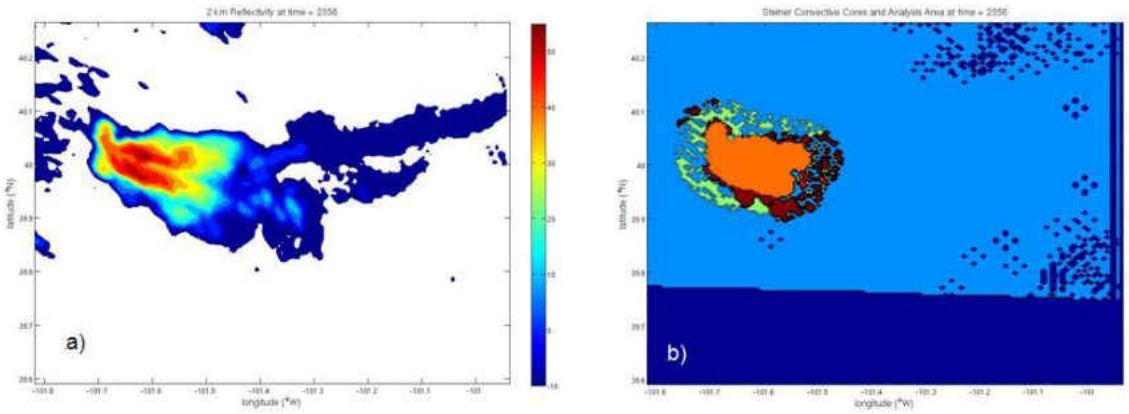

Figure 10: Radar reflectivity CAPPI at 2km for the June 3 single cell at 2356 UTC. (b) Classifications for the Steiner method: orange regions are convective, red is analysis non-anvil locations, and green is analysis anvil locations.

3.4.3 CSA Method

The final method is based on the CSA classifications from Feng et al. (2011). This classification scheme builds upon the technique by Steiner et al. (1995) by adding additional classifications for anvil types; see Section 2.3 for additional background on the CSA classification technique. Two anvil types classified by the CSA method are used in this study: ice anvil (yellow, figure 5b, c) and transitional anvil (blue, figure 5b, c). Also used for this study are the convective regions (red, figure 5b, c). As in the previous methods, once the convective regions are identified, an anvil analysis region is defined by drawing a 10-km radius around the convective area. Figure 11a provides example results for this method. Note that the convective region, and therefore the10 km swath around the convective region, is the same as that identified with the Steiner method (figure 10). Also, for this case, the CSA method has many less analysis anvil locations than the DDA method (figures 9) and the Steiner method (figure 10).

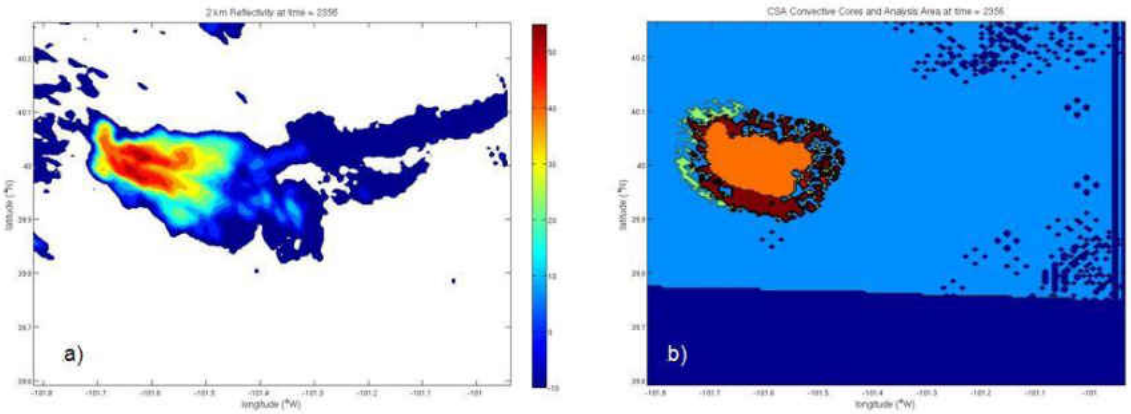

Figure 11: Radar reflectivity CAPPI at 2km for the June 3 single cell at 2356 UTC. (b) Classifications for the CSA method: orange regions are convective, red is analysis non-anvil locations, and green is analysis anvil locations.

3.5 Radar Data as a Proxy for Mass Detrainment

In order to estimate the detrainment profile from radar reflectivity, the amount of hydrometeor mass in the analysis anvil must be estimated. But before mass can be estimated from radar reflectivity, it was found that additional pre-processing must be applied to mitigate various structures that produced errors in detrainment estimates. Sources of error are removed via pre-processing are: single grid point convective classifications, data quality at the edges, and missing data in the vertical column.

3.5.1 Convective Classification Pre-Processing

Due to the use of reflectivity threshold values within the CSA and Steiner methods, isolated regions containing one or two grid points are occasionally classified as convective due to an isolated high reflectivity return. Figure 10b provides example of this problem, as there is an isolated convective grid point near -101.55°W, 39.48°N. This same point that is labeled as convective for figure 5b does not look like a convective element on figure 10a. It is unlikely that a deep convective updraft that will be detraining mass in the UTLS will have a radar reflectivity based convective region less than 2 km across, as radar reflectivity based

convective regions are usually larger than the actual updraft (Steiner et al. 1995). To remove these erroneous convective regions from the analysis, all convective cores must have at least 2 other convective classification points contiguously to the north, south, east, or west.

3.5.2 Horizontal and Vertical Gradient Pre-Processing

Sharp gradients near missing data values in both the horizontal and vertical can cause erroneous results. These sharp gradients are caused because data were removed from the original data set. To deal with sharp horizontal gradients, data within 2 km of the edges of the analysis were removed due to frequent missing or incorrect data. The June 11 convective line from the STEPS campaign provides an example of these sharp gradients.

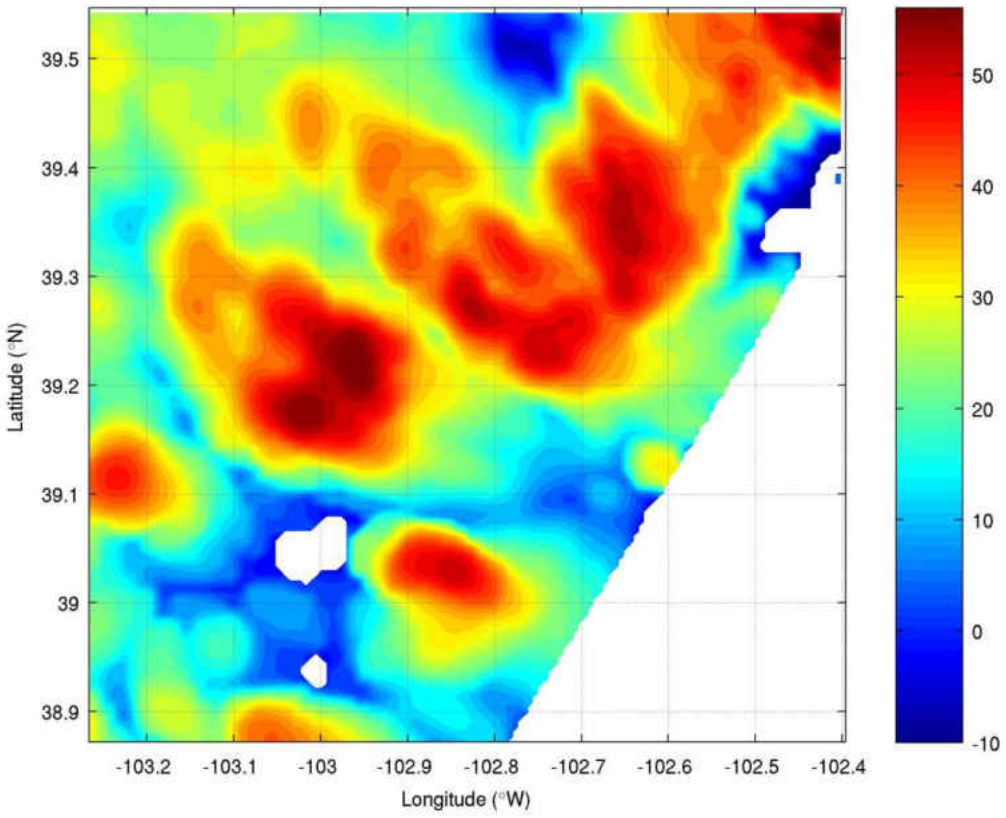

Figure 12: A 2 km constant altitude plot of reflectivity for the June 11 Convective Line at 2225 UTC.

Along the eastern edge of the reflectivity data shown in Fig. 12 is an anomalous pattern that is not representative of the actual reflectivity field. Such patterns arise owing to missing or removed data grid points. A clear air return that is not a result of missing or removed grid points is present at -103°W, 39.05°N.

Next, columns with missing data were masked out. This was done because missing data can lead to incorrect classifications. In Fig. 13, the unphysical structures in the northeast sector of the plot are artifacts resulting from missing data and have nothing to do with actual storm structure.

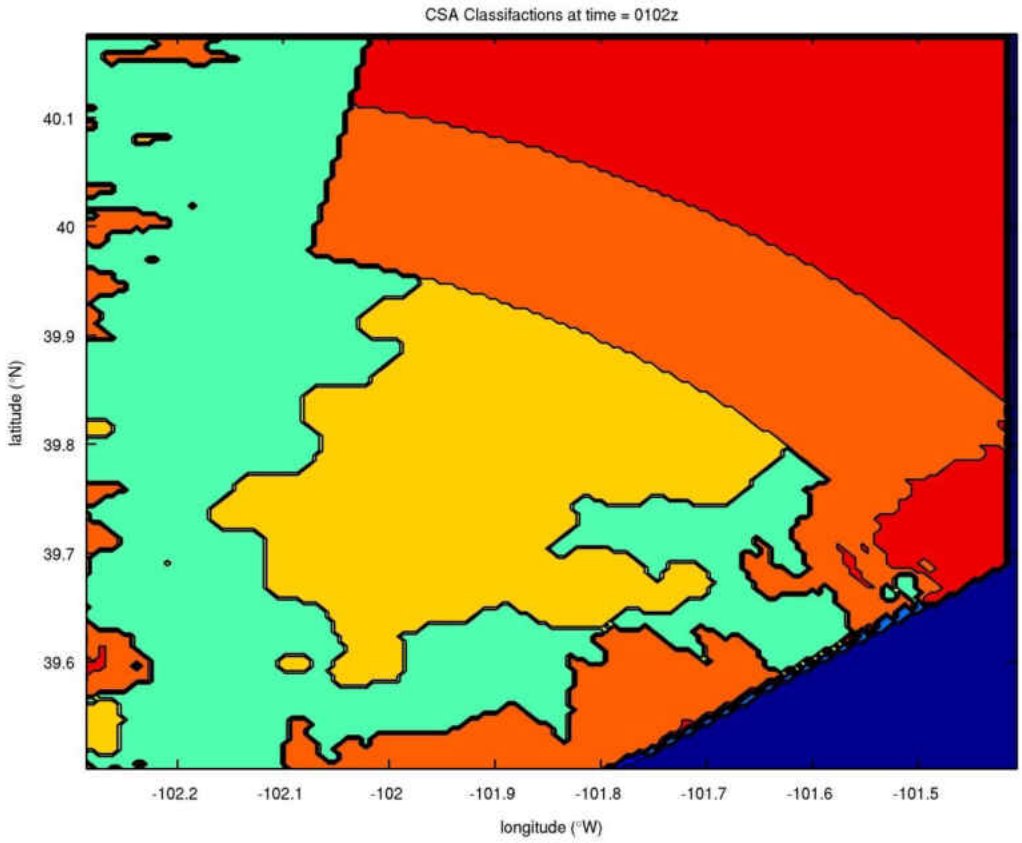

Figure 13: CSA classifications for the June 22 convective line at 0102 UTC. The convective cores are yellow, stratiform regions green, transitional regions orange, mixed anvil light red, ice anvil dark red, and the blue regions low clouds or no data.

Figure 14 shows the resultant ice mass detrainment envelope before (14c) and after (14b) removing bad columns from the reflectivity data. Even though after the bad columns are removed the method does not exactly match the "true" detrainment profile (14a), the corrected profile is much closer to truth both from the standpoint of the LMD and profile shape.

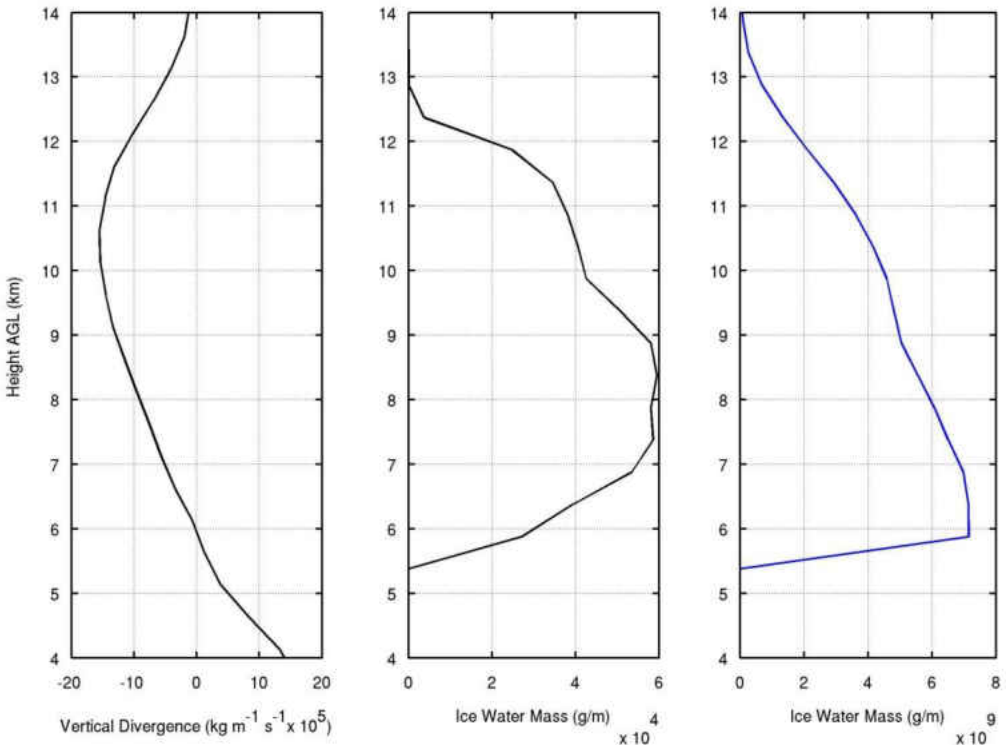

Figure 14: Mass detrainment profiles for the 2000 June 22 convective line at 0102 UTC, estimated using horizontally-integrated vertical mass divergence (a) and horizontally-integrated CSA anvil mass (b,c). b) has missing data columns removed while c) does not have the columns removed.

The columns with missing data were located by identifying sharp gradients of reflectivity at the top and/or bottom of the anvil location echo next to missing data values. An example of vertical columns that would be removed from the June 22 case at 0102 UTC is shown in Fig. 15, in much of the data below 3 km is missing. This is especially troubling for the CSA classification as it uses 3 km as its low limit during classification. The missing

data lead to an over classification of anvil regions as shown in figure 13(red contours).

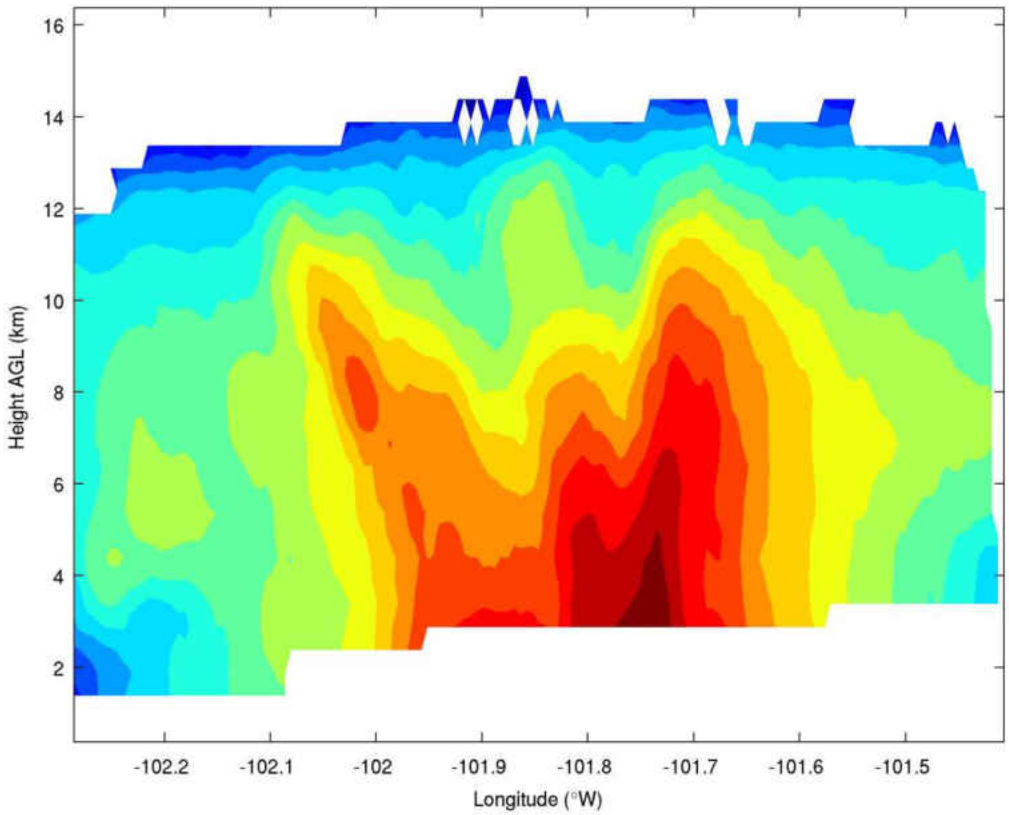

Figure 15: A vertical cross section of the June 22 convective line at 0102 UTC. All white space represents missing data or no data locations.

To remove missing data locations a gradient method was used since sharp gradients (i.e. going from no data to 20 dBZ at the next grid point) implies missing data and not a location where there was no retrieval due to absence of hydrometeors. The gradient check method needed to be applied since "missing data" (i.e. no retrieval) and "no data" (i.e. no hydrometeors) were coded using the same missing data value in the datasets. If the echo top or echo bottom values were above 5 dBZ then the column was removed. The value of 5 dBZ was determined subjectively based upon analysis of data holes in the nine cases analyzed. This can be seen in Figs. 10 and 11 as some locations within 10 km of a convective core are

not red analysis regions. Even if a grid point is within 10 km of a convective point it can be removed as an analysis location due to a failure of the gradient check.

3.5.3 Ice Mass Calculation

Once all of the anvil regions within the analysis area were identified, the anvil ice mass was summed. The anvil mass was calculated by converting effective reflectivity to ice water content (I) using equation 1 where ZI is the effective radar reflectivity from ice precipitation (Ze + 6.7 dBZ).

Since anvil was the focus of this study, the area summed in each column is from the -10 dBZ echo top down to the first -10 dBZ echo bottom; -10 dBZ is the same threshold used in the CSA algorithm. All data below 4 km were removed since they would likely not be ice and (3) would no longer be valid. The 4 km level was picked subjectively based upon an analysis of the soundings near the storms from the nine cases. Studies taking place at different locations or at different times of the year would likely need to pick a different level. Finally, if fewer than ten analysis anvil columns are identified with a given method, then nothing is computed at that time for that particular method. This number was determined via testing different threshold values for the nine cases. A time with fewer than ten analysis anvil locations produced much more variable results that did not match up with the other times or vertical mass divergence LMDs. Typically, LMDs for times having less than ten analysis anvil locations would be either too high or low by 3 km or more.

Ice mass is summed at each level to create vertical mass profiles at each time; example mass profiles created using each method are shown in Fig. 7b. For each case, averaged profiles are calculated by summing the mass at each height for all times and

dividing by the number of valid times. This was compared against a vertical mass divergence plot of the average values from all times (valid and not valid from mass methods).

CHAPTER 4

RESULTS AND DISCUSSION

4.1Method Comparison

In this section a best method to find the level of maximum detrainment (LMD) using reflectivity as a proxy will be determined. Three methods are compared: Dual-Doppler based convective cores with simple anvils (DDA), Steiner et al. (1995) convective cores with simple anvils (Steiner), and Feng et al. (2011) Convective Stratiform Anvil (CSA). The convective and anvil locations for the three methods were applied to STEPS and CSU-CHILL datasets with additional pre-processing as described in section 3.5. Once the anvil locations were identified, the masses of anvils located near convective cores were calculated based upon reflectivity as described in section 3.5. The focus of the analysis is on the altitudes of the maximum mass values and shapes of the vertical mass profiles, so all three methods were normalized based upon their respective maximums. These derived mass profiles are then compared to dual-Doppler derived vertical mass divergence plots. The LMD for the mass plots is the altitude in the upper-troposphere/ lower-stratosphere (UTLS) where the largest amount of mass exists. The LMD for the vertical mass divergence plots is at the minimum value level since vertical mass convergence (i.e. negative divergence) implies horizontal detrainment. As discussed in chapter 3, each method produced a result at a given time only if the required number of anvil locations was exceeded at that time. A given method is deemed a “good” performer if the radar-reflectivity-estimated LMD for that

method is close in altitude to the mass divergence estimated LMD, which is assumed to be "truth". Nine cases of varied storm type were analyzed from the STEPS campaign and CSU-CHILL/CSU-Pawnee Doppler radar network (Table 2).

	Div-DDA (km)	Div-Steiner (km)	Div-CSA (km)
June 3 Single Cell	0.98 (43%)	0.82 (0.82%)	0.51 (100%)
June 11 Convective Line	0.58 (43%)	1.33 (43%)	2.00 (29%)
June 19 Convective Line	- (0%)	- (0%)	0.25 (29%)
June 22 Convective Line	2.09 (100%)	2.05 (100%)	1.31 (91%)
June 23 Multicell	3.25 (14%)	2.00 (14%)	0.93 (100%)
June 29 Supercell	2.61 (100%)	2.75 (100%)	1.25 (100%)
July 2 Supercell	3.50 (21%)	3.50 (21%)	1.64 (100%)
July 15 Convective Line	2.75 (50%)	2.64 (50%)	1.40 (36%)
July 21 Multicell	4.75 (14%)	4.75 (14%)	3.90 (36%)

Table 2 The difference in height between the vertical mass divergence based LMD and the method based LMDs for all nine cases. The number in parenthesis is for the percentage of times that had analysis anvil locations for each method.

The nine cases are presented individually in the following subsections, which are followed by a summary of the comparison results.

4.1.1 June 3 Single Cell

On 3 June 2000 the data were collected from a single cell storm as part of the STEPS campaign. The analysis began at 2301 UTC on June 3 with a developing single cell thunderstorm. This storm developed quickly and become mature at the next time step of 2304 UTC (Tessendorf et al. 2007). The storm had a well-defined developed anvil before it began

to dissipate at 0032 UTC. Figure 16 shows a constant altitude plot of the storm at 2356 UTC when the storm was mature and well developed.

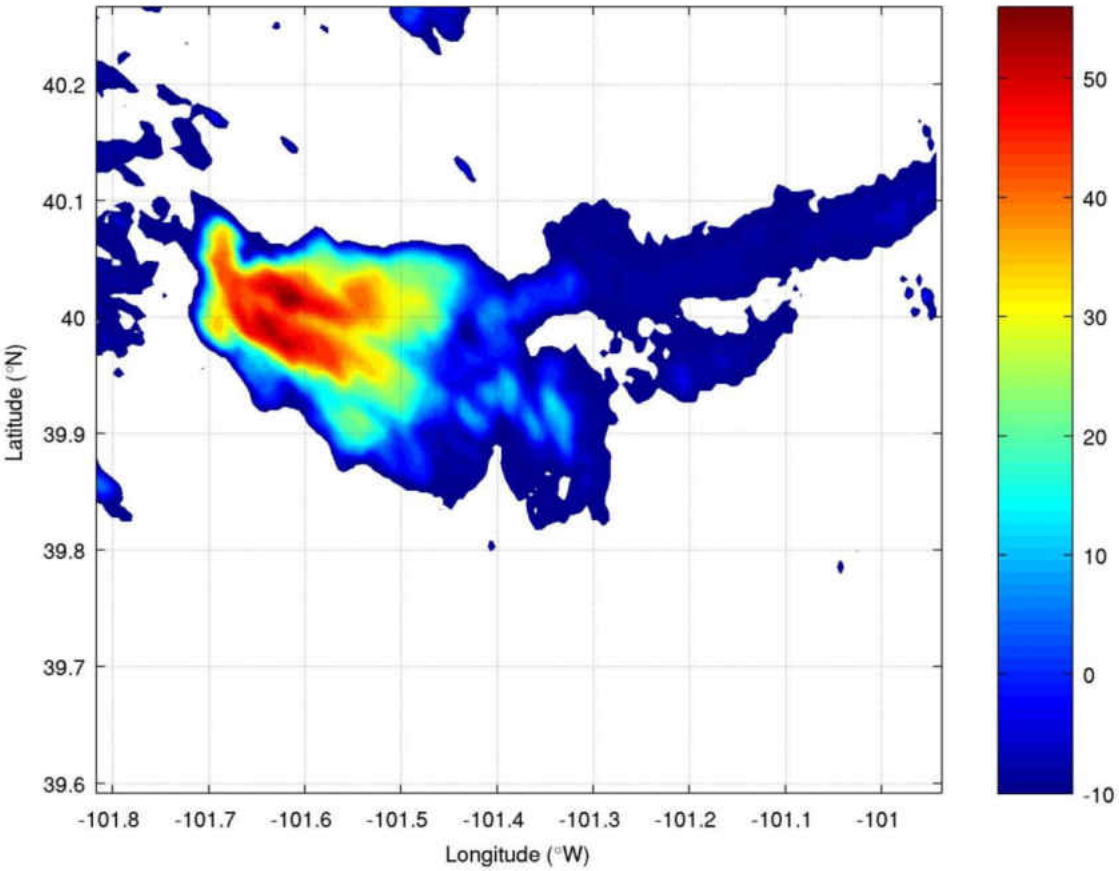

Figure 16: Radar reflectivity at 2km for the June 3 single cell case at 2356 UTC.

The CSA method passed the threshold for anvil locations for all times analyzed and the mass-derived LMD lines up well with the vertical mass divergence LMDs (Fig. 17).

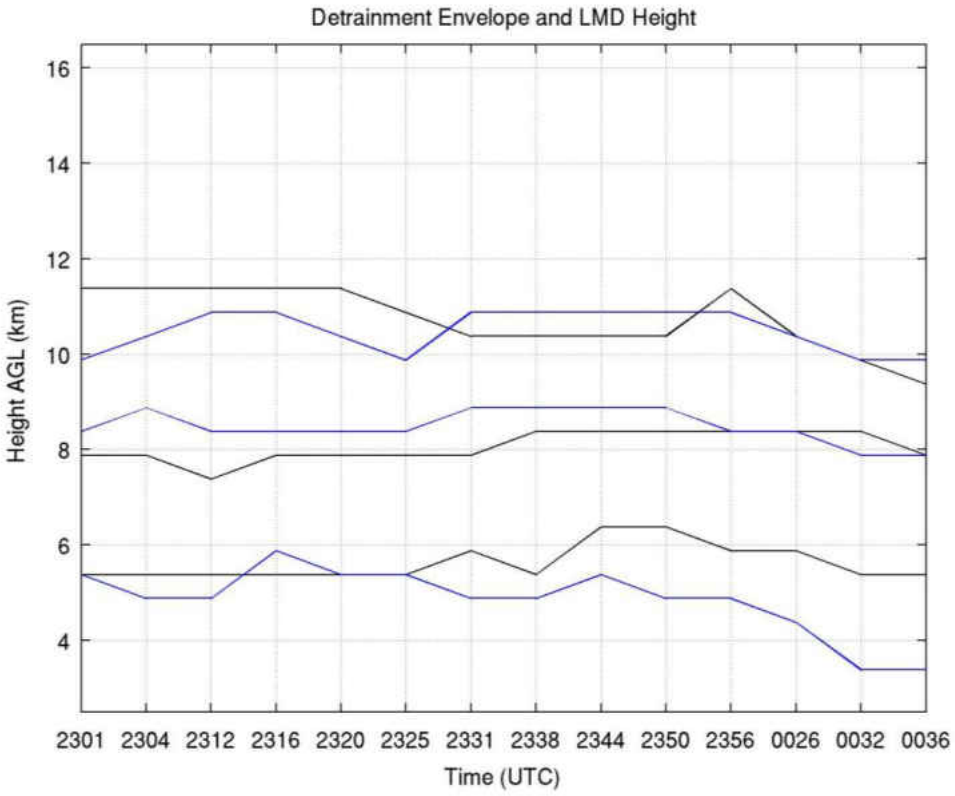

Figure 17: A plot of the upper envelope (top two lines), LMD (middle two lines), and lower envelope (lower two lines) height for the June 3 STEPS single cell case. Blue lines are for the vertical mass divergence and black lines are for the CSA ice mass.

The DDA and Steiner methods exceeded the threshold for anvil locations for six of the times (43%). Figure 18 shows the divergence LMD (left panel) and mass LMD (right panel) for all three methods at 2356 UTC. Although the DDA and Steiner methods provide results for less than 50% of the times, all three methods produced results that were very similar, and, with the exception of one analysis time, the methods never produced LMDs that differed by more than 0.5 km. When all three methods passed the threshold for anvil locations, the CSA method was either closest to the divergence LMD or tied with another method. The average distance from the vertical-mass-divergence-based LMD was the lowest for the CSA method (Table 2).

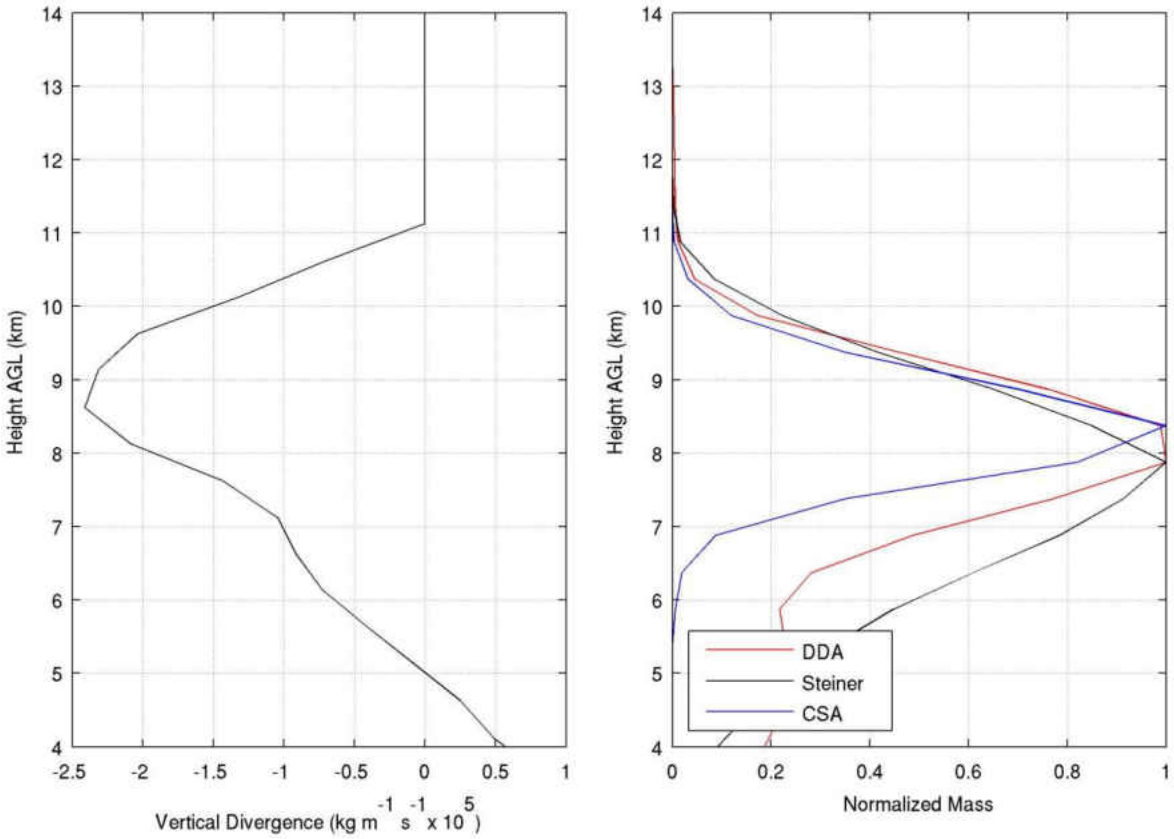

Figure 18: Mass detrainment profiles for the 2000 June 3 single cell storm at 2356 UTC, estimated using horizontally-integrated vertical mass divergence (a) and horizontally-integrated anvil mass (b). b) shows three different methods of anvil estimation: DDA (red line), Steiner (black line) and CSA (blue line)

4.1.2 June 11 Convective Line

On 11 June 2000 the data were collected from a convective line as part of the STEPS campaign. For this analysis, two times were sampled, once when the storm was a cluster of cells close together from 2200 to 2240 UTC and later when it formed into a bowing convective line from 0007 to 0045 UTC. Figure 19 from 2213 UTC and Fig. 20 from 0037 UTC demonstrate the significant difference in the storm's structure during these two periods.

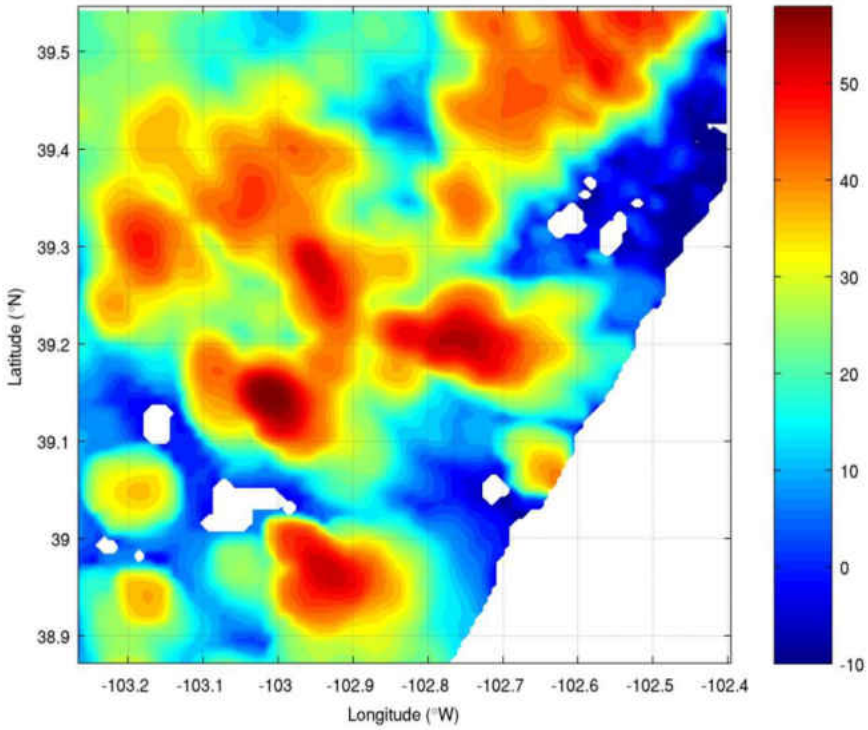

Figure 19: A horizontal radar reflectivity slice of the June 11 STEPS convective line at 2213 UTC at 2 km while it was more multicellular.

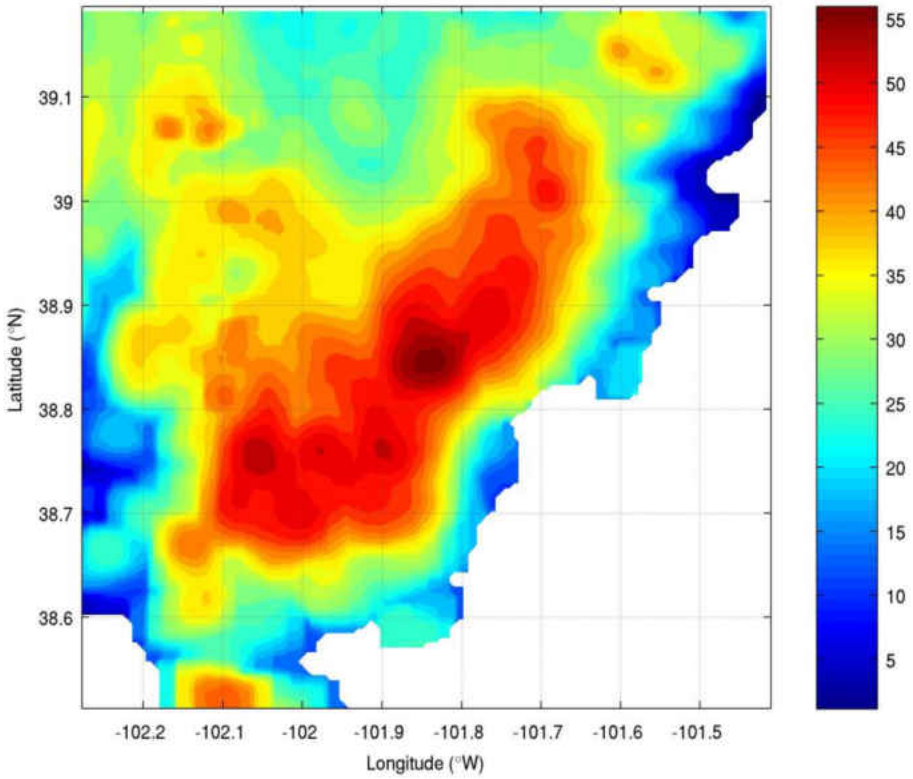

Figure 20: Radar reflectivity at 2km for the June 11 convective line at 0037 UTC (technically June 12 at this point).

A large and persistent single cell was present towards the end of this storm's lifetime, as noted in Mullendore et al. (2013). In contrast to the single cell results, the CSA method only passed the threshold for anvil locations for three times for this case (29%, Table 2). The DDA and Steiner methods passed the threshold for anvil locations at 6 of the times (43%). The three times that the CSA method passed the threshold for anvil locations the other two methods did not. At the three times that the CSA method found qualifying anvil, it did not perform well. An example is provided in Fig. 21.

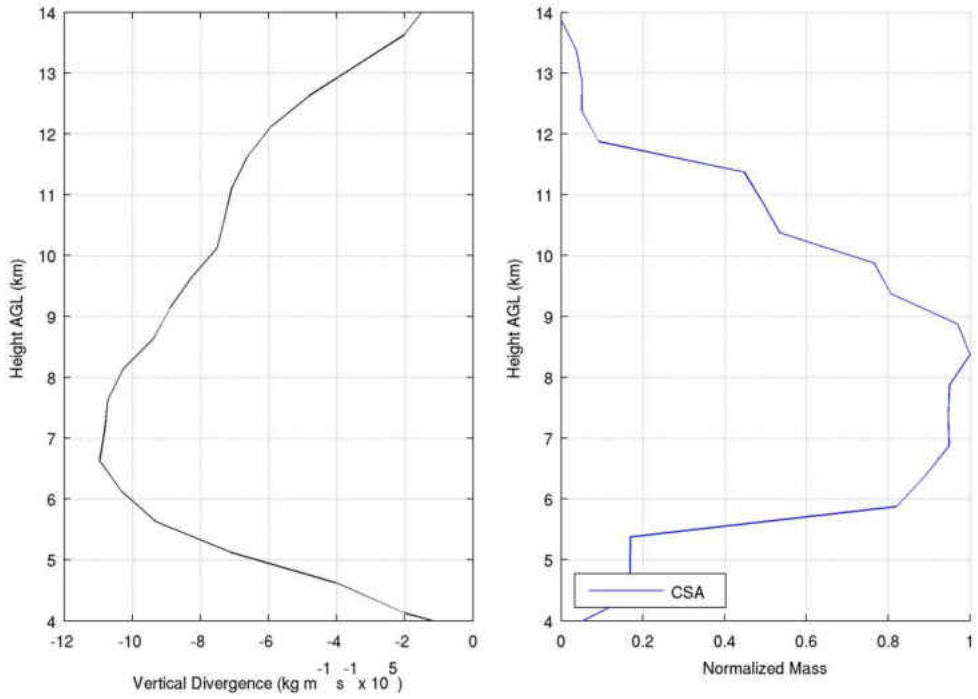

Figure 21: Mass detrainment profiles for the 2000 June 11 convective line at 0012 UTC, estimated using horizontally-integrated vertical mass divergence (a) and horizontally-integrated anvil mass (b). b) shows the only method of anvil estimation that passed the threshold, CSA (blue line).

The CSA mass LMD is higher at this time than the vertical divergence LMD. In contrast, the DDA method performs well for this case, as seen in Fig. 22 (red line). The average distance from the vertical-mass-divergence-based LMD was lowest for the DDA method (Table. 2). When the DDA method performs well it is because it found additional convective regions

that the CSA method missed. This is shown in Fig. 22, since the DDA line has an LMD much closer to the mass divergence LMD than the LMD produced using the Steiner method. For Fig. 22, CSA had too few analysis anvil locations and therefore was not plotted. This is the only case in which the CSA did not perform the best.

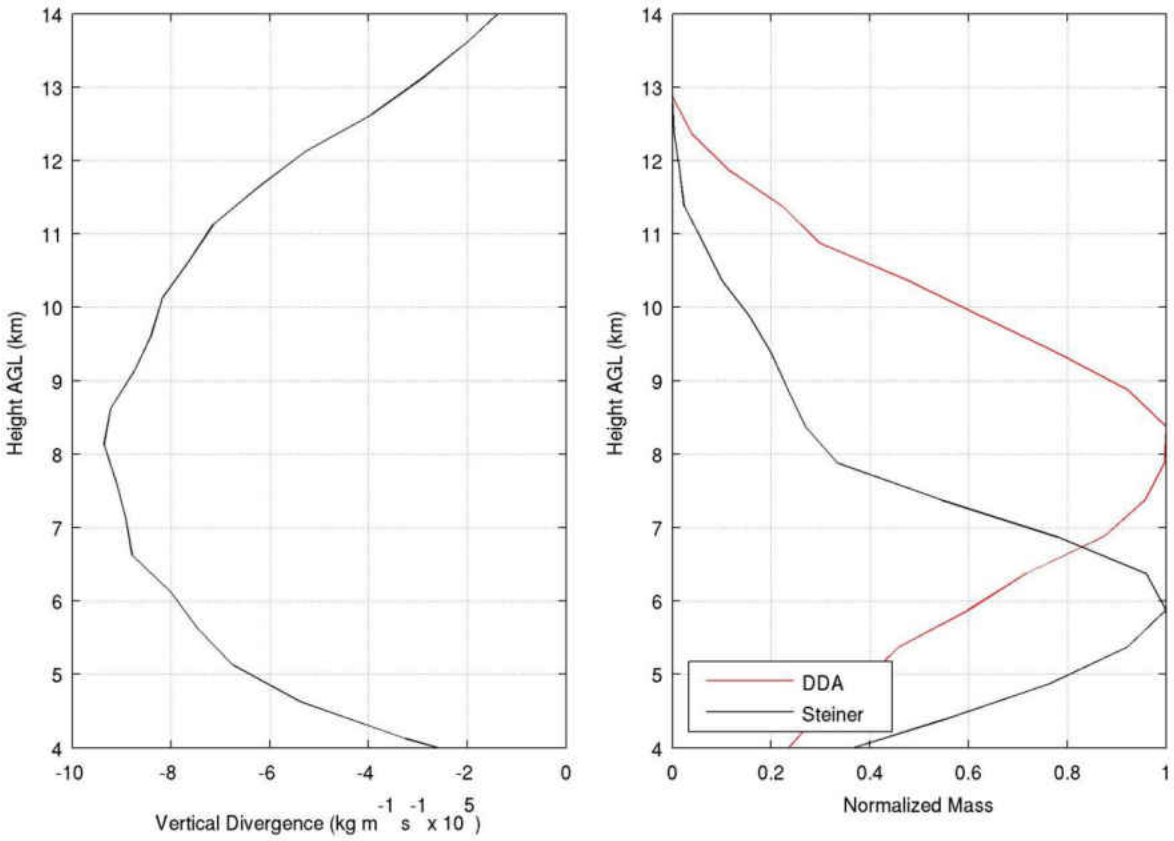

Figure 22: Mass detrainment profiles for the 2000 June 11 convective line at 2200, estimated using horizontally-integrated vertical mass divergence (a) and horizontally-integrated anvil mass (b). b) shows three different methods of anvil estimation that passed the threshold: DDA (red line) and Steiner (black line).

4.1.3 June 19 Convective Line

On 19 June 2000 the data were collected from a convective line as part of the STEPS campaign, although for the times sampled, the storm was still in its developing stages. Therefore, as seen in Fig. 23, which is for one of the final times sampled, the line had not formed yet.

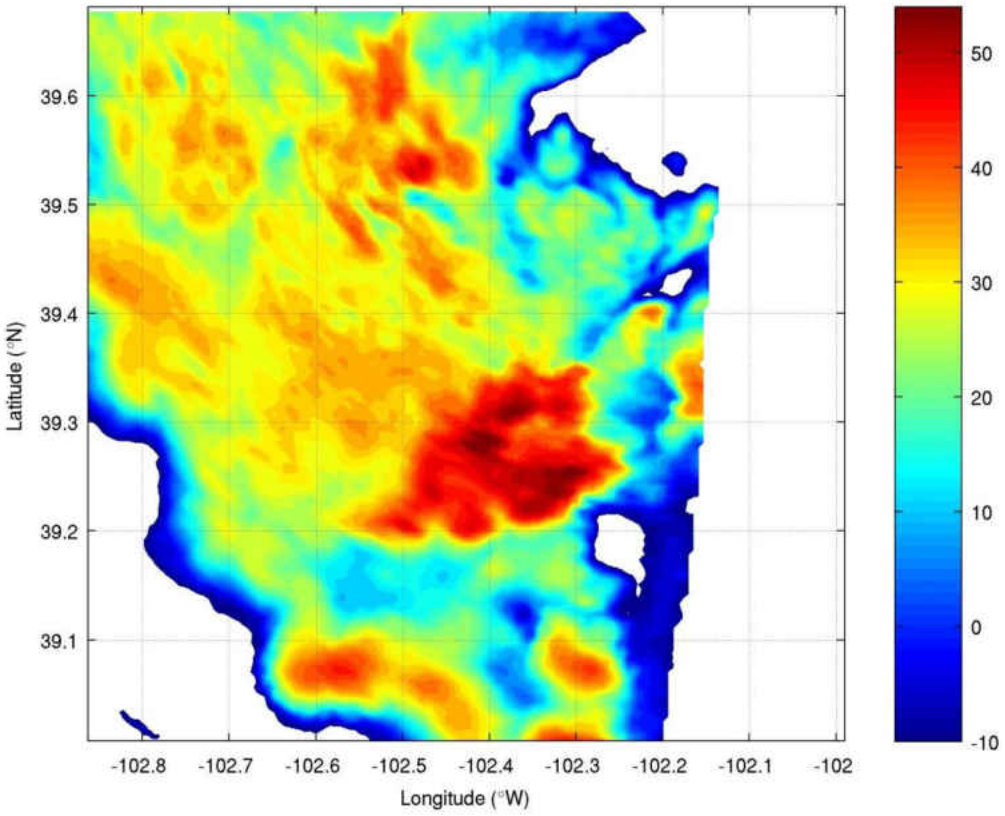

Figure 23: Radar reflectivity at 2km for the June 19 convective line at 0038 UTC.

For this case all three methods struggled significantly. The DDA and Steiner methods did not meet the threshold for anvil locations at any time for this case. The CSA method only met the threshold for anvil locations at four times for this case (29%, Table 2). For the times that the CSA method met the threshold, only two of those times produced LMD altitudes that were close to the divergence derived LMD and an example of the mass plot for one of those times is figure 24. Those two times were the final two sampling times, when the storm had a large mature cell (Fig. 23; high reflectivity core southeast of center). Earlier, the storm was characterized by small cells that had little detectable anvil.

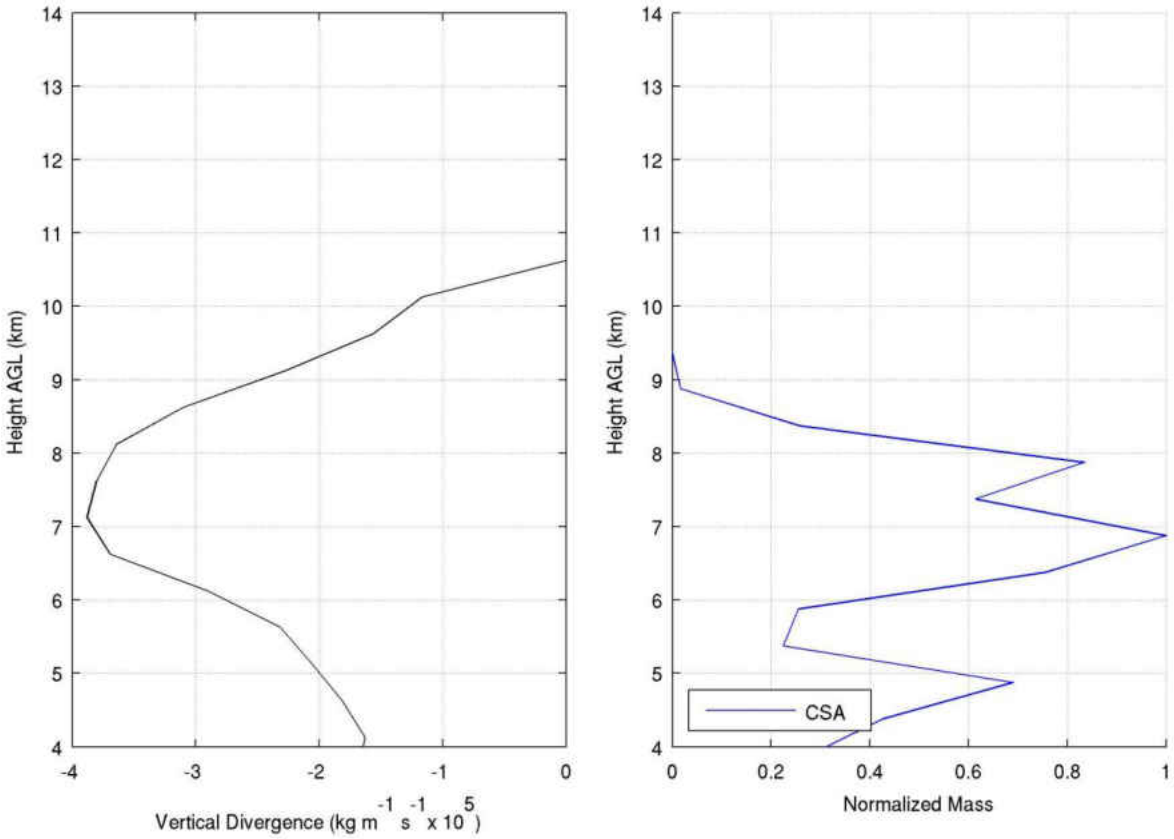

Figure 24: Mass detrainment profiles for the 2000 June 19 convective line at 0032, estimated using horizontally-integrated vertical mass divergence (a) and horizontally-integrated anvil mass (b). b) shows the only method of anvil estimation that passed the threshold, CSA (blue line).

On average, the difference between the mass divergence and CSA LMDs was only 0.25 km. Much of the difficulty with this case was due to missing data at the top and bottom of the vertical column, an example of which is provided in Fig. 25. These missing data caused a significant portion of the radar retrievals to be thrown out in pre-processing, the approach to which is discussed in section 3.5.

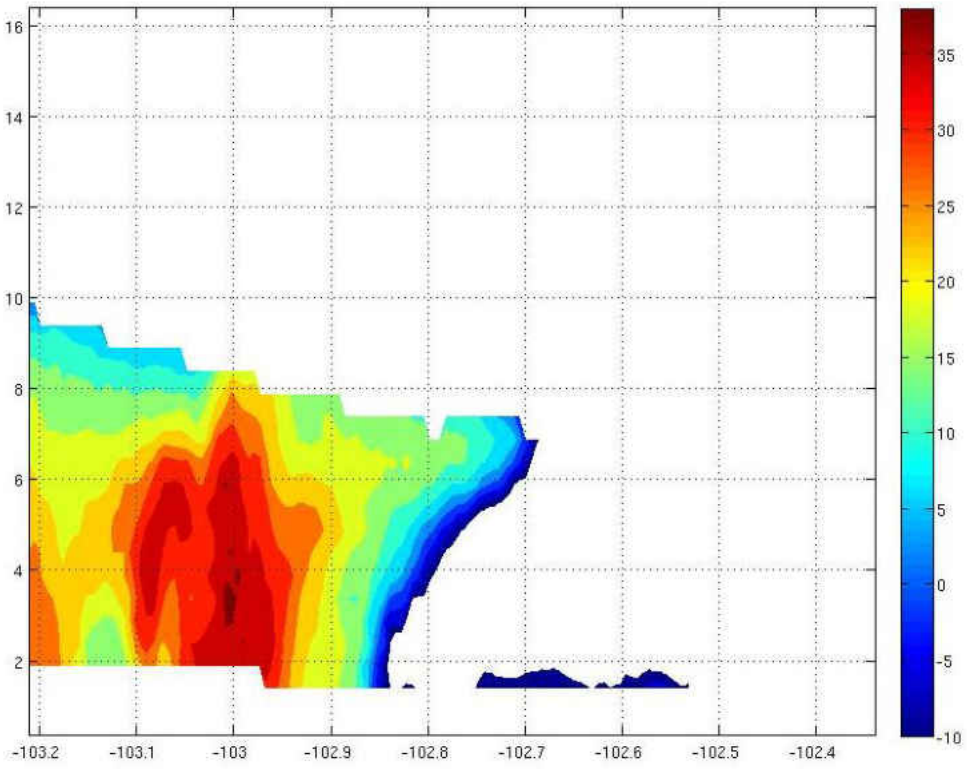

Figure 25: Vertical cross section of reflectivity for the June 19 storm.

4.1.4 June 22 Convective Line

On 22 June 2000 the data were collected from a convective line as part of the STEPS campaign. During the analysis period this storm was a persistent and well-defined convective line that propagated from west to east, as shown in Fig. 26. A significant amount of data was missing in the lower levels for this case, which resulted in some convective cores and anvil locations being thrown out, as discussed in section 3.5 and shown in Fig. 13. For some analysis times, this pre-processing step removed most of the convective and anvil locations. Although many potential analysis areas were removed, 100% of times for DDA and Steiner, while 91% of times for CSA passed the anvil threshold.

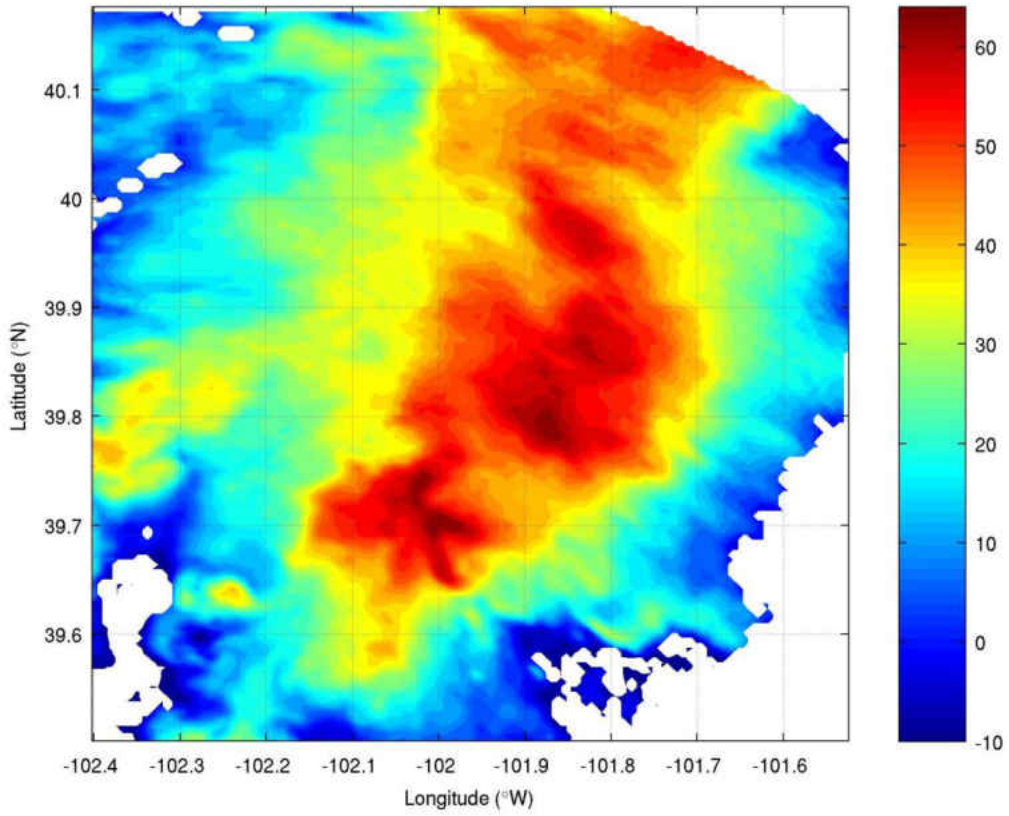

Figure 26: Radar reflectivity at 2km for the June 22 convective line at 0054 UTC.

For half of the times analyzed, the three methods produced very similar results, such as shown in Fig. 27b. However, for the other times one method would significantly outperform the other two. For example, the CSA method, although still under-predicting the "true" LMD, clearly outperforms the DDA and Steiner methods at 0035 UTC (Fig. 28). Although the DDA and Steiner methods did outperform CSA at individual times, CSA outperformed the other methods on average (Table 2).

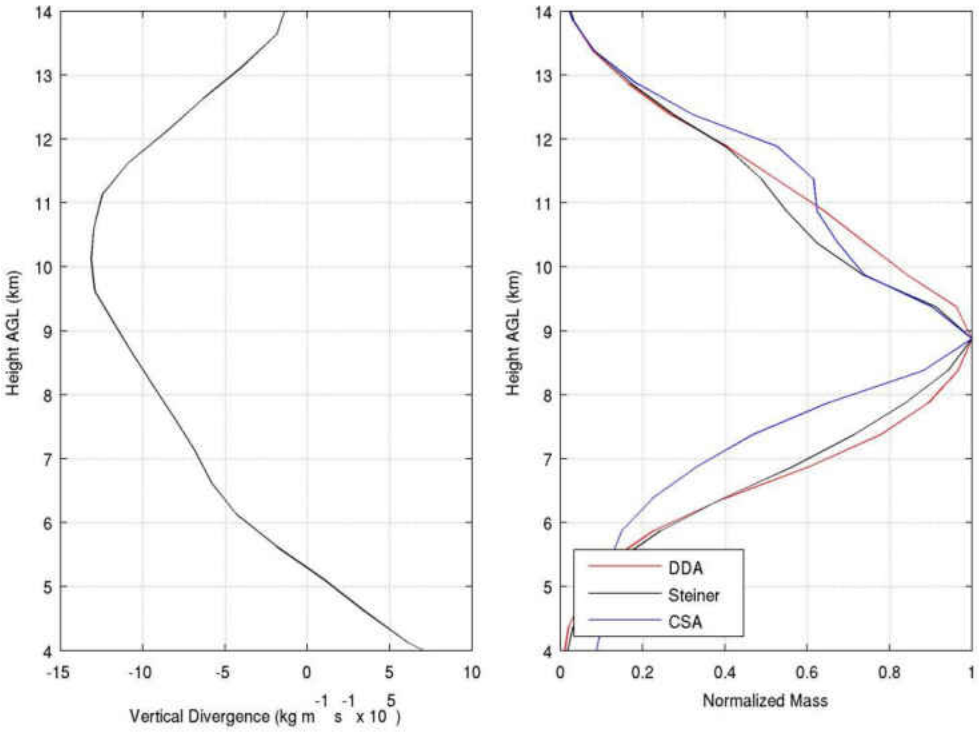

Figure 27: Mass detrainment profiles for the 2000 June 22 convective line at 0015 UTC, estimated using horizontally-integrated vertical mass divergence (a) and horizontally-integrated anvil mass (b). b) shows three different methods of anvil estimation: DDA (red line), Steiner (black line) and CSA (blue line)

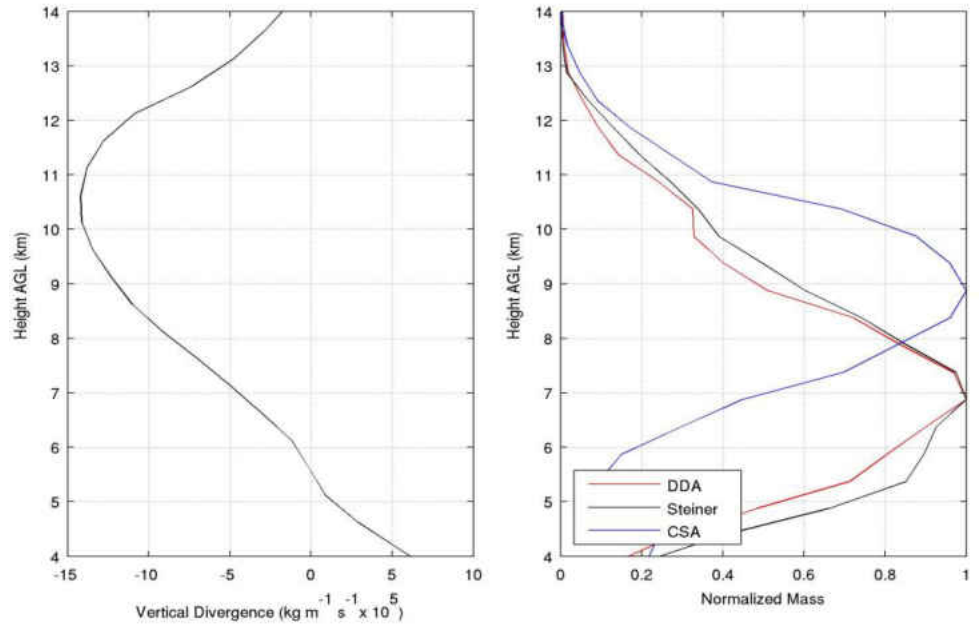

Figure 28: Mass detrainment profiles for the 2000 June 22 convective line at 0035 UTC, estimated using horizontally-integrated vertical mass divergence (a) and horizontally-integrated anvil mass (b). b) shows three different methods of anvil estimation: DDA (red line), Steiner (black line) and CSA (blue line)

4.1.5 June 23 Multicell

On 23 June 2000 the data were collected from a multicell as part of the STEPS campaign. A few cells developed and remained relatively stationary during the analysis period. Although this is a multicell case, the cells are arranged linearly, as shown in Fig. 29, so it was easier to identify anvil locations since there was not as much anvil overlap as with other cases.

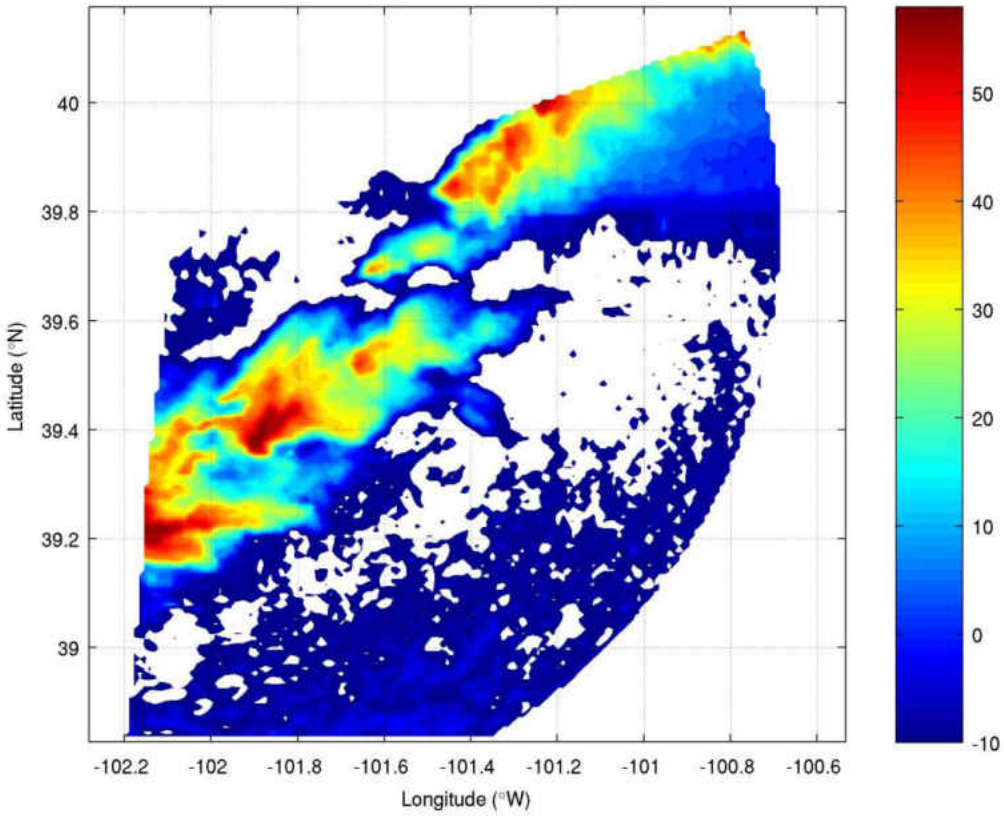

Figure 29: Radar reflectivity at 2km for the June 23 multicell case at 2206UTC.

For this case the DDA and Steiner methods only passed the threshold for anvil locations values for 14% of the times while the CSA method provided results at all times. With the exception of a secondary maximum for the DDA method at 2140 UTC, the DDA method struggled (Fig. 30).

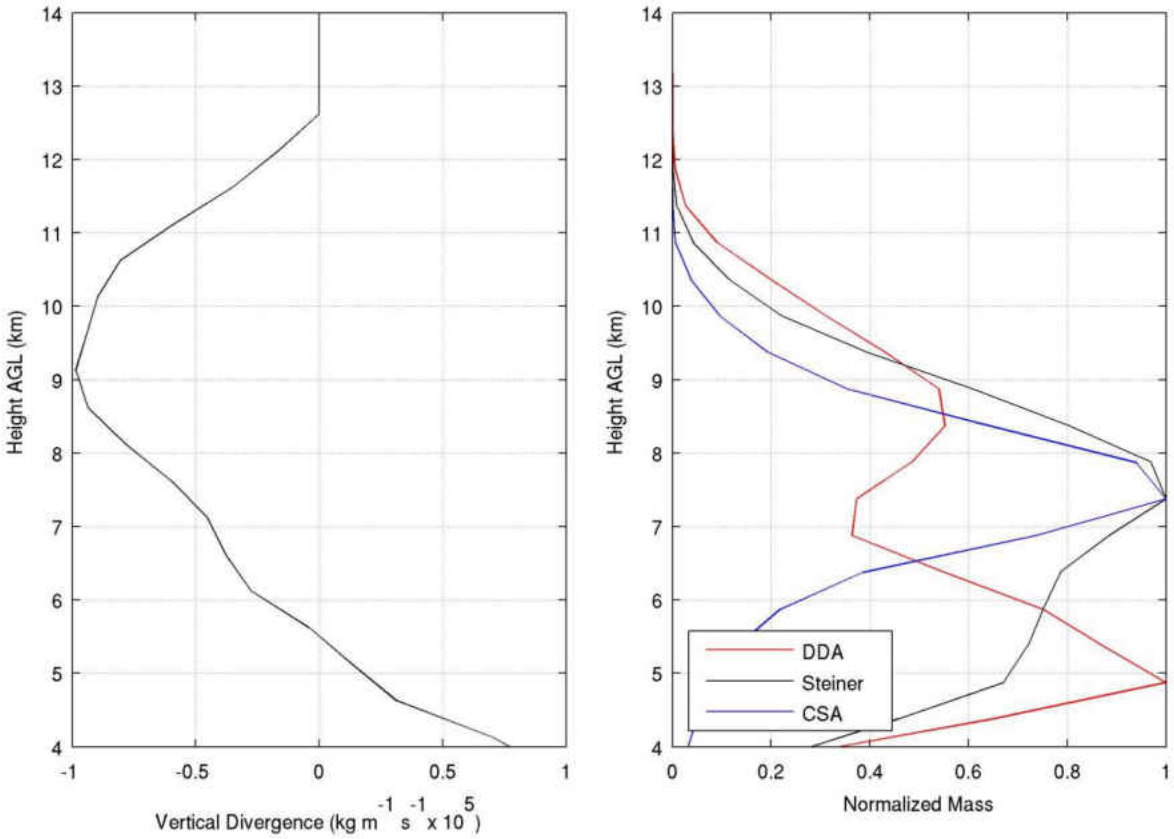

Figure 30: Mass detrainment profiles for the 2000 June 23 multicell at 2140 UTC, estimated using horizontally-integrated vertical mass divergence (a) and horizontally-integrated anvil mass (b). b) shows three different methods of anvil estimation: DDA (red line), Steiner (black line) and CSA (blue line).

For the Steiner method the main problem was the small percentage of times that had enough anvil detected (Tbl. 2). Although all three methods produce similar results in Fig. 30, the CSA method outperforms the other two at all other times, especially since most times have no result for DDA or Steiner. Figure 31 shows the evolution of the LMD based on the CSA method versus that obtained using vertical mass divergence. The two LMD values are relatively close at all times. The average distance from the vertical-mass-divergence-based LMD was the lowest for the CSA method, which outperformed the other methods by more than 1 km on average (Table 2).

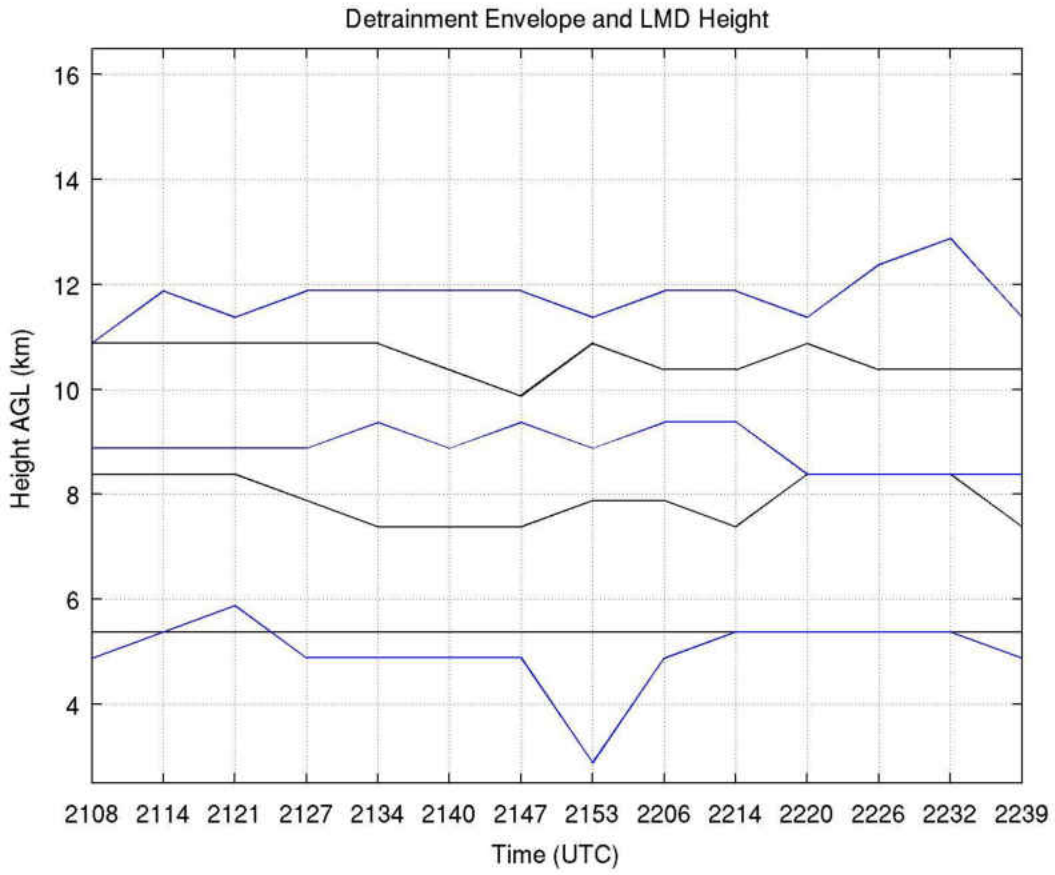

Figure 31: A plot of the upper envelope (top two lines), LMD (middle two lines), and lower envelope (lower two lines) height for the June 23 STEPS multicell case. Blue lines are for the vertical mass divergence and black lines are for the CSA ice mass.

4.1.6 June 29 Supercell

On 29 June 2000, the data were collected from a supercell as part of the STEPS campaign. At all times sampled for this analysis, the supercell was mature, but, at 2325 UTC, the storm became a pronounced right-mover with a tornado touchdown at 2328 UTC (Tessendorf et al. 2005). After turning right, the supercell maintained a strong updraft, and a constant altitude plot of reflectivity (Fig. 32) shows the structure of a classic supercell. Supercells, with their intense updrafts, have been found to have higher LMDs than other storm types (Mullendore et al. 2005, 2013). For this case, the divergence based LMDs ranged from 10-13 km. Generally the CSA method performed the best for finding the higher anvil

levels. The DDA and Steiner methods rarely identified an LMD above 9 km while, while CSA LMDs were above 9 km for the majority of the times. The average distance from the vertical-mass-divergence-based LMD was the lowest for the CSA method (Table 2).

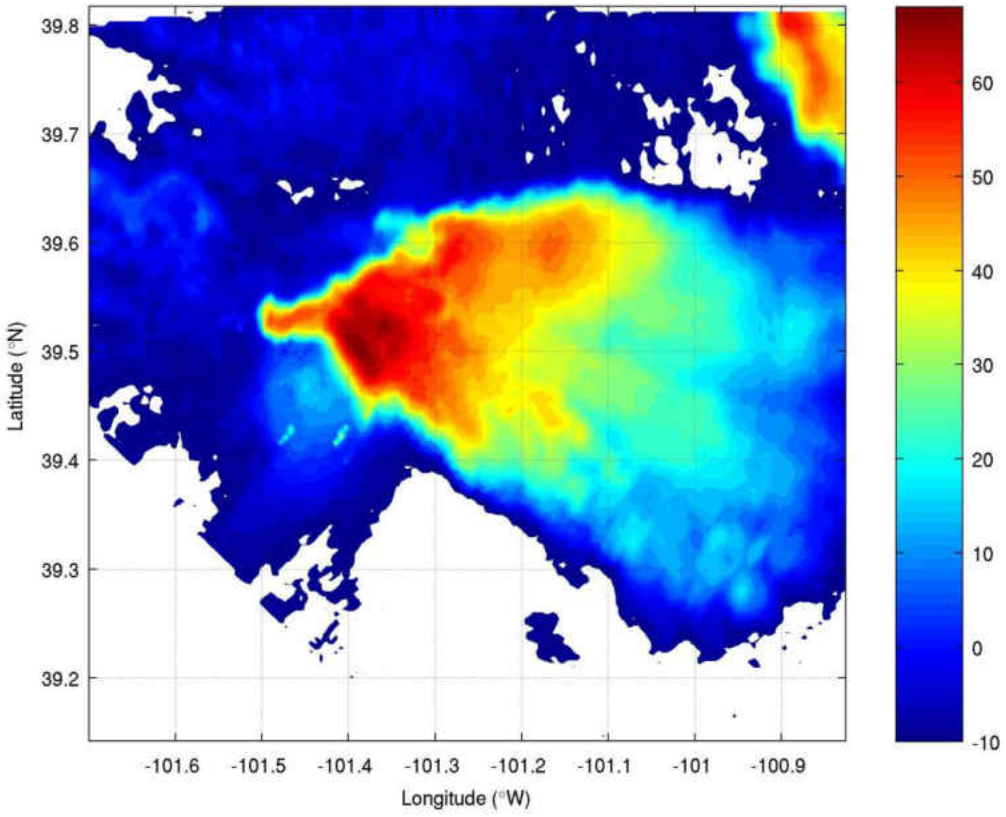

Figure 32: Radar reflectivity at 2 km for the June 29 super cell case at 2357 UTC.

4.1.7 July 2 Supercell

On 2 July 1998 the data were collected from a supercell thunderstorm utilizing the CSU-CHILL and CSU-Pawnee radars. At 0038 UTC, the first analysis time, the storm is already a well-developed supercell with a hook echo (Fig. 33). It moves to the southeast and maintains its strength until 0125 UTC, when it approaches some other cells and begins to lose organization.

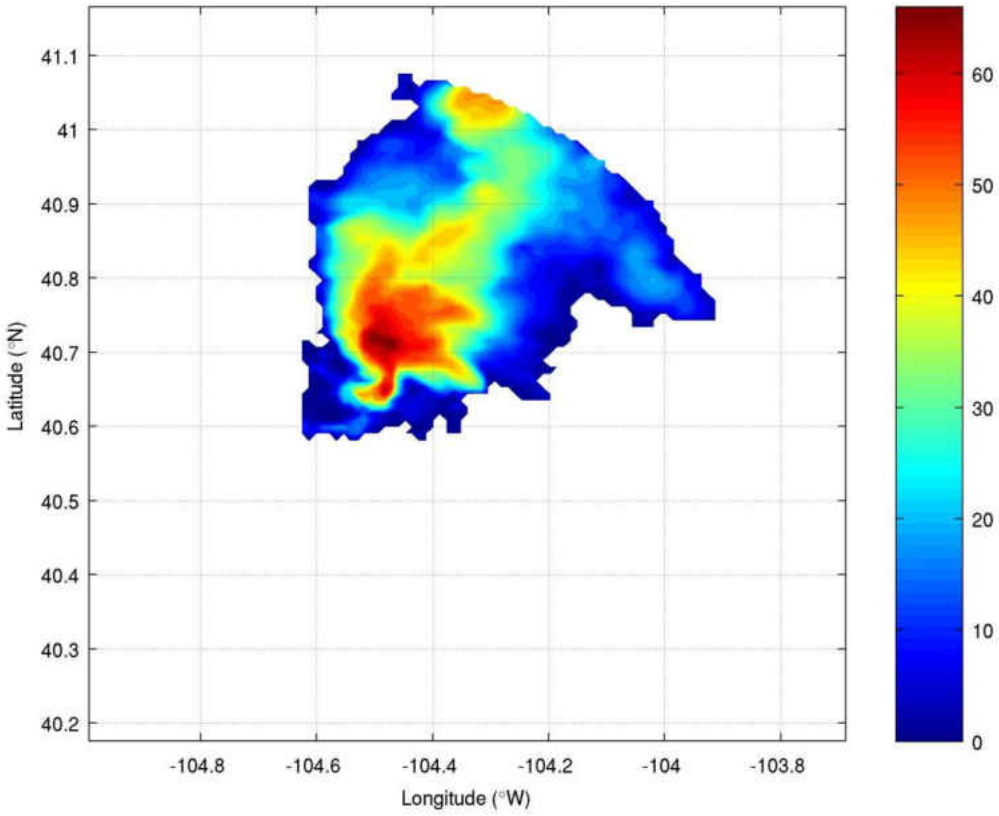

Figure 33: Radar reflectivity at 2km for the July 2 super cell case at 0038 UTC.

The cells then merge at 0135 UTC, and the storm, while not as impressive as earlier, still maintains the classic "kidney bean" supercell radar morphology. Unlike the STEPS supercell discussed in the previous subsection (4.1.6), the DDA and Steiner methods did not pass the threshold for anvil locations for many of the analysis times. When the DDA and Steiner methods did pass the threshold, their LMDs were 2 km or more lower than the divergence LMD (Fig. 34b). In contrast, the CSA method passed the threshold for anvil locations for all times and, although it performed poorly at some times (e.g., Fig. 34b), for most of the times the CSA had an LMD within 1-1.5 km of the divergence LMD (e.g., Fig. 35b).

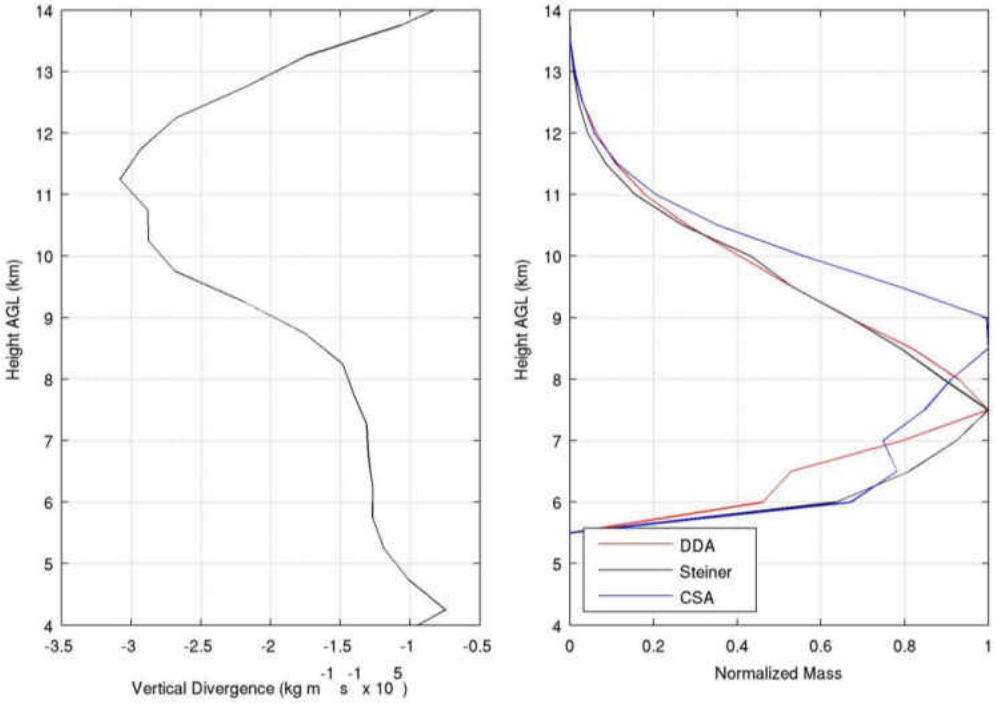

Figure 34: Mass detrainment profiles for the 1998 July 2 supercell at 0044 UTC, estimated using horizontally-integrated vertical mass divergence (a) and horizontally-integrated anvil mass (b). b) shows three different methods of anvil estimation: DDA (red line), Steiner (black line) and CSA (blue line).

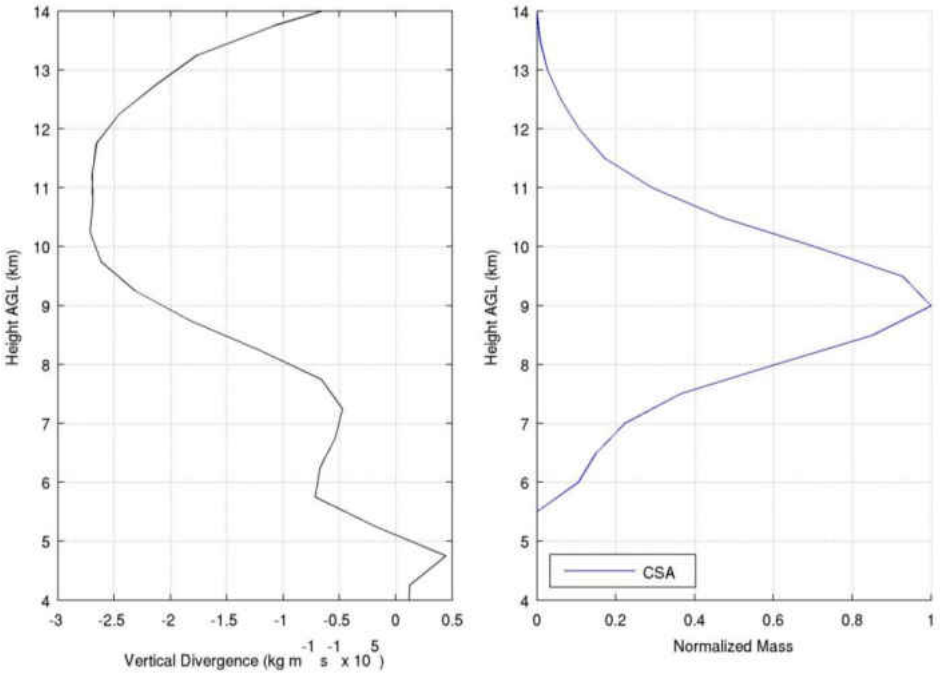

Figure 35: Mass detrainment profiles for the 1998 July 2 supercell at 0145 UTC, estimated using horizontally-integrated vertical mass divergence (a) and horizontally-integrated anvil mass (b). b) shows the only method of anvil estimation that passed the threshold, CSA (blue line.

In this case the detrainment LMD, while still in the anvil, sometimes occurred in the upper anvil and not at the level of maximum anvil reflectivity. This will be explored in section 4.2. The average distance from the vertical-mass-divergence-based LMD was smallest for the CSA method (Table 2).

4.1.8 July 15 Convective Line

On 15 July 1998 the data were collected from a convective line utilizing the CSU-CHILL and CSU-Pawnee radars. At 2328 UTC a convective line with very little stratiform rain enters the analysis region and tracks southeast through the end of the analysis at 0046 UTC. Figure 36 shows a constant altitude plot of this convective line at 2 km at 0040 UTC.

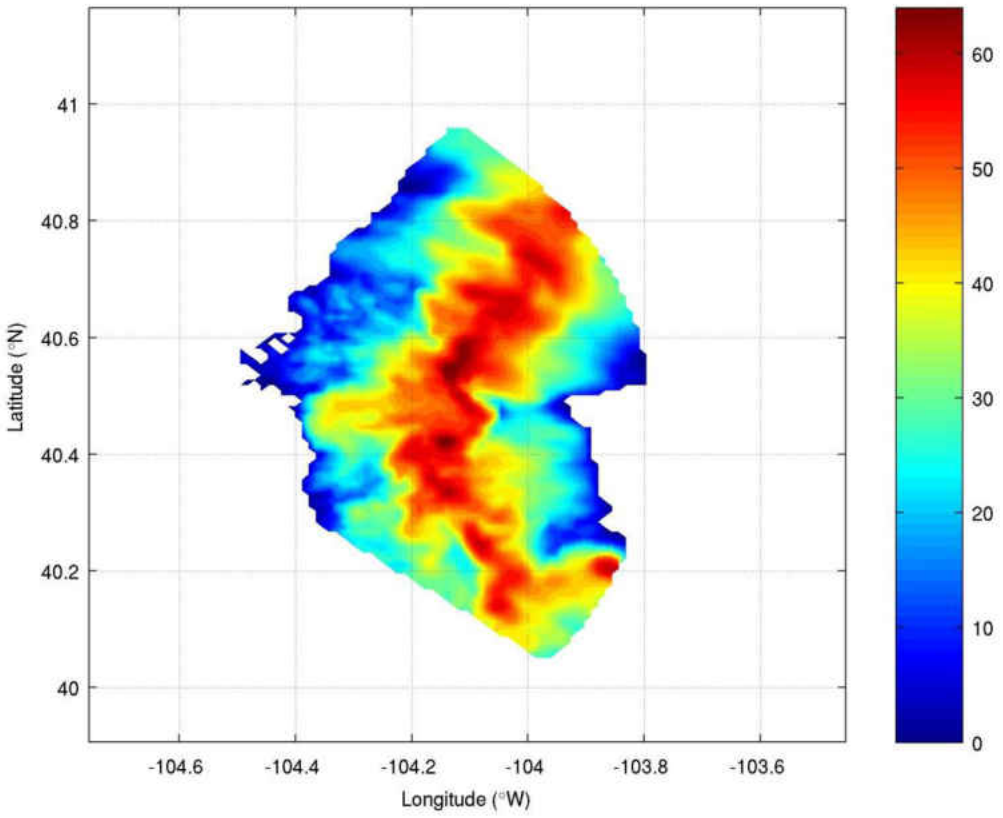

Figure 36: Radar reflectivity at 2km for the July 15 convective line at 0040 UTC.

At this time, the convective line has merged with some other cells, leading to the unusual shape of the storm. Figure 37 is from just before the cells merged at 0028 UTC.

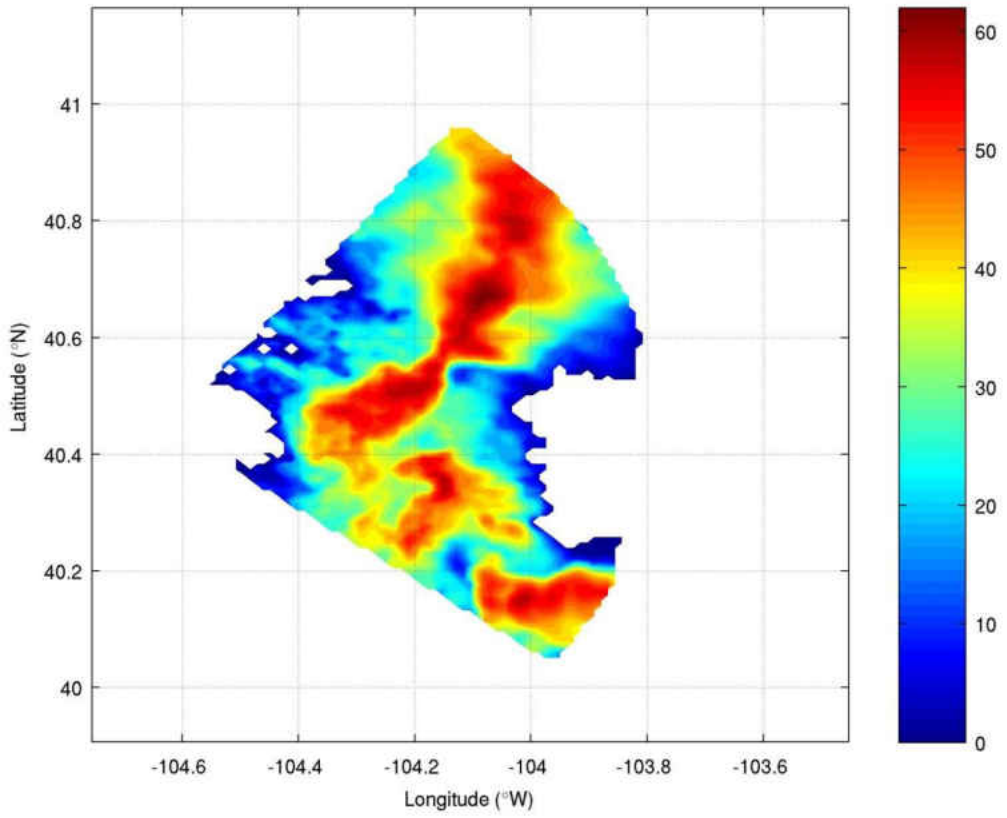

Figure 37: Radar reflectivity at 2km for the July 15 convective line at 0028 UTC.

For all the methods and at most times for this case, the mass-derived LMD is a maximum near ~6 km, as illustrated in Fig. 38b. This significant under-prediction of the LMD height is due to a widespread anvil mass at 6 km in this domain. This type of error is investigated further in the following section (4.2). Although under-prediction was a persistent problem, for the two earliest times, the CSA method had LMDs 1.0 to 1.5 km higher than at later times. For example, at 2328 UTC (Fig. 39) the CSA LMD is only approximately 1 km lower than the divergence-based LMD. The average distance from the vertical-mass-divergence-

based LMD was lowest for the CSA method (Table 2).

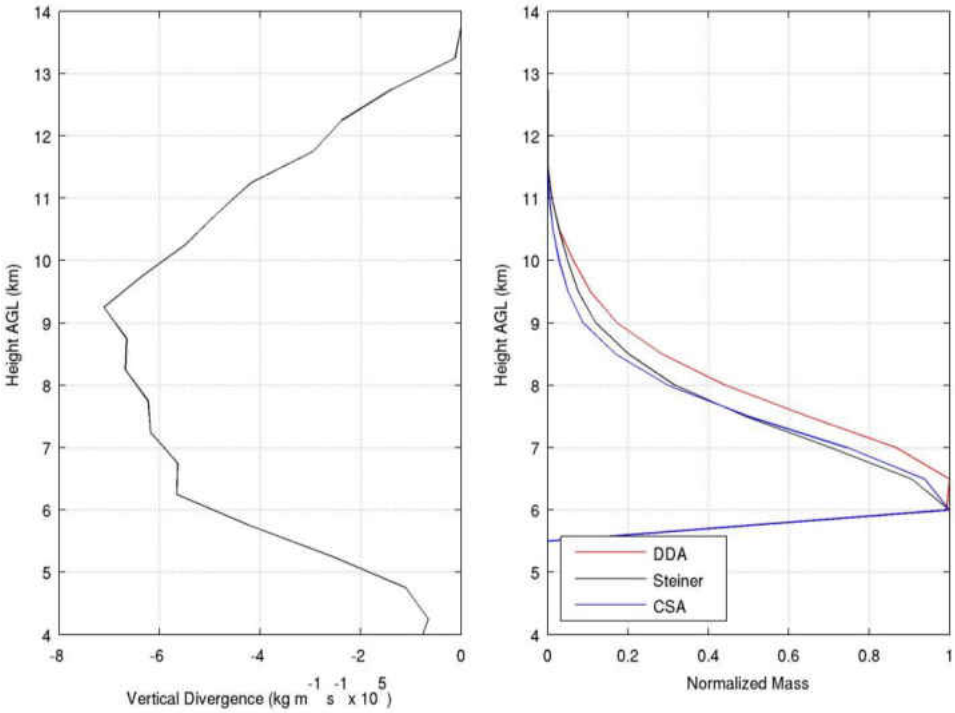

Figure 38: Mass detrainment profiles for the 1998 July 15 convective line at 2352 UTC, estimated using horizontally-integrated vertical mass divergence (a) and horizontally-integrated anvil mass (b). b) shows three different methods of anvil estimation: DDA (red line), Steiner (black line) and CSA (blue line).

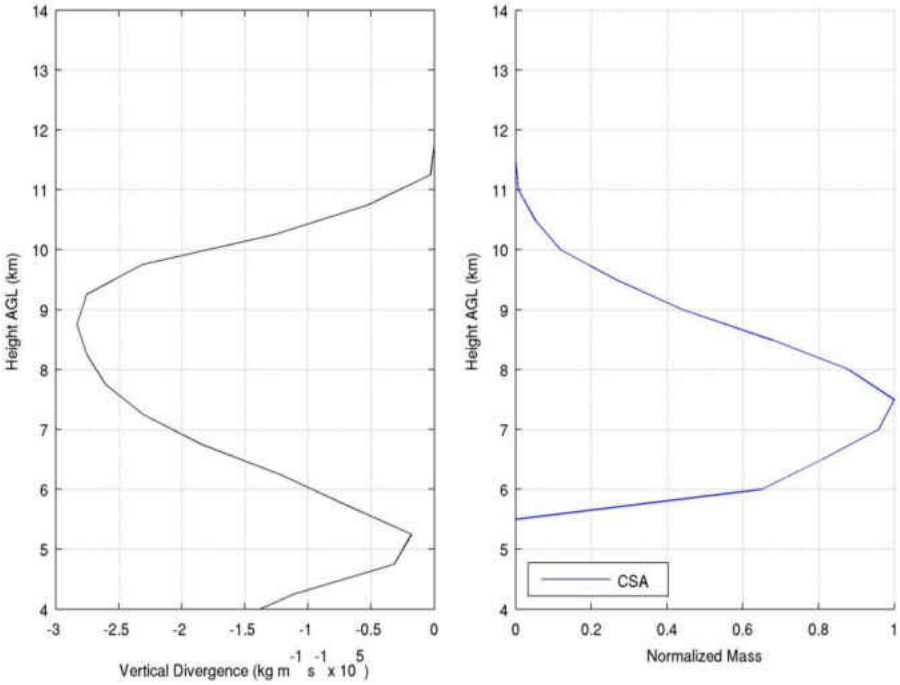

Figure 39: ass detrainment profiles for the 1998 July 15 convective line at 2328 UTC, estimated using horizontally-integrated vertical mass divergence (a) and horizontally-integrated anvil mass (b). b) shows the only method of anvil estimation that passed the threshold, CSA (blue line)

4.1.9 July 21 Multicell

On 21 July 1998 the data were collected from a multicell thunderstorm utilizing the CSU-CHILL and CSU-Pawnee radars. For this case, a slow moving cluster of cells propagated eastward by generating new cells as the old cells died.

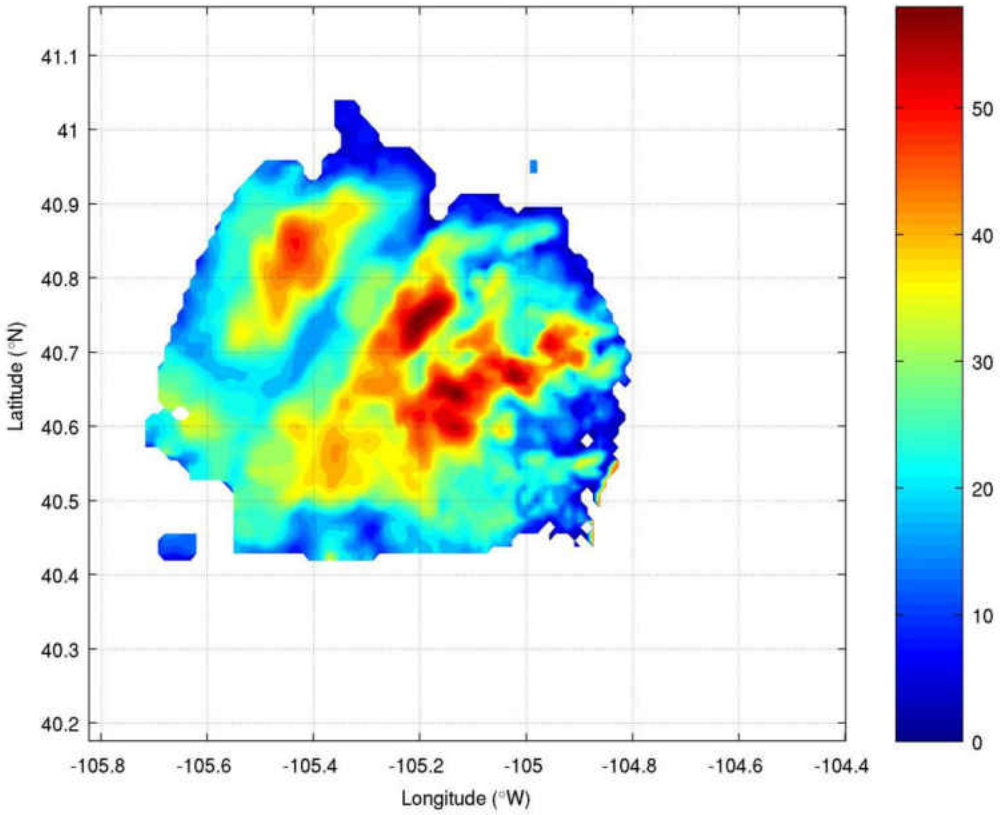

Figure 40: Radar reflectivity at 2km for the July 21 multicell case at 2106 UTC.

Figure 40 shows the radar reflectivity at 2 km for this multicell case. Initially, the most intense cell was south of the other cells, but, by 2056 UTC, the southern cell was dissipating. Around 2106 UTC (Fig. 40), the easternmost cell began to grow and became the dominant cell. The anvil altitudes in this case do not match up well with the divergence LMD for most times and methods. Figure 41 illustrates this gap between the mass-derived and divergence-derived LMDs. However, at certain times, the CSA method did show some

promise. At 2052 UTC (Fig. 42) the maximum is at 6 km, but there is another maximum at 10 km, close to the divergence LMD. This widespread anvil at 6 km is similar to that observed with the July 15 convective line case--this phenomenon is investigated further in the following section (4.2). The average distance from the vertical-mass-divergence-based LMD was the lowest for the CSA method (Table 2).

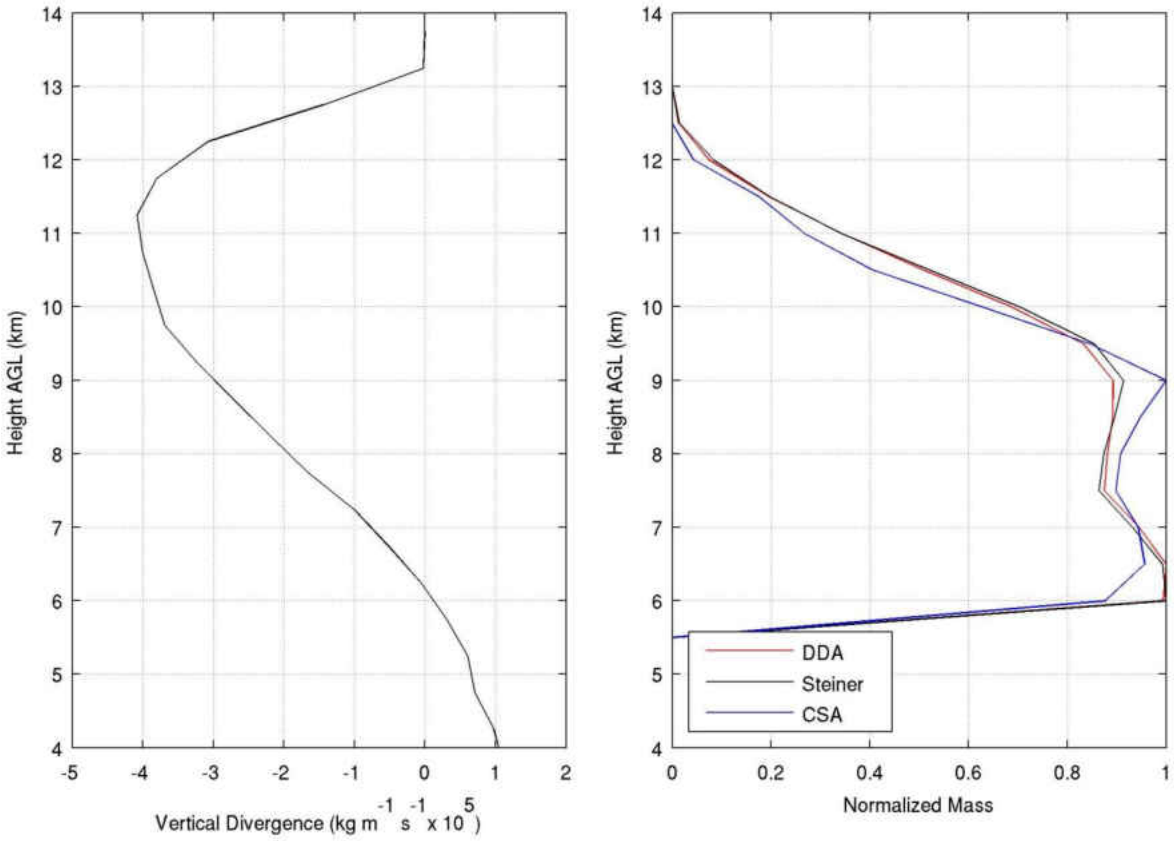

Figure 41: Mass detrainment profiles for the 1998 July 21 multicell at 2116 UTC, estimated using horizontally-integrated vertical mass divergence (a) and horizontally-integrated anvil mass (b). b) shows three different methods of anvil estimation: DDA (red line), Steiner (black line) and CSA (blue line).

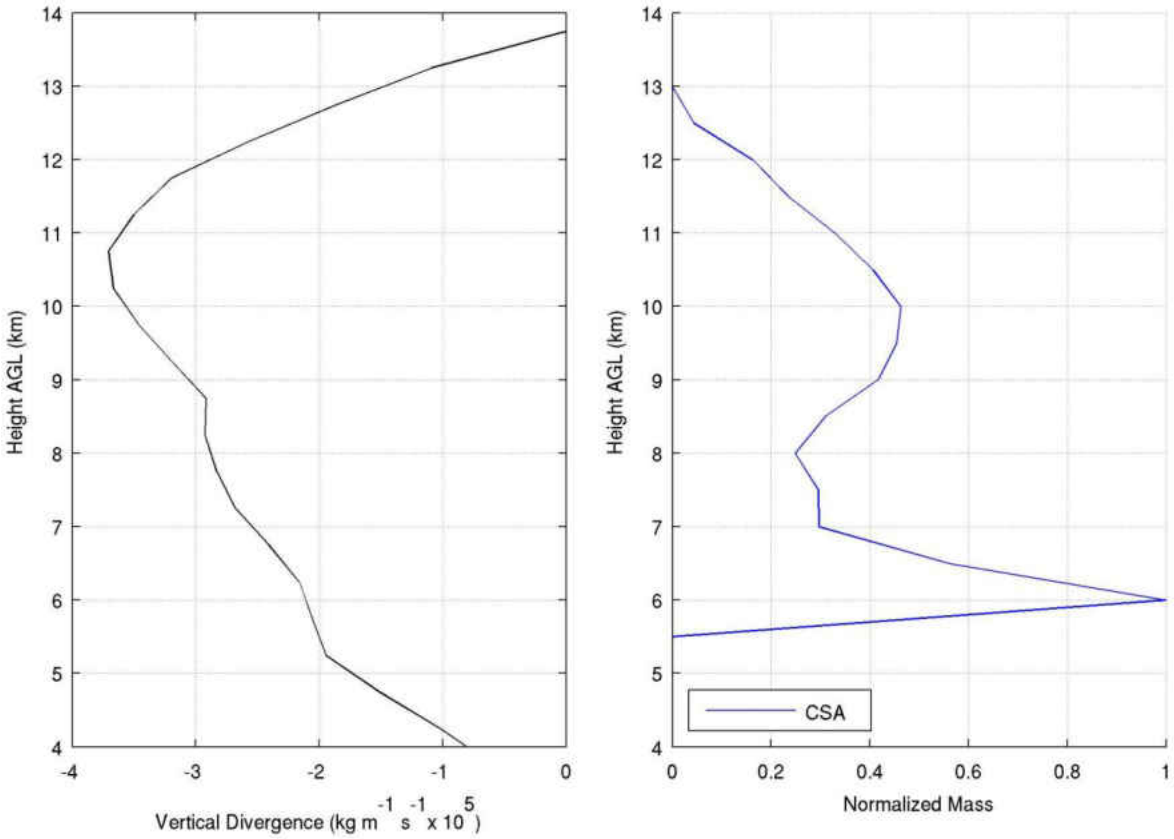

Figure 42: Mass detrainment profiles for the 1998 July 21 multicell at 2052 UTC, estimated using horizontally-integrated vertical mass divergence (a) and horizontally-integrated anvil mass (b). b) shows the only method of anvil estimation that passed the threshold, CSA (blue line)

4.1.10 Summary of Three-Method Comparison

For the majority of cases and times, the CSA method outperforms the other two methods. Table 2 shows that for eight of the nine cases, CSA provides the best results. Although the CSA method is the best method overall, it did not perform well at all times for every case. While CSA handles isolated cells (e.g. June 3 single cell) quite well, it struggles with clusters of cells (e.g. June 11 convective line). Also, with many of the cases where CSA performed well, there were times when it struggled. For example, the CSA method often performed better during later stages of storm lifecycles after they had already been mature for some time.

The DDA and Steiner methods often produced very similar results. Both methods used the same type of anvil detection, but used different approaches for identifying convective cores. As discussed in Chapter 3, the Steiner method for finding convective cores (also used by the CSA method) often incorrectly locates updrafts. However, for the purposes of this study, dual-Doppler based updraft locations did not produce a significantly better result than a reflectivity-based identification method. The results for the DDA and Steiner methods were often very similar while the CSA was different. Both the DDA and Steiner methods, although their convective identification differed greatly, used the same simple anvil definition. The main factor for the success of the three methods was how well the anvil identification methodology worked. It was not the methodology for identifying convective location. The simple anvil approach did not work as well as the CSA multi-layer technique.

4.2 Investigation of the CSA Method

The previous section proved that the CSA method was the most successful method among the three tested, including the method that most closely mirrors previously published methods (i.e., the Steiner method, which is similar to the methods used in Mullendore et al. 2009 and Takahashi and Luo 2012). With the ultimate goal being application to radar retrievals that do not include dual-Doppler three-dimensional velocity fields, the proper way to apply the CSA method needs to be investigated and developed. In order to develop application recommendations, the weaknesses of the CSA method will be discussed in this section. For the CSA method, are three main factors have a significant impact on its success: missing data in the vertical column, storm morphology, and the maturity of the convective cells.

4.2.1 Missing Data in the Vertical Column

One of the biggest factors that caused the CSA method to fail is when the threshold value for analysis anvil locations is not met. When this threshold is not met, no result is produced. This happens for two main reasons: a lack of anvil classifications within 10 km of the convective cores or missing data in the vertical column at anvil locations. This section discusses the impacts of missing data in the vertical column.

As stated in the section 3.5.2, locations with sharp gradients at the top or bottom of an anvil near missing data values were removed. This was done since sharp gradients along the bottom lead to incorrect CSA classifications and sharp gradients near the top lead to unusually low LMDs. As shown in section 3.5.2, the June 22 case had significant missing data at low levels, leading to misclassification of anvil. The July 15 case had significant missing data at upper levels, leading to miscalculations of anvil height. Additional pre-processing of the gridded radar reflectivity data, as discussed in section 3.5, now mitigates both of these by removing these vertical columns from the analysis. However, the removal of columns leads to fewer candidate anvil locations, ultimately leading to insufficient anvil to calculate a mass-based LMD. This lack of anvil due to missing data was particularly evident in the July 15 and 21 cases. As shown in Table 2 only 36% of the times for each of these two cases passed the anvil threshold. While some issues with morphology, discussed in next section, were present, missing data was the main reason for the low percentages for both of these cases. Another example of missing data is the June 19 storm. For this convective line, only 29% of the times passed the anvil threshold due to missing data in the vertical column. As shown in Fig. 25, data are missing at both the top and the bottom of the reflectivity profile, which results in much of the data being removed in preprocessing.

In summary, to avoid misclassifying anvils, extensive preprocessing needs to be done before applying the CSA method. This preprocessing, however, can lead to a lack of columns identified as anvil, such that the method does not meet the anvil count threshold for a given time. This problem is not easily corrected as there are multiple reasons that data at specific grid points can be removed such as ground clutter or poor data quality. Since data are never perfect pre-processing is an important step in all of the methods.

4.2.2 Morphology

Storm morphology had a significant impact on the success of the CSA methodology. Better results were produced with cases like the June 3 single cell p much better than cases like June 11, which had multiple cells. However, enhanced performance is not just because of storm type, as the CSA method also performed well for the June 23 multicell. The general storm classifications shown in Table 2 are from Mullendore et al. (2013). Additional morphology classifications beyond those shown in Table 2 can be used, as in Gallus et al. (2008), which are shown in Fig. 43. This radar reflectivity structure based method provided another means of classification. Of these morphologies, the times with clusters of cells (CC) or non-linear (NL) produced poor results with the CSA method. When convective cores are close together, the CSA classification algorithm has a hard time finding anvil locations. This is because where one cell's anvil is located another cell could be contributing some lower level clouds, which would result in a non-anvil classification.

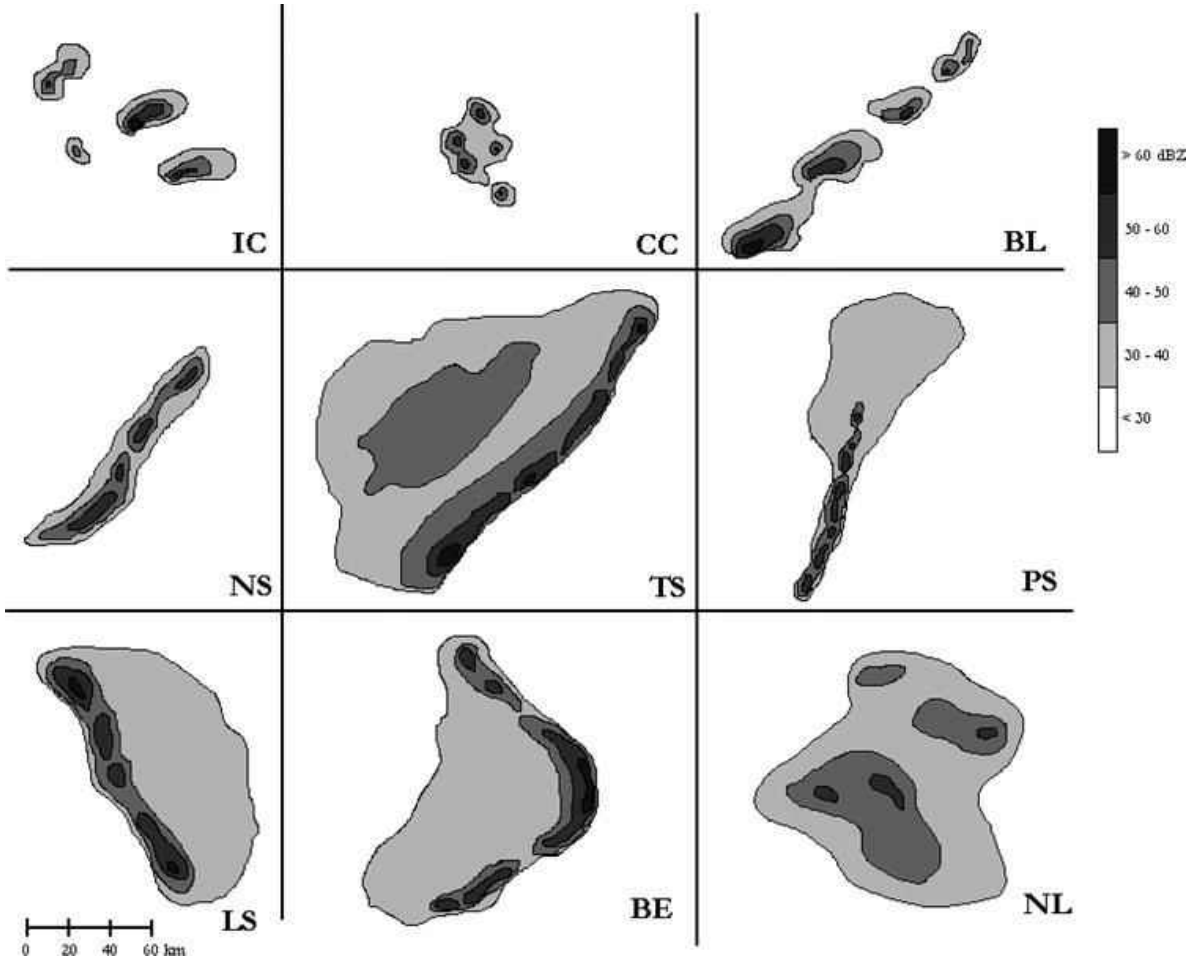

Figure 43: Taken from Gallus et al. (2008) figure 2. This details the 9 morphology classifications: isolated cells (IC), clusters of cells (CC), broken line (BL), squall line with no stratiform rain (NS); squall line with trailing stratiform rain (TS), squall line with parallel stratiform rain (PS); squall line with leading stratiform rain (LS); bow echo (BE), and nonlinear system (NL).

An example of how multiple cells close together can have a major impact is provided by the June 11 STEPS at 2213 UTC. Figure 19 gives an overview of the reflectivity at this time, at which many high reflectivity cells were present. Figure 44 shows that there are not many anvil locations (red), and the few anvils locations that are present are not close enough

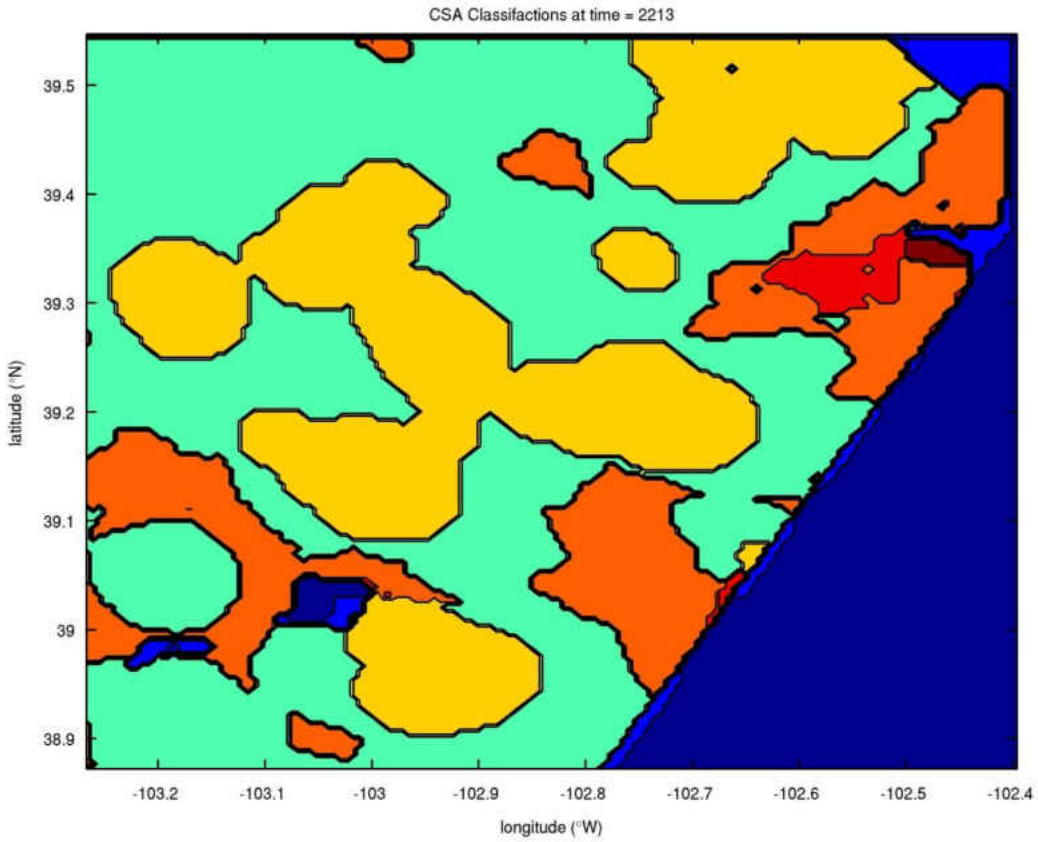

Figure 44: The CSA classifications for the June 11 STEPS convective line at 2213 UTC. The convective cores are yellow, stratiform regions green, transitional regions orange, mixed anvil light red, ice anvil dark red, and blue regions low clouds or no data.

to the convective cores (yellow) to be considered convective anvil. Another example is at 0025 UTC, at which time very few anvil locations were identified with the CSA method (Fig. 45). Stratiform (green) and the transitional or deep cloud region (orange) dominate the area surrounding the convection (yellow). At this time, CSA did not identify any anvil because

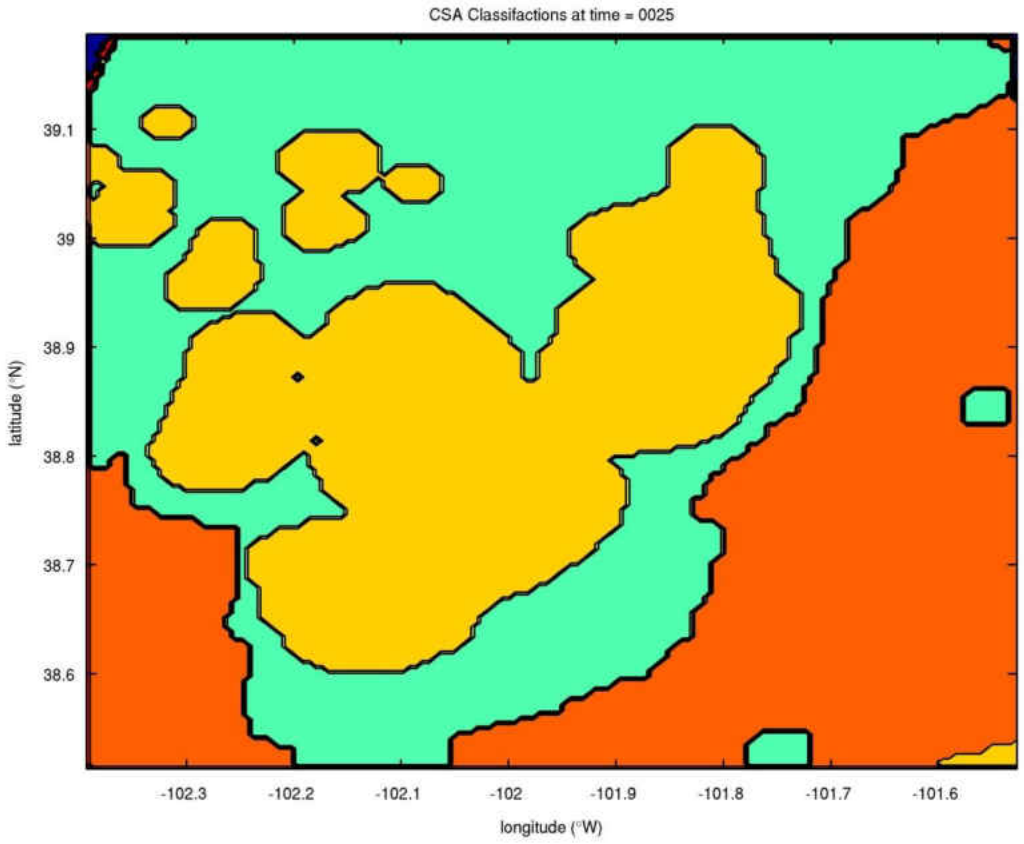

Figure 45: The CSA classifications for the June 11 STEPS convective line at 0025 UTC. The convective cores are yellow, stratiform regions green, transitional regions orange, mixed anvil light red, ice anvil dark red, and blue regions low clouds or no data.

there were too many low level reflectivity returns as shown in Fig. 46b. As stated in the methodology, the CSA method uses three levels to determine classifications, and if returns are present in the lowest level, anvils are never classified. It is because of this that cases with multiple cells close together may have few anvil locations.

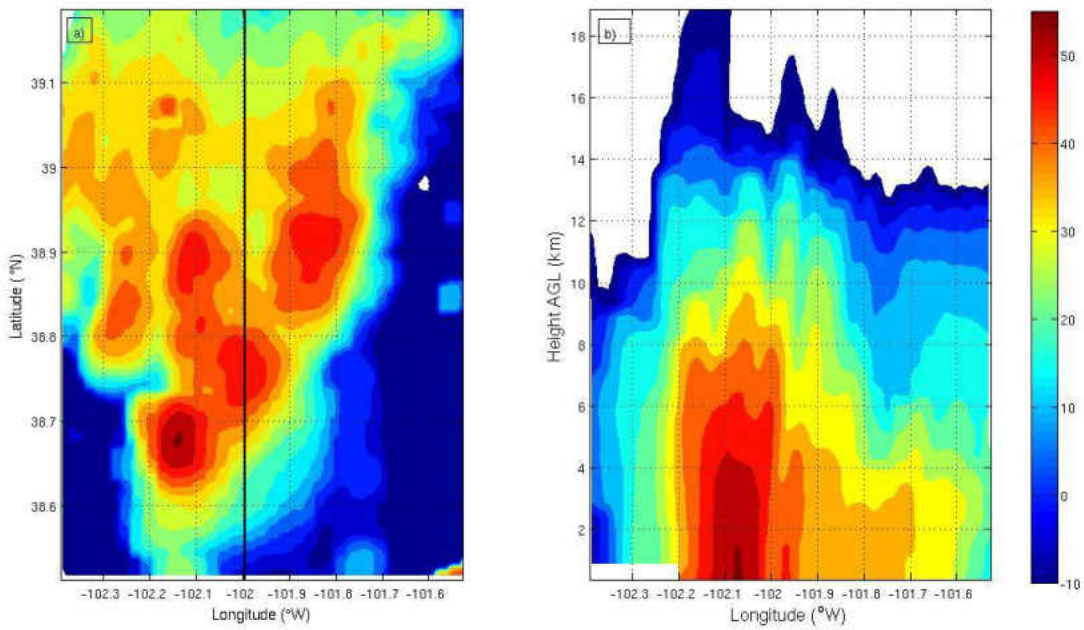

Figure 46: a)Horizontal reflectivity cross section at 2 km. b) Vertical reflectivity cross section taken at black line on a).

However, not all multicells present this problem. As shown in Fig. 47, the June 23 STEPS multicell case shows that the methodology works with some multicell storms. This storm, based upon the Gallus et al. (2008) classification system, is a broken line (BL). Since this is a BL and not a CC or NL, the CSA method can classify anvil regions that are within the analysis region as shown in Fig. 47. With a CC morphology many features from the different cells can overlap, which complicates the classification and can often lead to non-anvil classifications. With a BL morphology there may still be some overlapping features and therefore missed anvil, but there is much less of this. This is shown in Fig. 47, as while there are no anvil regions in the areas between the convective cores (orange), there are numerous anvil regions (green) behind and in front of the convective cores. The nonlinear morphology would also lead to a failure of the CSA method for the same reason. Only the linear and isolated morphologies (IC, BL, NS, TS, PS, LS, and BE) will work with the CSA method,

while the nonlinear (CC and NL) will struggle.

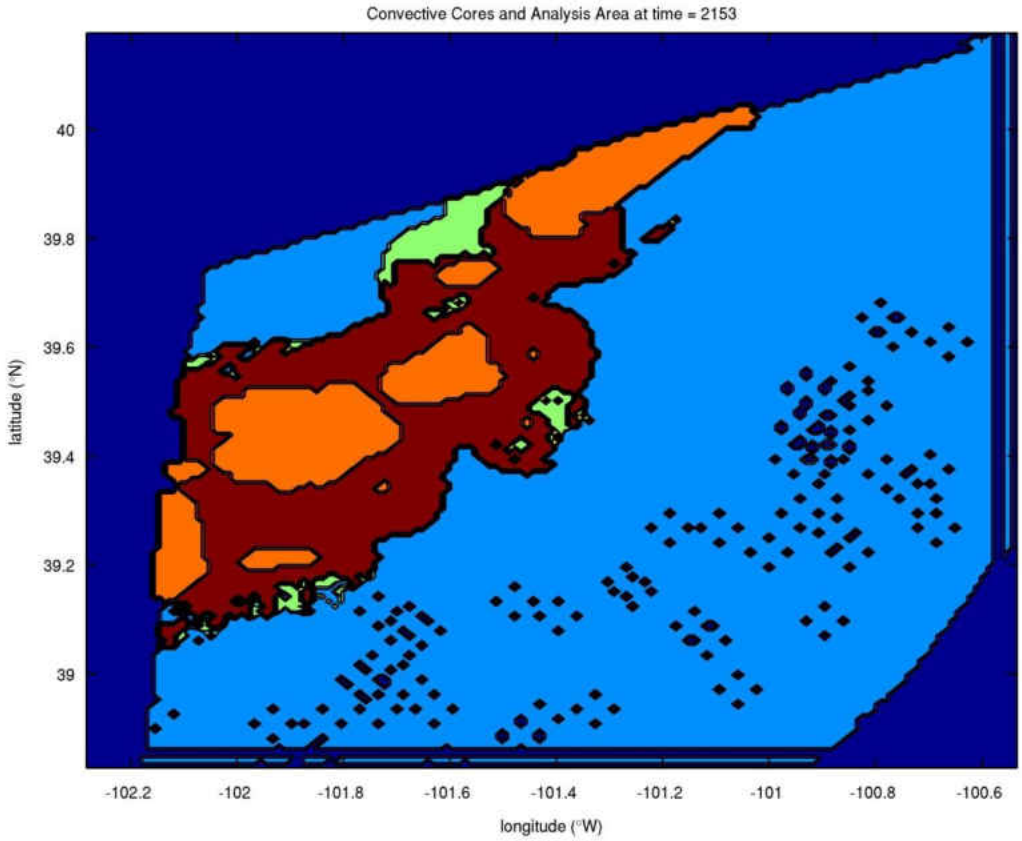

Figure 47: plot of the locations of the convective cores, analysis region, and analysis anvil locations for the June 23 STEPS multicell at 2153 UTC. The convective cores are orange, analysis region locations without anvil red, and analysis anvil locations green. blue colors are no data regions.

4.2.3 Maturity of Convective Cells

The maturity of the cells being analyzed is another significant factor in the accuracy of this method. Since the CSA method infers detrainment based upon anvil reflectivity, it is dependent upon the formation and location of the anvil. Therefore, this method should only be used with cells having mature updrafts. In cells with developing or dissipating updrafts, the level at which maximum detrainment occurs changes more rapidly than in cells with mature updrafts. Additionally, while a measurement of detrainment from vertical mass divergence can be made instantaneously, an anvil needs time to grow before anvil mass can

be estimated. The CSA methodology works best for an anvil that has had time to develop from into a mature and relatively consistent updraft. A mature and consistent updraft would be an updraft that has little to no change in height with time.

The June 3 single cell provides a good case for investigating the impacts of maturity, as it is an isolated cell and was analyzed at different stages of its development. Figure 17 shows both the LMD and the detrainment envelope of the CSA method (black lines) and also the vertical mass divergence LMD and detrainment envelope (blue lines) at every radar scan time. Based on Fig. 17, the CSA method performs well (i.e., compares well with the mass divergence calculations) at all of the times, However, it performs best around 2356 UTC, which is late in the mature stage of the storm before dissipation begins (Tessendorf et al. 2007). Figure 48 provides a comparison of the CSA mass and vertical divergence at 2304 UTC (early in the mature stage of this storm) and 2356 UTC (late in the mature stage of this storm). The early mature time has much less mass in the anvil than the late mature time since the later time had more time for the anvil to grow. The earlier time also has a greater difference between the CSA and vertical-mass-divergence LMDs. This shows that the anvil needs time to grow after the storm reaches maturity before the CSA method can be used to accurately determine the LMD. Since this is a single cell, there is much higher confidence in the mass amounts shown by CSA. As discussed in the previous section, without other cells nearby, CSA more consistently identifies anvil locations associated with deep convection. In other cases, such as the June 22 convective line, all of the analyzes were at times when the

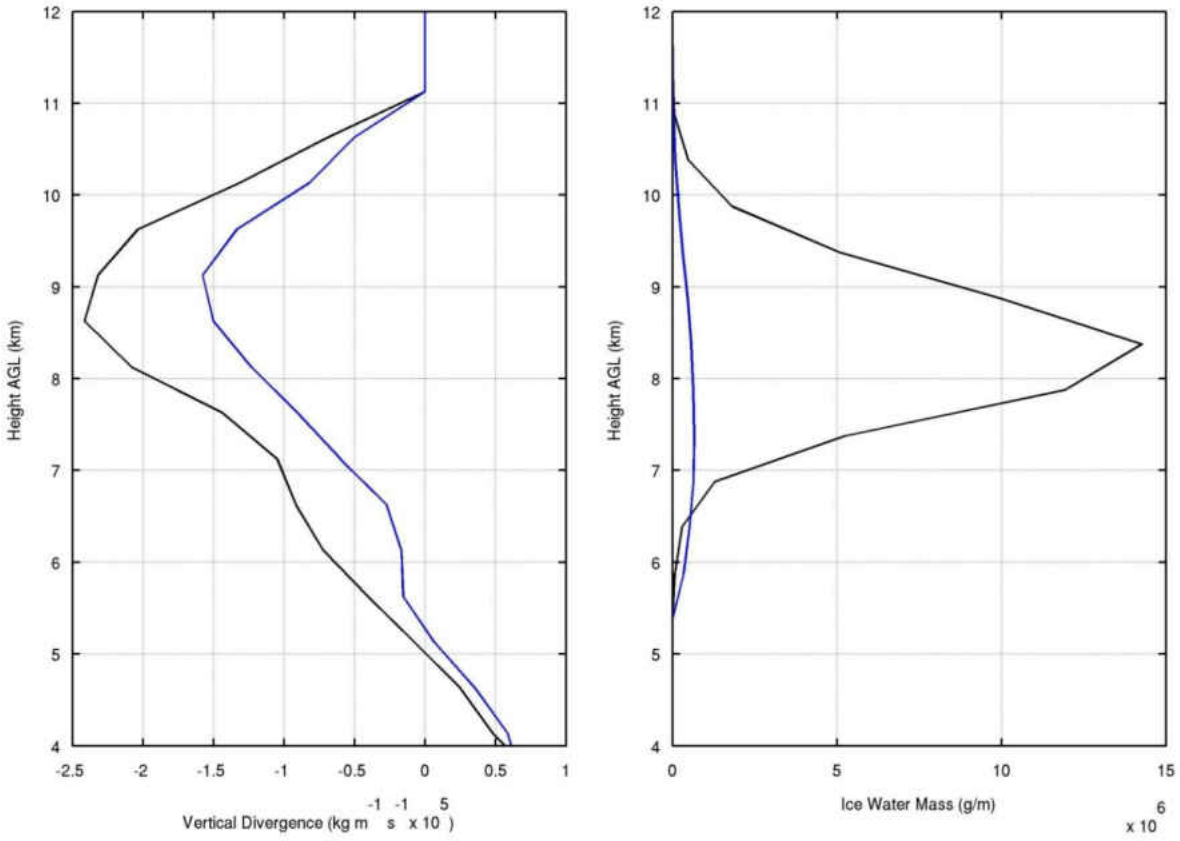

Figure 48: Vertical mass divergence plotted on the a and CSA ice mass on the right for two times from the June 3 STEPS single cell case. blue lines are for 2304 UTC and black lines are for 2356 UTC.

storm was mature (Tessendorf and Rutledge 2007). Figure 49 shows the evolution of the LMD for June 22 storm. It shows that at the times with enough anvil locations, the CSA methodology performs quite well. Note that for this case, missing data at low levels led to many of the anvil locations being removed at the times that are not plotted.

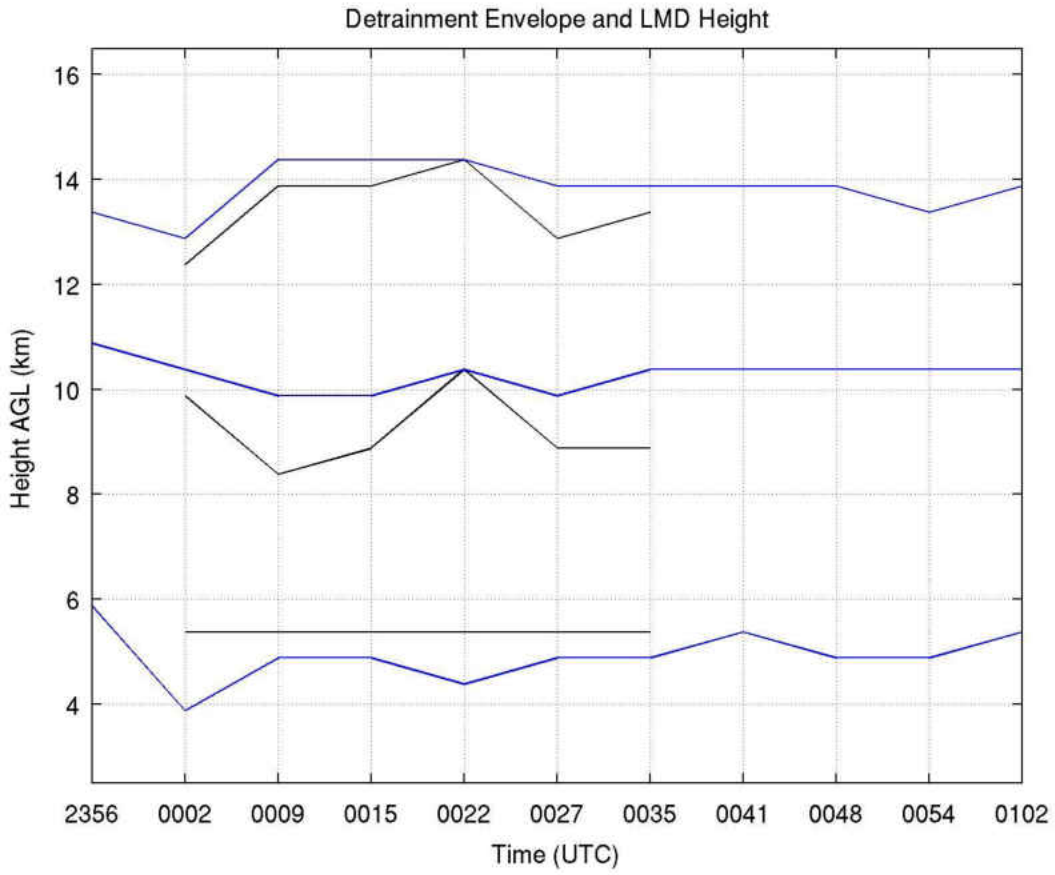

Figure 49: A plot of the upper envelope (top two lines), LMD (middle two lines), and lower envelope (lower two lines) height for the June 22 STEPS convective line case. Blue lines are for the vertical mass divergence and black lines are for the CSA ice mass.

Cells at different stages of development will detrain at different levels, which presents a challenge to a methodology that analyzes a large area. This can create situations in which two LMD maximums are present due to two cells detraining at different heights. In such situations, choosing one LMD height can be challenging. An example of how two cells close together can have a major impact is the June 29 STEPS supercell at 0010 UTC. Figure 50 shows that at this time a cell is located to the northwest of the supercell. This cell is significant enough to be counted as a convective core and, thus, anvil near it is analyzed.

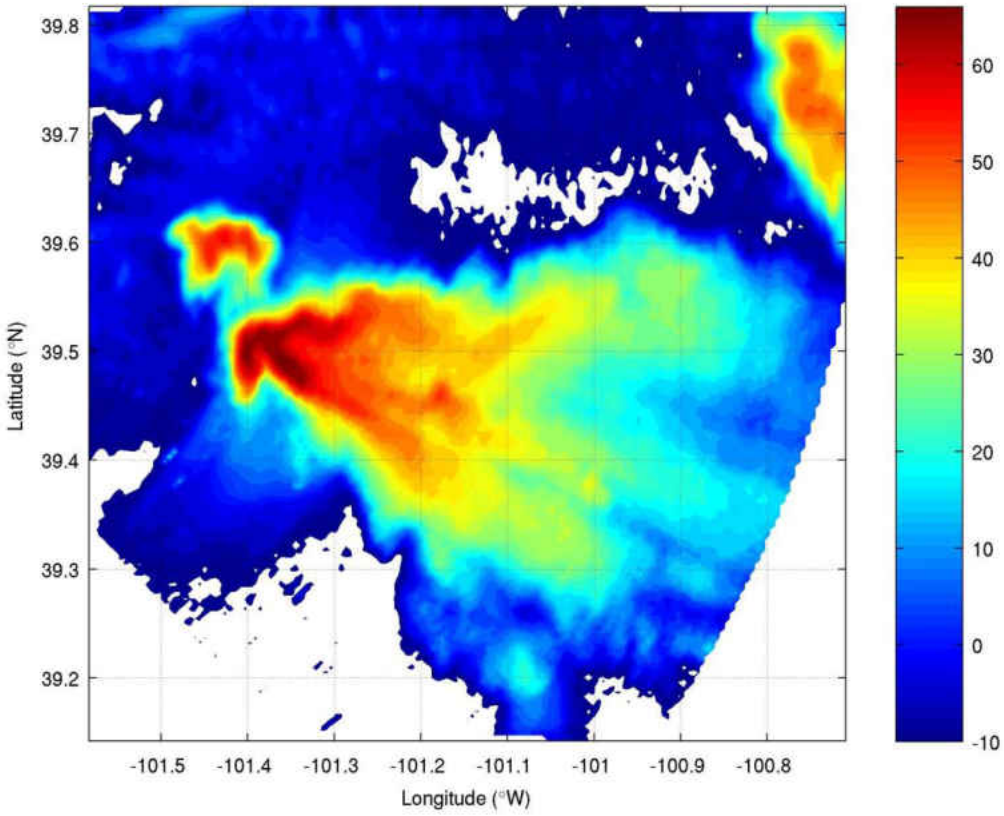

Figure 50: A horizontal radar reflectivity slice of the June 29 STEPS super cell at 0010 UTC at 2 km.

Figure 51 shows the anvil mass that is estimated when considering both convective cores and when considering only the dominant convective core (black line). When both cores are used considered, a double maximum is present in the CSA result. If only the main convective core is considered, then the plot changes significantly and only a single maximum is present. Figure 51 shows that the two methods produced well-matched LMDs. Based on this, it seems that the smaller developing cell was b detraining mass near 9 km at this time, while the larger cell was detraining at 13 km. Unusually, the mass maximum for what seems to be from the

developing cell is larger than that from the larger primary supercell. This

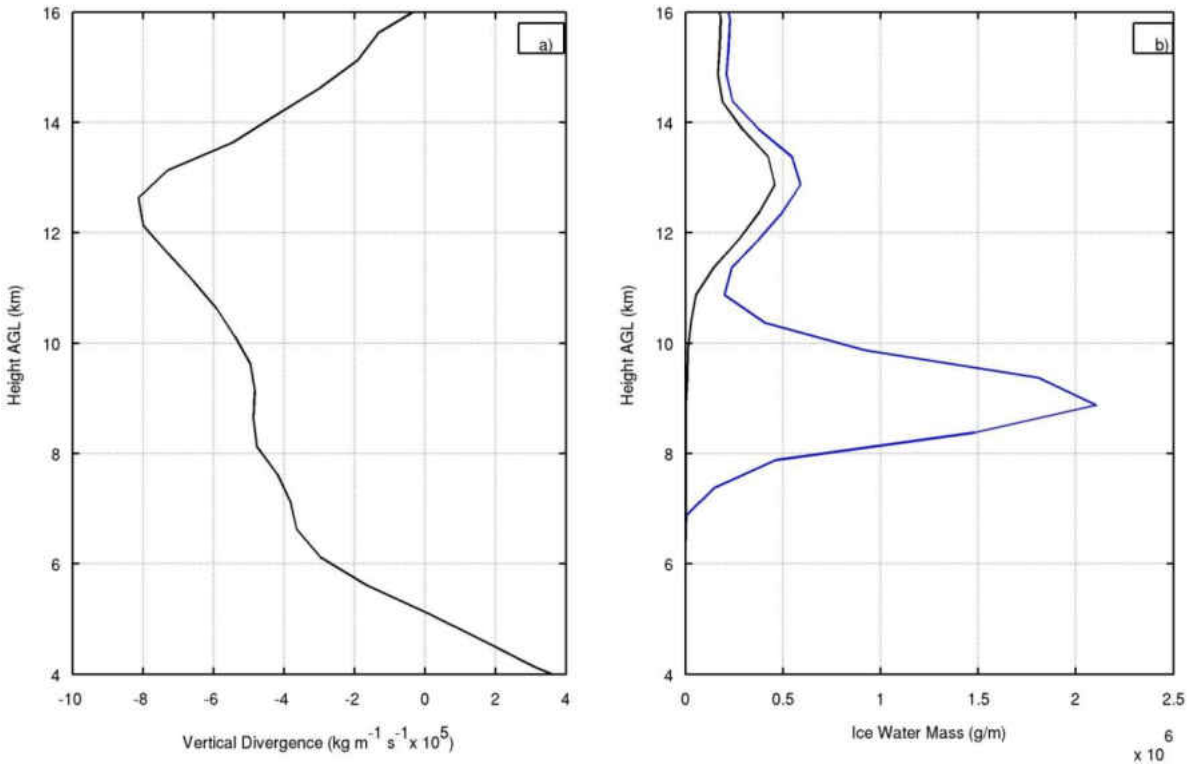

Figure 51: : a) Vertical mass divergence plotted. b) CSA ice mass on the right for 0010 UTC from the June 29 STEPS super cell case. Only the larger convective core was used for the CSA ice mass for the black line while the whole domain was used for the blue line.

result of the lower anvil dominating the signal over the higher anvil from the primary updraft is due to the location of the CSA anvil classifications. Figure 52 shows that much of the anvil (dark red) associated with the larger convective core is more than 10 km away from the core, while there are more anvil locations near the smaller developing core.

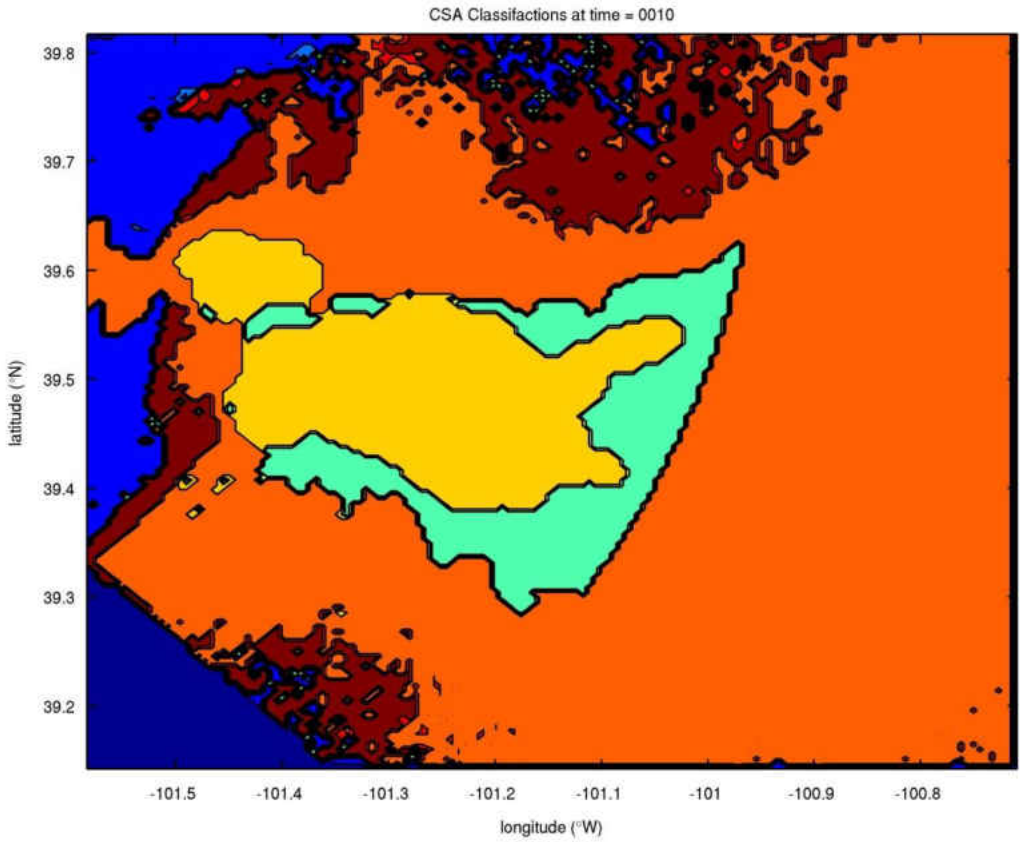

Figure 52: The CSA classifications for the June 29 STEPS supercell at 0010 UTC. The convective cores are yellow, stratiform regions green, transitional regions orange, mixed anvil light red, ice anvil dark red, and blue regions low clouds or no data.

4.2.4 Application of CSA Method Recommendations to Previous Results

Based on analysis of the CSA method results a more representative picture of how the three methods performed was made. Analysis of the CSA method results provided suggestions based on storm maturity and morphology that were not used in the previous STEPS and CSU results. A new method was determined to make use of the recommendations related to storm maturity. Instead of utilizing average mass values, a most representative time was determined. This was done because the late mature times lead to the best results with all three methods. Based on the analysis presented in section 4.2.3, the time when the anvil would be most representative of mass transport is late in the storm's mature

phase. Times were selected for all nine cases based upon the detrainment magnitude. The time before the detrainment magnitude began to have sustained decreases is the most representative time. The result of the new analysis is table 3, which lists the difference between the average vertical mass divergence LMD and the mass based LMD at the most representative time.

Date	Morphology	Rep Time (UTC)	Div-DDA (km)	Div-Steiner (km)	Div-CSA (km)
June 3	IC	2356	0.5	0.5	0
June 11	TS	0025	-	0.2	-0.3
June 19	NL	0148	-	-	-
June 22	TS	0054	5.0	2.5	4
June 23	BL	2232	-	-	0.5
June 29	IC	0010	3.0	3.5	-1.0
July 2	IC	0135	-	-	1.5
July 12	NS, CC	0028	3.0	2.5	2.5
July 21	CC	2126	4.5	4.5	4.5

Table 3: The difference in height between the vertical mass divergence based LMD and the method based LMDs for all nine cases based on the LMD at the rep time. Morphologies that work well in the CSA method are in green and morphologies that do not work well are in red.

For the June 29 case there were two cells present and, as suggested in section 4.2.3, only the primary cell's convective cores were used, while the developing cell's convective cores were ignored. Also listed in table 3 are the morphologies present for each case at its most representative time. With the exception of the June 22 case all of the cases with poor results are cases with CC or NL morphologies present. For the June 22 case at 0054 UTC, the most representative time, there was significant missing data near the surface which lead too much

of the data being removed via pre-processing. For the cases with ideal (green) morphologies, the CSA method did as well as or better than the other two methods. However, the amount that CSA method outperforms the other methods using the most representative time (table 3) is not as large as when all the times are considered (table 2). In other words, when the most representative time is known, all three methods are adequate proxies for convective transport, but if the most representative time is not exactly known, the CSA method is the best choice for determining the LMD.

4.2.5 Discussion of Application for CSA Method

While the CSA method provides more consistent results and represents an improvement compared to previous methods, it does not work for all cases. It works best when applied to isolated cells with mature updrafts. How well the anvil identification works is the biggest single factor. The clearer an anvil is, the easier it is to identify and the better the method works. The messier the anvil is, either due to missing data, proximity to other cells, or significantly varying detrainment altitude, the worse the method performs. The accuracy of the method will vary from case to case depending upon morphology and the ability to identify maturity.

If cells are close together, a cell-by-cell analysis method may be needed. If cells are isolated and mature, then the whole area can be analyzed. However, as the June 23 multicell case demonstrates, not all of the cells need to be isolated for the analysis method to perform well. The specific morphology of the storm plays a role in how the method performs. The CC and BL morphologies are a challenge while other, more linear, morphologies such as broken lines do not present this challenge. While morphology can explain a lack of results at certain

times, it should not lead to erroneous results. For application of the method, the morphology of storms should be considered.

Also, identifying whether a storm is mature is important. At this time, a subjective analysis of storm maturity is recommended, although it is possible that in the future a cell-tracking algorithm could be used to identify maturity. Finally, it is suggested that when more than 50% of near convective columns have been removed by pre-processing (over all analysis times), this approach should not be used for deriving mass-based LMD estimates. These recommendations will be tested in the next section using a case study of NEXRAD mosaic data.

The primary goal of this project was to develop a method that could provide an estimate of the level at which the maximum detrainment occurs using only radar reflectivity data. Such a method would be of great use with chemical models since this method could be used to constrain chemical transport. A climatology based upon this method could be developed for different storm types in different geographical regions, and could be used as a baseline for model comparison. For example, this method could be applied to more supercell storms in the STEPS domain of Kansas and Colorado. From this extended analysis, an average LMD profile could be determined. Based upon the cases considered herein (the June 29 and July 2 supercells), the LMD for late June/early July supercells is between 10 and 12 km. Then, if a chemical transport model was detraining mass at 6 or 8 km, the modeler would know that something could be wrong and that further analysis would be needed.

4.3 Application of the CSA Method to DC3 Field Experiment

The CSA method was applied to three cases from the Deep Convective Clouds and Chemistry (DC3) campaign. These cases were chosen because the DC3 campaign, once the data is released, will be able to provide verification sources. There were three regions study: northern Alabama, northeastern Colorado, and central Oklahoma/Western Texas. One case from each region was selected due to storms being present within the dual-Doppler lobes and flights in the anvil having occurred. These three cases are: May 21 from Alabama, May 29-30 from Oklahoma, and June 6-7 from Colorado. In this section an overview of the DC3 campaign will be given followed by analysis of the results from the three cases. The radar data analyzed for these three cases was from the NMQ NEXRAD mosaic dataset as discussed in section 3.2. The methodology used in these cases is identical to the methodology for the CSA method detailed in chapter 3 with a few changes. Specifically, the methods suggested in the previous section to mitigate sources of error were applied to these cases. All mass plots are taken from the freezing level, as determined based on nearby soundings, to the top of the anvil. The analysis areas were chosen based upon storm maturity, morphology, and proximity to the DC3 measurement platforms.

4.3.1 DC3 Overview

The DC3 project used aircraft and a variety of ground based facilities in three regions to gather observations to improve the understanding of the role of convective clouds in the composition and chemistry of the UTLS (Barth et al. 2012). The regions, detailed above, were selected to gather observations on different types of storms with different initial conditions at different times; as these parameters can vary significantly between these three regions (Barth et al. 2012). The various instrument platforms used in the study are shown in

figure 53. There were three instrumented aircraft that participated in this study: The NSF/NCAR Gulfstream-V (GV), NASA DC-8, and German Aerospace Center (DLR) Falcon. The GV studied "high altitude outflow of the storms, and is instrumented to measure a variety of gas-phase species, radiation, and cloud particle characteristics" (Barth et al. 2012). The GV also performed downwind sampling to document chemical evolution of the convective outflow. The DC-8 observed storm inflow and provided remote sensing to aid planning and observe outflow evolution. The Falcon measured "the very fresh storm outflow close to the storm core as well as measurements of aged outflow" (Barth et al. 2012). Multi-Doppler networks were set up within each study region to measure the physical and kinematic characteristics of the storms. Lightning mapping arrays were used to detect lightning as it is important in the formation of NOx. Lastly, radiosondes were used to determine the atmospheric profile with respect to temperature, moisture, and wind. Of interest to this study is the data from the chemical measurements taken from the aircraft and the multi-Doppler data to evaluate results. These data will be used to evaluate the results of the following sections as the data are released.

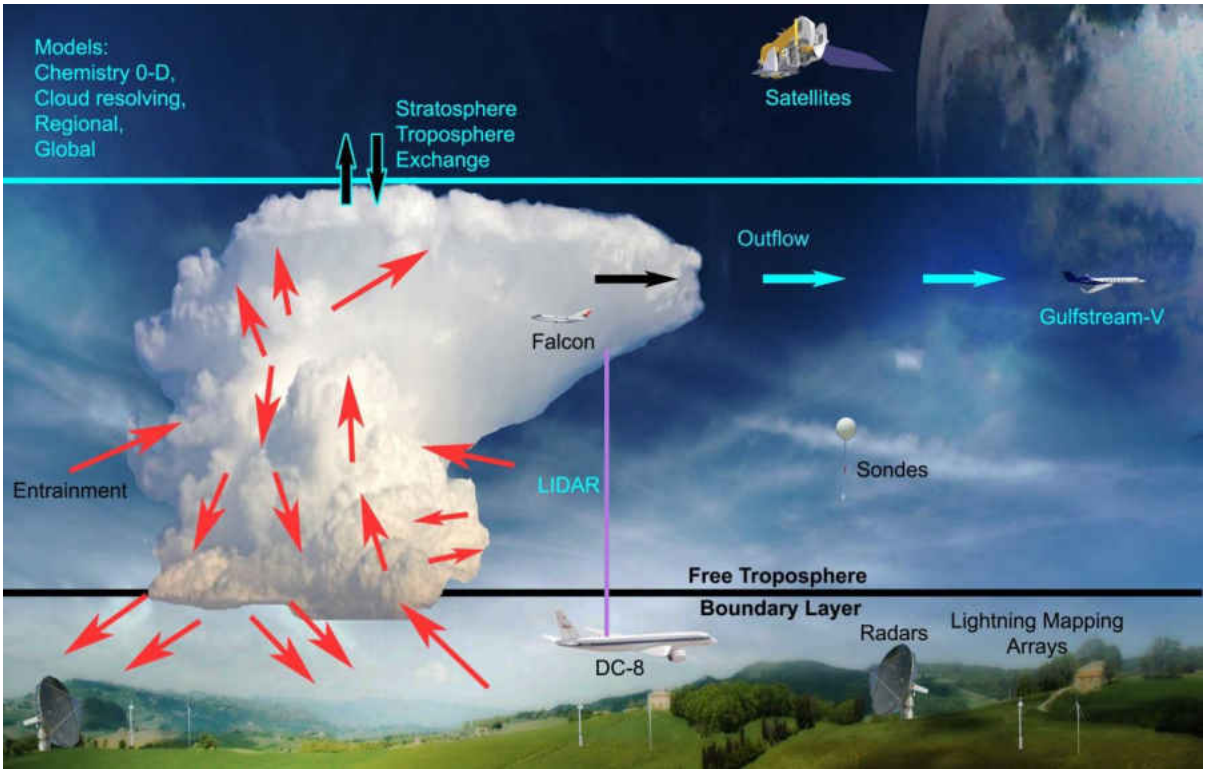

Figure 53: An overview of the various platforms used in the DC3 project and their relation to elements of a convective storm. Taken from www.eol.ucar.edu/projects/dc3/.

4.3.2 Alabama Case Result

On May 21, 2012, convection developed in central Tennessee and northern Alabama ahead of a cold front that produced a variety of convection typical to northern Alabama (UCAR 2012). The GV and DC-8 flew sampling the inflow region, convective anvil, and the near convection environment. The convection topped out at 35 kft to 38 kft (10.7 km to 11.6 km), with sounding reporting an LNB at 38 kft (11.6 km), which provides an upper limit the LMD should be below. Storms were present within the dual-Doppler lobes and sampled from the aircraft from 1930 UTC to 2130 UTC (UCAR 2012). As the day went on the storms strengthened; the final times sampled were the most mature.

Before running the CSA method to get an LMD height, some initial analysis was needed. Based on upon section 4.2, the final mature time, 2130 UTC, is the time that will have the

most representative LMD height for this case. Figure 54 shows the radar reflectivity cross section at 2 km at 2130 UTC. There are elements of a broken line, cluster of cells, and isolated cell morphologies present at 2130 UTC.

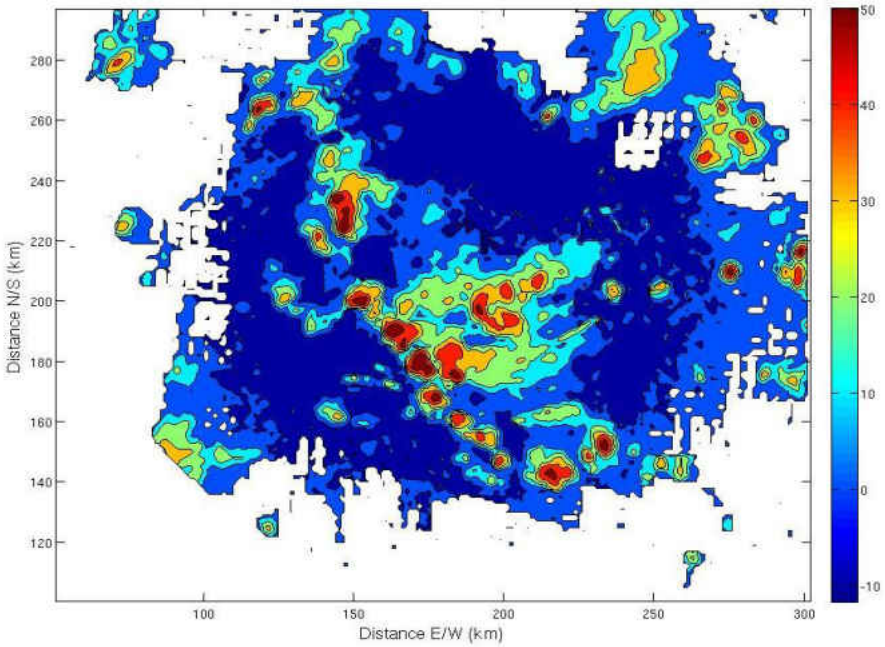

Figure 54: A horizontal radar reflectivity slice of the Alabama case on May 21, 2012 at 2130 UTC at 2 km.

Figure 55 shows the mass-derived detrainment using the entire domain. There are two maximums, i.e. LMDs, with the lower maximum at 3.5 km and the higher maximum at 8 km. The 3.5 km maximum is too low for an LMD and is due to the shallow convection present throughout the event. The 8 km maximum is high enough to be considered an LMD and is present due to anvil created for the deep convective updrafts. The multicellular nature of the storm in the analysis region is likely the cause of this dual signal. The more mature cells are detraining at the higher 8 km height while the younger cells are detraining at lower heights,

similar to the signal seen in section 4.2.3.

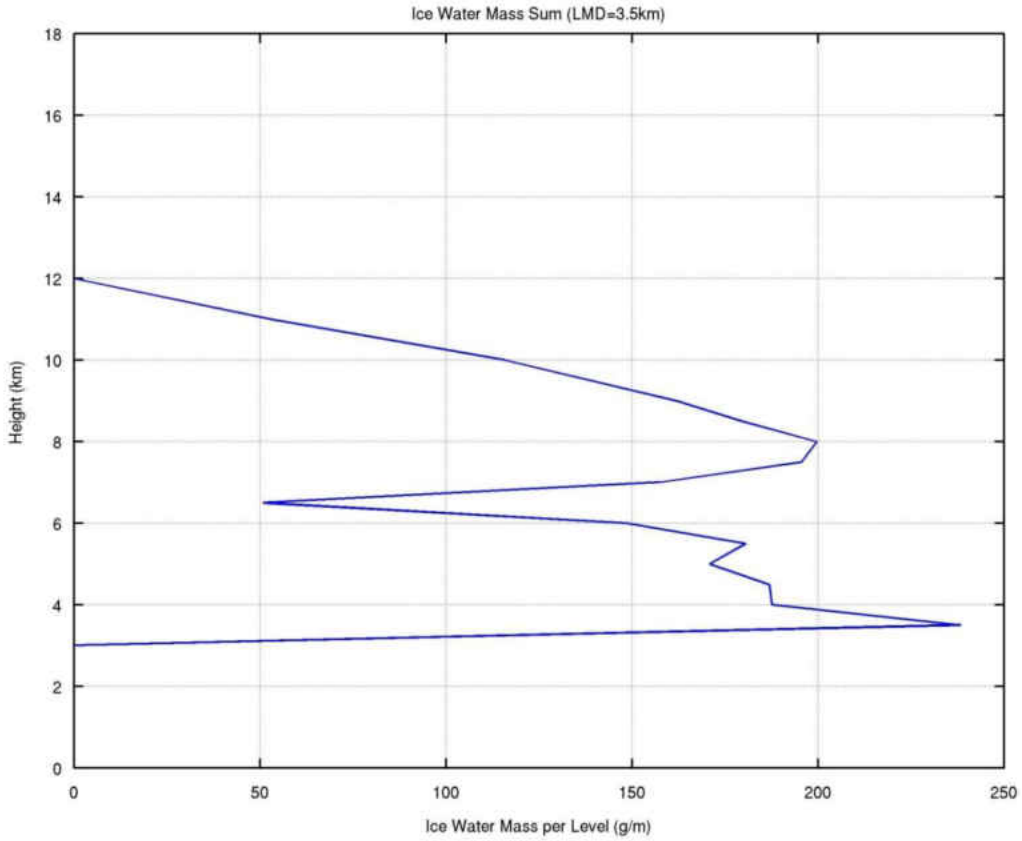

Figure 55: The horizontally integrated mass of the Alabama case on May 21, 2012 at 2130 UTC.

In addition to the mixed maturity of cells in the analysis domain, the morphology, i.e. clusters of cells, introduces error into the analysis. According to the DC3 Chief Scientist Summary the anvils for these storms were northeast of the updrafts, while some of the most intense cells in the broken line had additional cells to their northeast. The presence of updrafts in the area of most mature anvils makes anvil identification difficult. This difficulty in anvil identification leads to the lower LMD having the larger magnitude, since fewer anvil locations were available for the more mature storms (i.e. the higher LMD). Despite this being a difficult case due to the morphologies of the storms present, an LMD of 8 km, which is within one standard deviation (1.4 km) of the average vertical mass divergence based LMD

(9.6 km), was produced by the CSA method. These cases were from western Kansas and eastern Colorado so direct comparisons need to be made with caution. An analysis of the vertical cross sections at 2130 UTC show that most of the cells have anvils near 3 to 4 km while some of the cells had taller updrafts with anvils at 8 km.

4.3.3 Oklahoma Case Result

On May 29, isolated convection fired ahead of a dry line in southwestern Oklahoma before merging with convection to the north and forming an MCS (UCAR 2012). The inflow and outflow of the convection was well sampled for this case with all three aircraft deployed. Outflow sampled from the storms was from 34 kft to 37 kft (10.4 km to 11.3 km). This range was determined subjectively from the mission scientist as the primary areas of detrainment. This case was well sampled on all components (radar, aircraft, and LMA), and a downwind flight was also flown the next day (UCAR 2012). Figure 56 shows the radar reflectivity at 2 km at 2355 UTC on May 29. This only shows the region analyzed; there is more convection present in northern Oklahoma, but the mobile radars and aircraft deployed on the southern storms (UCAR 2012).

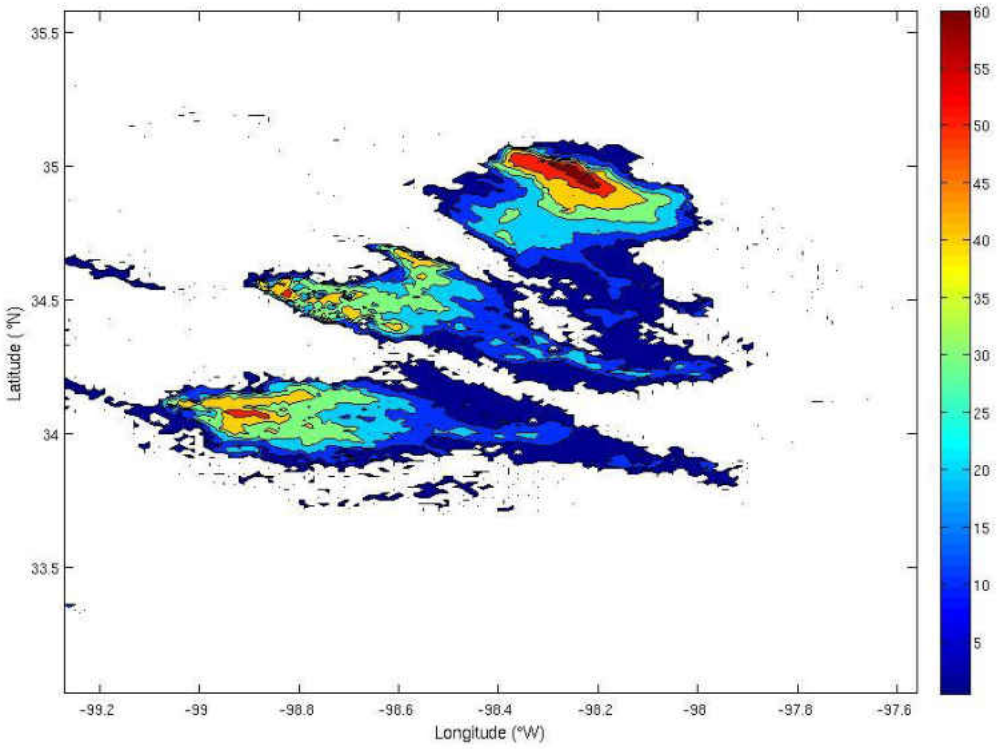

Figure 56: A horizontal radar reflectivity slice of the Oklahoma case on May 29 at 2355 UTC at 2 km.

The storms intensified rapidly, and, at 2355 UTC, the northern cell was near the peak of its maturity. Later, the southern cell becomes the dominant cell and is near the peak of its maturity at 0120 UTC on May 30. These two times were analyzed for mass-derived detrainment, focused on the cells in southern Oklahoma and northern Texas. The reflectivity at 2 km of the analysis area used at 2355 UTC is shown in figure 56. At 2355 UTC, the LMD of 10 km (figure 57) is very close to the range of the outflow values determined by the DC3 mission scientist. Note that the analysis at 2355 UTC is performed on all three cells (figure 56). As the day progressed the northern cell was absorbed by the MCS to the north and the

southern cell became dominant. At 0120 UTC, only the southern cell and remnants of the

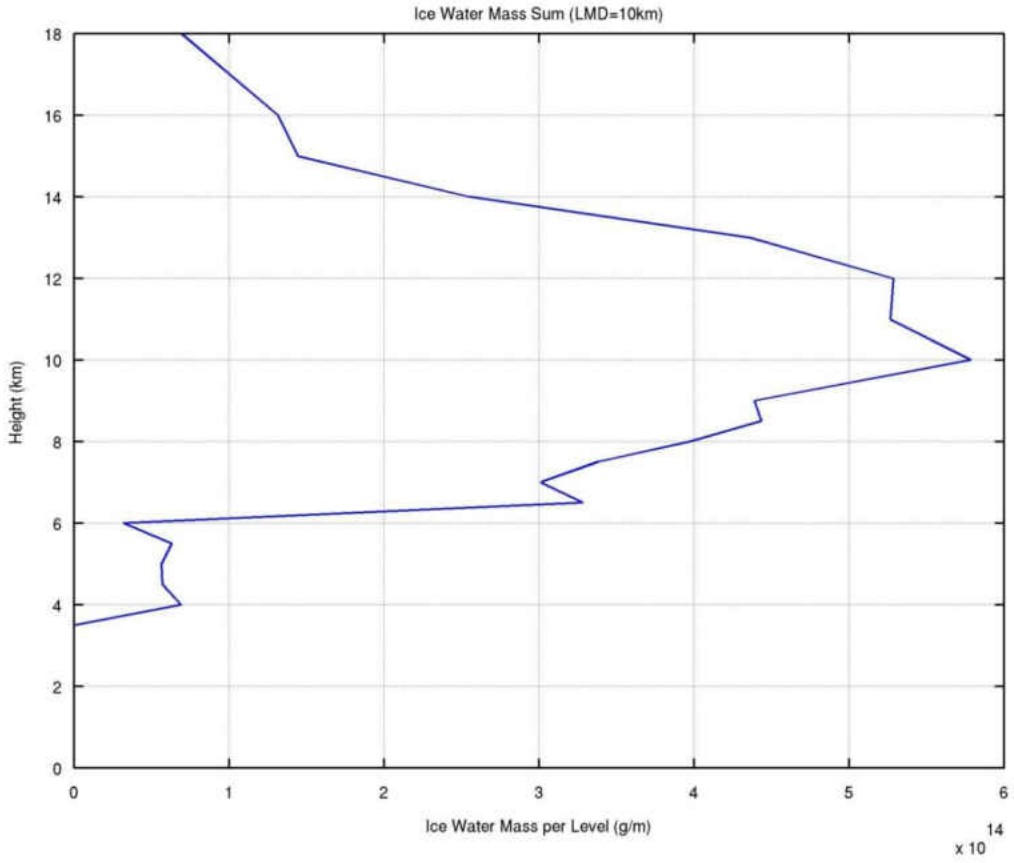

Figure 57: The horizontally integrated mass of the Oklahoma case on May 29, 2012 at 2355 UTC.

middle cell were analyzed; the mass-derived LMD is shown in figure 58. The double maximum in is caused by middle cell shown in figure 56 because it is still present in the analysis area. This cell was not removed because some anvil would have been lost taking out this cell. The higher LMD is at 12 km which is on the upper end of the outflow sampled by the aircraft. Both times, 2355 UTC and 0120 UTC, produced LMD close to the outflow levels determined by the mission scientist. The 2355 UTC result is with the standard deviation of the STEPS and CHILL cases vertical mass divergence based LMD average. The 0120 UTC time is not within one standard deviation of the average but higher LMDs are associated with stronger, more intense updrafts which could have been present, based on the

morphology of the storm.

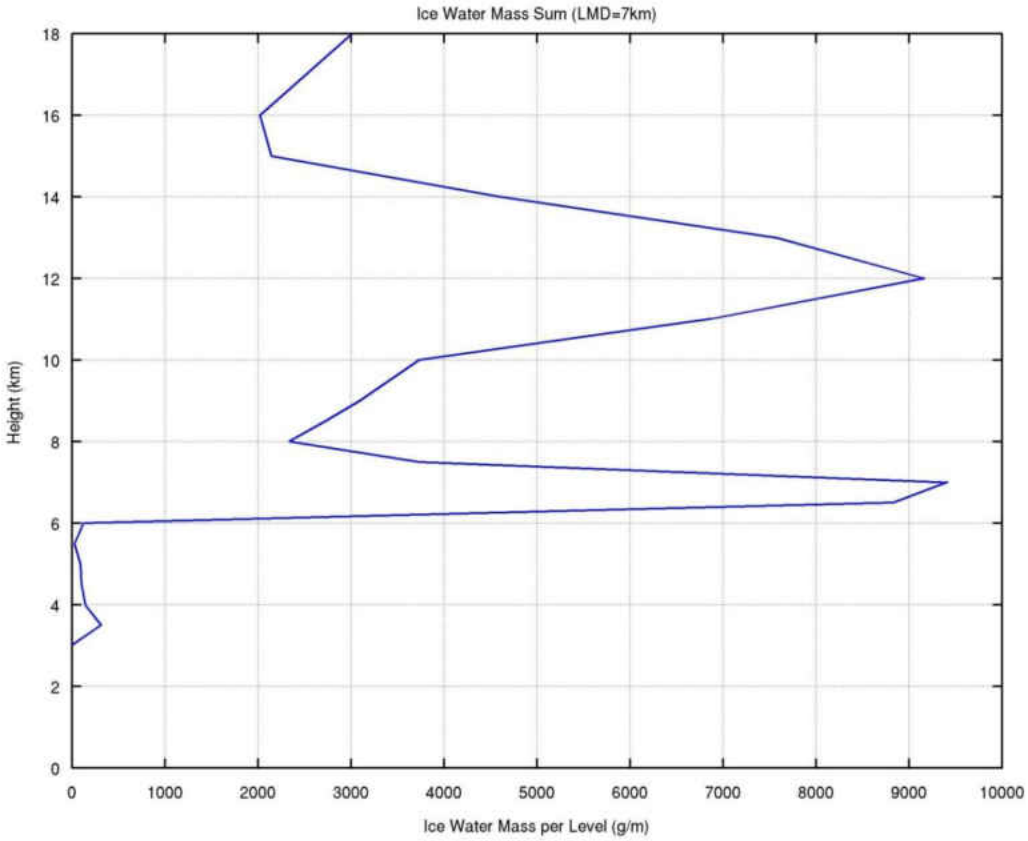

Figure 58: The horizontally integrated mass of the Oklahoma case on May 30, 2012 at 0120 UTC.

4.3.4 Colorado Case Result

On June 6, moist southeasterly flow and strong low level shear lead to the development of several isolated cells into northeastern Colorado (UCAR 2012). Late on June 6 and early on June 7 (UTC) data three hours of dual-Doppler data, LMA data, soundings, and flights were all recorded. This was a long convective event in the Colorado domain as convection was present in the domain from 20 UTC on June 6 until 9 UTC on June 7. A downwind flight which took off at 19 UTC on June 7 towards Missouri was also performed (UCAR 2012). There should be ample data to verify the LMD height results from the CSA method once the data is released. A time from late in the event at 0800 UTC on June 7 was analyzed for this

case, as at this time a well-developed isolated cell was present as shown in

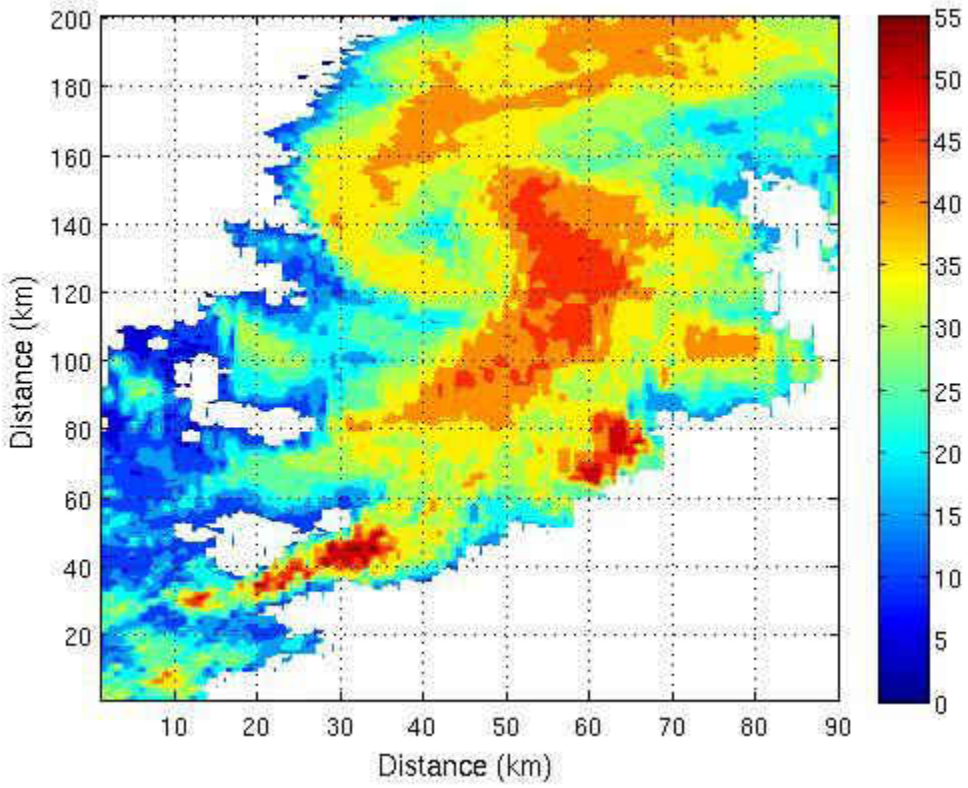

Figure 59: A horizontal radar reflectivity slice of the Colorado case on June 7 at 0800 UTC at 2 km.

figure 59. Figure 60 shows the mass profile based on the CSA method with an LMD at 8 km. Based upon the vertical cross section from 0800 UTC an 8 km LMD matches well with the anvil height as shown in figure 61. An 8 km LMD seems reasonable based on the other the CHILL and STEPS cases average vertical mass divergence based LMD of 9.6 km. Since the STEPS and CHILL cases were from the same region there is more confidence in this comparison.

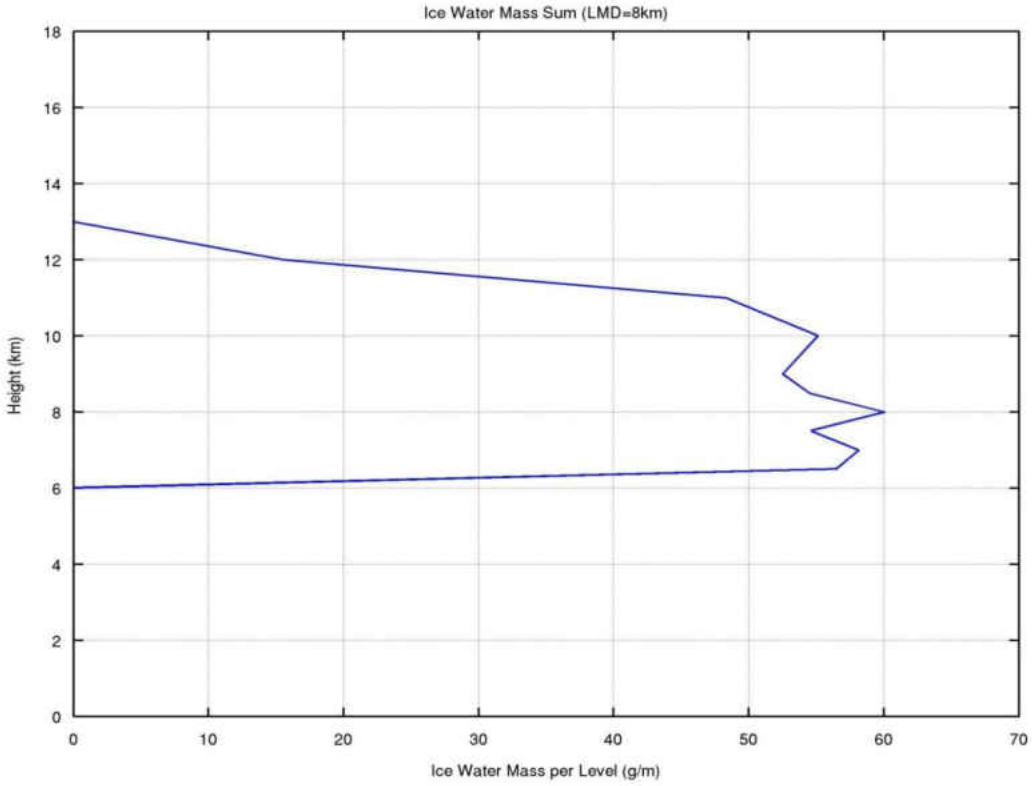

.

Figure 60: The horizontally integrated mass of the Colorado case on June 7, 2012 at 0800 UTC.

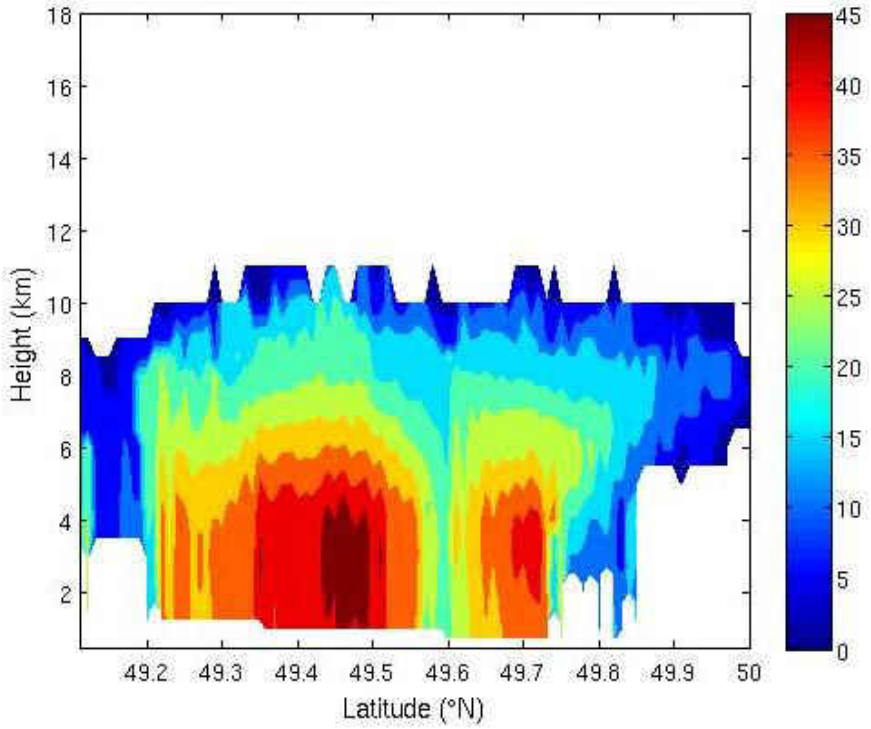

Figure 61: Figure 61: A vertical radar reflectivity slice of the Colorado case on June 7 at 0800 UTC.

CHAPTER 5

CONCLUSION

The objective of this study was to produce a methodology for estimating the level of maximum detrainment in convective systems using only radar reflectivity data. Using the results of Mullendore et al. (2009) as a foundation, three methodologies were tested with nine cases: Dual-Doppler convective cores with simple anvil (DDA), Steiner et al. (1995) convective cores with simple anvil (Steiner), and Feng et al. (2011) CSA convective core and anvil classifications (CSA). Differences in the performance of these methods resulted from differences in the convective and anvil classification approaches. It was found that the method with the most complex anvil identification classification scheme (CSA) was the best method of the three. The CSA method uses classifications based upon Feng et al. (2011), which used a multi-layer echo identification technique. The methods previously presented in the literature are most like the Steiner method, so this project shows that the CSA method is an improvement over currently used methods.

Although the CSA method was clearly superior to the two other methods that were tested, it did not perform well at all analysis times and for all cases. Hence, recommendations for application of the method were needed. The nine cases provided a variety of storm types and morphologies, which led to suggestions for the application of the method. The developed methodology works best for mature isolated convective cells. Pre-

processing of the radar data prior to application of the method removes most of the features that produce poor results, but because of this no values may be provided for some convective systems. The main factors that are not addressed via pre-processing are maturity and morphology. Any application of this methodology needs to have a means for diagnosing storm maturity so that times when the methodology can be accurately applied can be determined. A method will also be needed for removing cases that exhibit the clusters of cells morphology. These suggestions were applied by doing subjective analysis to pick times that would be representative of the case three times, one case for each region of DC3. All three cases produced believable results, but the results cannot be verified until the data from DC3 is released.

Future research will focus on trying to find ways to improve the methodology for the situations in which it currently struggles, like the clustered cells morphology. Also, a method for identifying storm maturity that does not require a subjective analysis is needed. Once these goals are accomplished, the methodology that is recommended herein can be used to analyze storms of varied types from many different regions to meet the final goal of this line of work--helping constrain chemical transport models based upon storm type and geographic location.

REFERENCES

Andreae, M. O., J. Fishman, and J. Lindesay, 1996: The Southern Tropical Atlantic Region Experiment (STARE): Transport and Atmospheric Chemistry near the Equator-Atlantic (TRACE A) and Southern African Fire-Atmosphere Research Initiative (SAFARI): An introduction. J. Geophys. Res., **101(D19)**, 23519–23520, doi:10.1029/96JD01786.

Barth, M., W. Brune, C. Cantrell, and S. Rutledge, 2012: Deep Convective Clouds and Chemistry (DC3) Operations Plan, 107. [online] Available from: http://www.eol.ucar.edu/projects/dc3/documents/DC3_Operations_Plan_28_Apr_2012.pdf

Bluestein, Howard B., Carlton R. Parks, 1983: A Synoptic and Photographic Climatology of Low-Precipitation Severe Thunderstorms in the Southern Plains. Mon. Wea. Rev., **111**, 2034–2046. doi: http://dx.doi.org/10.1175/1520-0493(1983)111<2034:ASAPCO>2.0.CO;2

Boe, Bruce A., and Coauthors, 1992: The North Dakota Thunderstorm Project: A Cooperative Study of High Plains Thunderstorms. Bull. Amer. Meteor. Soc., **73**, 145–160.

Chatfield, R. B., and A. C. Delany,1990: Convection links biomass burning to increased tropical ozone: However, models will tend to overpredict 03, J. Geophys. Res., **95**,473-18.

Cotton, W. R. and Coauthors, 1995: Cloud Venting - A Review and some New Global Annual Estimates. Earth-Sci Reviews, **39.3-4**, 169-206.

Dickerson, R. R. and Coauthors ,1987: Thunderstorms: An important mechanism in the transport of air pollutants, Science, **235**, 460 – 465.

Dong, X., B. Xi, and P. Minnis (2006), A climatology of midlatitude continental clouds from the ARM SGP Central Facility. Part II: Cloud fraction and surface radiative forcing, J. Clim., **19(9)**, 1765–1783. doi:10.1175/JCLI3710.1.

Erukhimova, T., and K. P. Bowman, 2006: Role of Convection in Global-Scale Transport in the Troposphere. J. Geophys. Res., **111**, D03105. doi: 10.1029/2005JD006006

Fischer, H. and Coauthors, 2003: Deep convective injection of boundary layer air into the lowermost stratosphere at midlatitudes. Atmos. Chem. Phys., **3**, 739–745, doi:10.5194/acp-3-739-2003.

Fishman, J., C. E. Watson, J. C. Larsen, and J. A. Logan, 1990: Distribution of tropospheric ozone determined from satellite data, J. Geophys. Res., **95**, 3599-3618.

Feng, Z., X. Dong, B. Xi, C. Schumacher, P. Minnis, and M. Khaiyer, 2011: Top-of-atmosphere radiation budget of convective core/stratiform rain and anvil clouds from deep convective systems. J. Geophys. Res., **116**, D23202. doi:10.1029/2011JD016451.

Frederick, Kaycee, Courtney Schumacher, 2008: Anvil Characteristics as Seen by C-POL during the Tropical Warm Pool International Cloud Experiment (TWP-ICE). Mon. Wea. Rev., **136**, 206–222. doi: http://dx.doi.org/10.1175/2007MWR2068.1

Gallus, William A., Nathan A. Snook, Elise V. Johnson, 2008: Spring and Summer Severe Weather Reports over the Midwest as a Function of Convective Mode: A Preliminary Study. *Wea. Forecasting*, **23**, 101–113.

Hauf, T., P. Schulte, R. Alheit, and H. Schlager, 1995: Rapid vertical transport by an isolated midlatitude thunderstorm. J. Geophys. Res., **100**, D11. doi:10.1029/95JD02324.

Holton, J. R., 2004: *An Introduction to Dynamic Meteorology*. 4t ed. Elsevier Academic Press, 535 pp.

Lang, Timothy J., Steven A. Rutledge, 2002: Relationships between Convective Storm Kinematics, Precipitation, and Lightning. Mon. Wea. Rev., **130**, 2492–2506.: http://dx.doi.org/10.1175/1520-0493(2002)130<2492:RBCSKP>2.0.CO;2

Leary, Colleen A., Robert A. Houze, 1979: Melting and Evaporation of Hydrometeors in Precipitation from the Anvil Clouds of Deep Tropical Convection. J. Atmos. Sci., **36**, 669–679. doi: http://dx.doi.org/10.1175/1520-0469(1979)036<0669:MAEOHI>2.0.CO;2

Lelieveld, J., and P. J. Crutzen, 1994: Role of Deep Cloud Convection in the Ozone Budget of the Troposphere. Science, **264**, 1759-61.

Lopez, J. P., Luo, M., Christensen, L. E., Loewenstein, M., Jost, H., Webster, C. R., & Osterman, G., 2008: TES carbon monoxide validation during two AVE campaigns using the Argus and ALIAS instruments on NASA's WB-57F. J. Geophys. Res.**113,** D16.

May, Peter T., Deepak K. Rajopadhyaya, 1999: Vertical Velocity Characteristics of Deep Convection over Darwin, Australia. Mon. Wea. Rev., **127**, 1056–1071. doi: http://dx.doi.org/10.1175/1520-0493(1999)127<1056:VVCODC>2.0.CO;2

Miller, L.J., C.G. Mohr, and A.J. Weinheimer, 1986: The simple rectification to Cartesian space of folded radial velocities from Doppler radar sampling. J. Atmos. Oceanic Technol., **3**, 162174.

Mohr, C. G., R. L. Vaughan, 1979: An Economical Procedure for Cartesian Interpolation and Display of Reflectivity Factor Data in Three-Dimensional Space. J. Appl. Meteor., **18**, 661–670. doi: http://dx.doi.org/10.1175/1520-0450(1979)018<0661:AEPFCI>2.0.CO;2

Mullendore, G. L., D. R. Durran, and J. R. Holton (2005), Cross-tropopause tracer transport in midlatitude convection, J. Geophys. Res., **110**, D06113. doi:*10.1029/2004JD005059.*

Mullendore, G. L., A. J. Homann, K. Bevers, and C. Schumacher, 2009: Radar reflectivity as a proxy for convective mass transport. J. Geophys. Res., **114**, D16103. doi:10.1029/2008JD011431.

Mullendore, G. L., A. J. Homann, S.T. Jorgenson, T.J. Lang, and S. A. Tessendorf, 2013: Relationship between level of neutral buoyancy and dual_Doppler observed mass detrainment levels in deep convection. Atmos. Chem. Phys.**13**, 181-190. doi:10.5194/acp-13-181-2013.

Pickering, K. E., A.M. Thompson, J. R. Scala, W.-K. Tao, and J.Simpson, 1992: Ozone production potential following convective redistribution of biomass burning emissions, J. Atmos. Chem., **14**, 297-313.

Pickering, K. E., et al., 1996:Convective transport of biomass burning emissions over Brazil during TRACE A, J. Geophys. Res., **101(D19)**, 23993–24012, doi:10.1029/96JD00346.

Ray, Peter S., Conrad L. Ziegler, William Bumgarner, Robert J. Serafin, 1980: Single- and Multiple-Doppler Radar Observations of Tornadic Storms. Mon. Wea. Rev., **108**, 1607–1625. doi: http://dx.doi.org/10.1175/1520-0493(1980)108<1607:SAMDRO>2.0.CO;2

Rind, D., and J. Lerner, 1996: Use of on-line tracers as a diagnostic tool in general circulation model development: 1. Horizontal and vertical transport in the troposphere. J. Geophys. Res., **101**, 12667-12683, doi:10.1029/96JD00551.

Steiner, M., R. A. Houze, and S. E. Yuter, 1995: Climatological characterization of three-dimensional storm structure from operational radar and rain gauge data. J. Appl. Meteorol., **34**, 1978–2007.

Takahashi, H., and Z. Luo, 2012: Where is the level of neutral buoyancy for deep convection?. Geophys. Res. Lett., **39**, doi:10.1029/2012GL052638.

Tessendorf, S.A., L.J. Miller, K.C. Wiens, and S.A. Rutledge, 2005: The 29 June 2000 supercell observed during STEPS. Part I: Kinematics and microphysics. *J. Atmos. Sci*., **62**, 4127-4150.

Tessendorf, S.A., K.C. Wiens, and S.A. Rutledge, 2007: Radar and lightning observations of an electrically inverted storm observed during STEPS. *Mon. Wea. Rev*., **135**, 3665-3681.

Tessendorf, S.A., S.A. Rutledge, and K.C. Wiens, 2007: Radar and lightning observations of normal and inverted polarity multicellular storms from STEPS. *Mon. Wea. Rev*., **135**, 3682-3706.

UCAR, cited 2013: EOL/DC3_2012 FIELD CATALOG. [Available online at: http://catalog.eol.ucar.edu/dc3/.]

Weisman, M. L., and L. J. Miller, 2000: An overview of the severe thunderstorm electrification and precipitation study (STEPS). Preprints, 20th Conf. on Severe Local Storms,Orlando, FL, Amer. Meteor. Soc., 273–276.

Zhang, J. and coauthors, 2011: National Mosaic and Multi-Sensor QPE (NMQ) system: Description, results, and future plans, Bull. Am. Meteorol. Soc., **92(10)**, 1321–1338, doi:10.1175/2011BAMS-D-11-0047.1.